UNIVERSIDAD COMPLUTENSE DE MADRID

FACULTAD DE CIENCIAS FÍSICAS

Departamento de Astrofísica y Ciencias de la Atmósfera

MASS AND STAR FORMATION RATE EVOLUTION OF INFRARED SELECTED GALAXIES IN THE COSMOS FIELD

MEMORIA PARA OPTAR AL GRADO DE DOCTOR
PRESENTADA POR

Helena Domínguez Sánchez

Bajo la dirección de los doctores
Carlotta Gruppioni
Andrea Cimatti
Francesca Pozzi

Madrid, 2012

UNIVERSIDAD COMPLUTENSE DE MADRID

FACULTAD DE CIENCIAS FÍSICAS
DEPARTAMENTO DE ASTROFÍSICA Y CIENCIAS DE LA ATMÓSFERA

Mass and Star Formation Rate Evolution of Infrared selected Galaxies in the COSMOS Field

Evolución de la Masa y de la Tasa de Formación Estelar de Galaxias Seleccionadas en el Infrarrojo en el Campo COSMOS

Tesis de Doctorado
de
HELENA DOMÍNGUEZ SÁNCHEZ

DIRECTORES:
Dra. **Carlotta GRUPPIONI (*INAF-OABO*)**
Dr. **Andrea CIMATTI (*UniBo*)**
Dra. **Francesca POZZI (*UniBo*)**

Memoria presentada por Helena Domínguez Sánchez para aspirar al grado de Doctora en Ciencias Físicas
Madrid, 2012

A Sara e Francesca P., per aprirmi la strada.
A Via Orfeo 25, per i pranzi della domenica.
Ad Annamaria, per rendere possibile questa dedica.

A mis abuelas (y a todos los que vienen detrás).

‘*La astrofísica es una ciencia que debe ser estudiada del siguiente modo. Beber un poco de vodka, una noche clara y fría, envolverse los pies en una manta de pelo, sentarse en el balcón y mirar al cielo. La ubicación preferible es una zona montañosa, con un débil retumbar de aludes en la lejanía; el momento preferible, las horas de la melancolía. Si no se sigue esta receta, la ciencia en cuestión parecerá un bosque petrificado de números y ecuaciones; pero aquel que se atiene a lo prescrito experimentará un estado curioso de éxtasis. Los signos algebraicos se transformarán en claves de violín, X e Y vibrarán y resonarán como sopranos y bajos, y de las extrañas ecuaciones surgirán la sinfonía del progreso y la decadencia del universo...*’

Arthur Koestler, El Camino hacia Marx

Contents

Resumen de la Tesis de Doctorado

ESTA Tesis de Doctorado ha sido realizada y escrita gracias a una Beca Internacional del Instituto de Astrofísica de Canarias (IAC) en el Observatorio Astronómico de Bolonia (INAF-OABO), Italia. Tanto los directores de la Tesis como el resto de los colaboradores son de habla no hispana, con lo que habría sido incoherente escribir la Tesis en castellano. A continuación presentamos un resumen con los principales contenidos y resultados de esta Tesis en castellano.

En esta Tesis se pretende estudiar la evolución de la masa y de la tasa de formación estelar de galaxias seleccionadas en el infrarrojo utilizando datos multi-banda del campo COSMOS. En la primera parte de la tesis hemos analizado una muestra de $\sim$ 80000 galaxias en el campo COSMOS seleccionadas en la banda 3.6 μm de IRAC con $\mathrm{mag}_{3.6} < 22.0$ y hemos calculado sus desplazamientos al rojo a partir de la información fotométrica. Una vez calculados sus desplazamientos al rojo, hemos estudiado en mayor detalle una sub-muestra de ~20000 galaxias con alto desplazamiento al rojo ($1.4 < z < 3.0$), calculando importantes parámetros físicos como la masa, la tasa de formación estelar o la edad, a partir de sus distribuciones espectrales de energía. Hemos dividido nuestras galaxies en 3 tipos dependiendo de su tasa de formación específ ca (*e.d.*, la cantidad de masa transformada en estrellas por unidad de tiempo y masa de la galaxia): galaxias pasivas, galaxias con formación estelar activa y galaxias de tipo intermedio. Hemos calculado la Función de Masa Estelar para la población total y para los 3 tipos de galaxias en 4 bins de desplazamiento al rojo con el propósito de estudiar la evolución de galaxias de distinta masa y modos de formación estelar con el tiempo.

Por otra parte, ya que la tasa de formación estelar es un parámetro fundamental para estudiar la formación y evolución de las galaxias, en la segunda parte de la Tesis, hemos aprovechado la posibilidad que nos brindan los nuevos datos del Telescopio

Espacial de la Agencia Espacial Europea Herschel para probar la validez de la receta para calcular la tasa de formación estelar a partir de la luminosidad infrarroja. Para este propósito hemos utilzado una muestra de 474 galaxias seleccionadas en el infrarrojo lejano (100 y 160 μm) con $0 < z < 0.46$, que tienen también asociada información espectroscópica del estudio 20k en el campo COSMOS. Hemos calculado la tasa de formación estelar a partir de la luminosidad infrarroja simplemente multiplicando esta luminosidad por una constante derivada a partir de modelos teóricos por Kennicutt (1998b). Para probar la validez de esta fórmula hemos comparado el resultado con la tasa de formación estelar obtenida a partir de la luminosidad de la línea de emisión Hα. Hemos comparado los dos resultados y hemos estudiado en mayor profundidad la dependencia de los resultados con distintas propiedades de las galaxias como el desplazamiento al rojo, la masa, la metalicidad, la tasa de formación estelar específ ca o el tipo morfológico.

Estudio de la Función Estelar de Masa de Galaxias con Alto Desplazamiento al Rojo

Para analizar la Función Estelar de Masa de galaxias con alto desplazamiento al rojo hemos construido un catálogo multi-banda desde la banda u^* hasta 24 μm a partir del método de 'Likelihood Ratio' (Sutherland & Saunders, 1992). Hemos partido de una muestra de ~80000 galaxias detectadas en la banda 3.6 μm de IRAC y hemos asociado un catálogo óptico multi-banda (Capak et al., 2007) que incluye fotometría en 9 bandas (u^*, B_J, g^+, V_J, r^+, i^+, z^+, J, K_s), así como el catálogo MIPS 24 μm (Le Floc'h et al., 2009). Para las fuentes para las que no se ha encontrado una asociación con el catálogo óptico hemos realizado la asociación con un catálogo seleccionado en el infrarrojo cercano, en la banda K_s (McCracken et al., 2010) que contiene información adicional en las bandas B_J, i^+, z^+ y J.

El hecho de utilizar una muestra seleccionada en el infrarrojo es muy importante para tener una muestra completa en masa, ya que la emisión en el infrarrojo cercano traza la emisión de las estrellas que contribuyen en mayor parte a la masa estelar de las galaxias. Además, los datos en el infrarrojo son muy importantes para estudiar objetos débiles en las longitudes de onda ópticas, pero que pueden suponer una importante contribución a la densidad de masa estelar a alto desplazamiento al rojo. Por otra parte, el hecho de estudiar datos del campo COSMOS, con una gran área

(2 deg^2), nos ayuda a evitar errores asociados a la variación cósmica. Además, al ser uno de los campos del cielo más profundamente estudiado, es posible recuperar información de estudios precedentes en casi todas las longitudes de onda.

Una vez construido el catálogo multi-banda en el campo COSMOS hemos calculado los desplazamientos al rojo de nuestras galaxias mediante un ajuste por mínimos cuadrados de librerias teóricas a la distribución espectral de enregía de cada galaxia (*SED-fitting*). Este método, ampliamente utilizado en la literatura, permite conocer el desplazamiento al rojo de un gran número de galaxias sin necesidad de tener información espectroscópica. Comparando los desplazamientos al rojo obtenidos mediante la fotometría con los desplazamientos al rojo espectrales conocidos para una sub-muestra de nuestras galaxias hemos comprobado que los resultados de los desplazamientos al rojo fotométricos son certeros, con $\sigma_{\Delta z/(1+z_s)} = 0.06$ y un porcentaje de errores catastróf cos del $\eta = 3.3\%$.

Como estamos interesados en estudiar la evolución de galaxias lejanas, hemos procedido a analizar con mayor detalle sólo las galaxias con un desplazamiento al rojo (z) $1.4 < z < 3.0$. Para esta sub-muestra, de nuevo utilizando las distribuciones espectrales de energía y haciendo uso de modelos de síntesis estelares de Maraston (2005), hemos derivado las características fundamentales que nos permitirán estudiar la evolución de estas galaxias (masa, edad, metalicidad, tasa de formación estelar...). Para clasif car las galaxias en distintos tipos nos hemos basado en los valores de la tasa de formación específ ca, *e.d.*, la tasa de formación estelar dividida entre la masa de cada galaxia ($SSFR = SFR/M$):

1. Galaxias con formación activa: aquellas con $log(SSFR[\mathrm{Gyr}^{-1}]) > -0.5$
2. Galaxias de tipo intemedio: aquellas con $-2 < log(SSFR[\mathrm{Gyr}^{-1}]) < -0.5$.
3. Galaxias pasivas: aquellas con $log(SSFR[\mathrm{Gyr}^{-1}]) < -2$.

Con todos los ingredientes necesarios calculados anteriormente, hemos calculado la Función de Masa Estelar (FME) para todas las galaxias y las galaxias divididas en distintos tipos en 3 bins de z: 1.4-1.6,1.6-2.0, 2.0-2.5 and 2.5-3.0. Nuestra FME para la población total coincide, en general, con otras FME calculadas anteriormente por otros autores. La FME de las galaxias pasivas muestra una considerable evolución desde $2.5 < z < 3.0$ hasta $1.4 < z < 1.6$. Para las galaxias masivas ($logM \sim 11.0$) el número de galaxias pasivas aumenta $\sim$ 1 dex en este intervalo de tiempo. La evolución es practicamente constante en todos los bins de z ($\sim$ 0.3 dex), *e.d.*, el

número de galaxias pasivas aumenta continuamente con el tiempo cósmico. Otro de los resultados interesantes que hemos encontrado es el hecho de que $z \sim 1.5$ parece ser una época de transición. Mientras a $z \gtrsim 1.5$ las FME está dominada por galaxias con formación estelar activa para todas las masas, las galaxias de tipo intermedio e incluso las pasivas empiezan a ser más abuntantes a $z \lesssim 1.5$. Además, esta evolución depende signif cativamente de la masa, ya que las galaxias con masas mayores dejan de formar estrellas antes que las galaxias de masas menores. De hecho, la mayor parte de las galaxias de baja masa ($M \lesssim 10^{10.5} M_{\odot}$) sigue formando estrellas activamente incluso a $1.4 < z < 1.6$.

También hemos calculado la densidad de masa estelar de los distintos tipos de galaxias. Por una parte la de las galaxias pasivas y por otra la de las galaxias de tipos intermedios o con gran actividad de formación estelar. La densidad estelar en el periodo de tiempo estudiado ($t \sim 2 - 4.5$ Gyr) aumenta muy rápidamente para las dos poblaciones (~ 0.5 dex para las galaxias con formación estelar y ~ 0.9 dex para las galaxias pasivas). Este aumento se ve frenado a z menores, pero, mientras que la densidad de masa estelar de galaxias con formación estelar se mantiene prácticamente constante desde $z \sim 1.2$ ($t \sim 5.0$ Gyr), la densidad estelar de galaxias pasivas continúa aumentando hasta $z \sim 1.0$ ($t \sim 6.0$ Gyr), alcanzando valores comparables a los de la densidad de las galaxias con formación estelar a $z < 1.0$.

Por último, hemos comparado nuestros resultados con las predicciones de los modelos teóricos. Aunque todos los modelos predicen un aumento del número de galaxias pasivas con el tiempo cósmico, sólo uno, el modelo basado en la simulación Millennium, reproduce los datos observados. Este modelo tiene en consideración el *feedback* de las galaxias centrales en cúmulos de galaxias, que parece ser fundamental para obtener resultados de acuerdo con las observaciones.

Comparación de Indicadores de la Tasa de Formación Estelar

En este caso hemos estudiado una muestra de 474 galaxias con $0 < z < 0.46$ seleccionadas en el infrarrojo lejano (100 y 160μm) que además tienen información espectroscópica del estudio 20k de zCOSMOS asociada, así como información fotométrica en las bandas ópticas y infrarrojas cercanas. Hemos eliminado las galaxias con nucleos galacticos activos para evitar contaminación de emisión

infrarroja no asociada a la formación estelar.

Para este estudio hemos utilizado datos del estudio PEP (PACS Evolutionary Probe) del Telescopio Espacial de la Agencia Espacial Europea Herschel. Herschel es un telescopio espacial infrarrojo que permite observar las galaxias en longitudes de onda jamás observadas hasta el momento con tanta precisión. Los datos de PACS a 100 y 160 μm son fundamentales para muestrear el pico en el infrarrojo lejano de las galaxias cercanas y calcular así la luminosidad infrarroja (8-1000 μm) con la mayor precisión conseguida hasta el momento.

Uno de los indicadores más usados en la literatura para calcular la tasa de formación estelar es precisamente la luminosidad infrarroja. Generalmente se utiliza la conversión propuesta por Kennicutt (1998b) [K98], que simplemente multiplica esta luminosidad infrarroja por una constante. Este factor de conversión ha sido calculado a partir de modelos teóricos para unas condiciones particulares (formación estelar continua, metalicidad solar, función inicial de masa de Salpeter) y debería ser válido solamente para brotes de formación estelar menores de 10^8 yr. Sin embargo, esta fórmula se utiliza comunmente en la literatura para calcular la tasa de formación estelar de todo tipo de galaxias con distintas propiedades. En este trabajo hemos comprobado si la tasa de formación estelar calculada de esta manera es válida para galaxias con distintos tipos morfológicos y distintas propiedades. El uso de los datos de PEP nos permite hacer esto sin la incerteza asociada a la extrapolación del pico infrarrojo. Una vez calculada la luminosidad infrarroja a partir del *SED-fitting* de los datos de nuestras galaxias en las bandas IRAC, MIPS y PEP, calculamos la tasa de formación estelar multiplicando este valor por la constante calculada en K98 (la denotaremos como SFR(L_{IR})).

Desgraciadamente, ningún indicador de tasa de formación estelar es exacto, con lo que no tenemos un valor de referencia con el que comparar los resultados obtenidos a partir de la luminosidad infrarroja. Sin embargo, uno de los indicadores más directo de la tasa de formación estelar es la luminosidad Hα, con lo que hemos calculado nuestra tasa de formación estelar a partir de estos valores para nuestras galaxias. La luminosidad Hα se ve afectada por la extinción del polvo y gas que rodea a las estrellas recién formadas, con lo que es necesario aplicar una corrección de extinción. Lamentablemente, la calidad de los espectros de nuestra muestra no es lo suf cientemente alta como para proporcionarnos una medida f able de la línea Hβ (necesario para calcular la extinción a partir de la relación Hβ/Hα observada y la teórica). Por lo tanto, hemos construido 3 espectros medios

dividiendo nuestras galaxias en 3 bins de luminosidad infrarroja. Los espectros medios tienen una mayor S/N con lo que podemos medir la línea de emisión Hβ. Hemos calculado la extinción media en cada bin de luminosidad infrarroja y hemos aplicado la extinción correspondiente al bin de L_{IR} al que pertenece cada galaxia a la luminosidad Hα de cada galaxia. La tasa de formación estelar a partir de la luminosidad Hα ha sido calculada mediante una simple relación de conversión (*e.d.*, multiplicando la luminosidad por una constante, como con la luminosidad infrarroja), así como haciendo uso de métodos algo más complicados obtenidos por Brinchmann et al. (2004) [B04]. En B04 se utiliza un factor de conversión no constante, sino dependiente de la masa de las galaxias. También para los valores de extinción en Hα se propenen valores distintos para galaxias de distintas masas. Denotamos la tasa de formación estelar derivada a partir de la luminosidad Hα como SFR(Hα).

Por tanto, una vez calculada la tasa de formación estelar de diversos modos, hemos comparado los resultados, encontrando que están bastante de acuerdo, teniedo en cuenta el amplio rango de tasas de formación estelar consideradas (3 órdenes de magnitud). También hemos estudiado cuáles son las propiedades de las galaxias que más afectan la comparación entre indicadores. El desplazamiento al rojo no parece afectar sustancialmente el cáculo de la tasa de formación estelar (al menos hasta z=0.46). El efecto de la masa no es muy signif cativo y se ve reducido cuando usamos las recetas de B04 que tienen en cuenta la masa de las galaxias. Sin embargo, las galaxias con distintas metalicidades si parecen tener distintos comportamientos. Si comparamos los valores log [SFR(L_{IR})/SFR(Hα)] para galaxias con altas y bajas metalicidades encontramos una diferencia de hasta 0.6 dex. Este efecto no se reduce ni siquiera cuando utilizamos los métodos derivados por B04. La tasa de formación estelar específ ca parece afectar a la comparación de indicadores de tasa de formación para bajos valores de tasa de formación estelar específ cos, ya que la SFR(L_{IR}) está sobrestimada debido a la contribución a la L_{IR} de la población estelar de mayor edad. Por último hemos estudiado la validez de los indicadores de tasa de formación estelar para galaxias con distintos tipos morfológicos (Sa, Sb, Sc, Sd/Irr). Para el grueso de las galaxias espirales ambos indicadores parecen estar de acuerdo, con valores de la pendiente SFR(L_{IR}) vs SFR(Hα) muy cercanos a 1. Para las galaxias de últimos tipos (Sd/Irr), la pendiente es mucho mayor ($m = 2.45 \pm 0.99$), aunque sigue siendo consistente a 3σ con la relación uno a uno debido al reducido número de galaxias clasif cadas

como tal (sólo 17). Sin embargo, podemos confirmar que observamos un continuo aumento de la pendiente de la relación SFR(L_{IR}) vs SFR(Hα) desde las espirales de primeros tipos hasta las espirales de últimos tipos, que sería interesante estudiar con una muestra más grande de galaxies irregulares.

Motivation and Aims of the Thesis Project

AMONG the variety of open issues in galaxy formation and evolution, the question of mass assembly and star formation are certainly crucial. The global aim of this thesis project is to study two complementary aspects of galaxy formation: the stellar mass evolution and the star formation rate and its accuracy. Two main studies allowed us to better understand these two issues. First, we present a detailed analysis of the stellar mass function evolution of a sample of high redshift galaxies with different star formation rates. Second, we show the comparison of two star formation rate indicators and their dependence on the galaxies properties.

The Evolution of the Galaxy Stellar Mass Function of Different Galaxy Populations

In this thesis we aim to present a complete study on the evolution of different galaxy populations at high redshifts ($1.4 \leq z \leq 3.0$). It is well known that galaxies can be roughly classif ed into star-forming and quiescent (or passive) galaxies depending on their star-formation activity. This bimodality, which affects the observed properties of galaxies (colors, morphologies, spectral features), is conf rmed to exist at least up to $z \sim 1$ and possibly up to $z \sim 2$. Both populations evolve in very different ways, so comparing the observations of their properties at different redshifts with those predicted by theoretical models is a crucial tool of present day astronomy to better understand how galaxies in the Universe formed and evolved. In particular, the quiescent population, composed by early type galaxies

(ETGs), often related to elliptical morphologies, is a key piece of the evolution and formation of galaxies, as these systems contain most of the mass of the present day universe. Besides, their formation is a rather controversial subject, so their observed properties can help to disentangle between the theoretical predictions of various cosmological models.

While the results up to $z \sim 1$ are quite solid thanks to the large samples of galaxies and to the spectroscopic information available, the samples of galaxies divided into different types at $z > 1 - 2$ are still small. Moreover, ETGs are the more clustered galaxies in the universe, making their study very complicated due to f eld to f eld variations, which introduce large uncertainties in their statistical properties, due to the cosmic variance.

Therefore, the uncertainties involved in the study of the evolution of quiescent galaxies at high redshifts are still large due to the observational diff culty to identify large samples of ETGs at high z (> 1.5). In particular, long wavelength data are necessary to cover the optical-near infrared part of the spectrum of high redshift galaxies, a crucial spectral range fundamental for estimating the photometric redshifts and for calculating the galaxy stellar masses. In addition, the collection of a large sample of high redshift galaxies requires a combination of large areas and deep near-IR (NIR) observations. Due to these diff culties, the study of the Galaxy Stellar Mass Function (GSMF hereafter) divided by galaxy types at $z > 1.5$ so far has been only roughly explored and our knowledge of the evolution of galaxies at high z is still rather poor.

Motivated by the limited information available at $z \geq 1.5$, we have studied the evolution of the GSMF with cosmic time for ~18000 high-z (specif cally at $z \geq 1.4$) galaxies for the total galaxy population and for the sample divided on the basis of the galaxy star-formation activity. We considered the COSMOS survey, which is the perfect wide area sample to look for rare and clustered objects, such as the old and massive ETGs, with much improved statistics. This survey (Scoville, 2007) presents many advantages when compared with other surveys. First of all, the continuous coverage of ~2 deg^2 substantially reduces the effect of cosmic variance. Besides, its extensive multi-λ coverage allows to calculate accurate photometric redshifts (Ilbert et al., 2009) and to study the sources based on their spectral energy distributions (SEDs), which is a more physical and complete approach than using only colors or morphological information. Secondly, the multiwavelength data include deep Spitzer/IRAC ($3.6 - 8.0$ μm; Sanders et al. 2007) and K_s-band data (McCracken

et al., 2010), crucial for estimating stellar masses at $z \sim 2$.

Galaxies of the present work are selected in the IRAC1 channel (3.6 μm), allowing to sample the optical-NIR stellar bump at $z > 1$. In addition, data at red wavelength are crucial to detect galaxies that are very faint in the optical (or even undetected) but may contribute signif cantly to, or even dominate, the stellar mass density at high redshift (Yan et al. 2000, Franx et al. 2003, Rodighiero et al. 2007). The extensive multi-band data are used to separate galaxies into different populations based on their SEDs. The present work extends to higher redshifts the study of Ilbert et al. (2010). The sample of Ilbert et al. (2010) was selected at 3.6 μm as the present one, but their restriction to IRAC sources with an i^+-band counterpart ($i^+ < 25.5$) limited their study to $z \lesssim 2$ and to larger stellar masses. In our work we considered and carefully analyzed also sources undetected in the optical bands.

Comparison of Star Formation Rate Indicators

By def nition, the main difference between the star-forming and the quiescent galaxies is the amount of star formation taking place on the galaxies at the present time. As galaxies have wide ranges of masses, the classif cation is often based on the specif c star formation rate ($SSFR$), which is the ratio between the star formation rate and the galaxy mass ($SSFR = SFR/M$). This is the approach commonly used in literature and which we used in this thesis. It is, therefore, of a great importance, to have a good SFR estimate. Many recipes have been derived to estimate SFR from emission at different wavelengths, as well as through SED-f tting procedures or spectroscopic analysis.

The SFR can be derived from the infrared (IR) emission, since the recently formed stars are usually embedded in dust and gas clouds which absorbe the ultra-violet (UV) light from theses young stars and re-emit at the IR wavelengths; thus the IR emission is a good tracer of the SFR. The most common method to derive SFR from the IR emission is to apply the Kennicutt (1998b) relation, which relates the SFR and the total infrared luminosity (L_{IR}; 8-1000 μm). However, this is a theoretical relation based on the starburst synthesis models of Leitherer & Heckman (1995a) obtained for a continuous burst, solar abundances and a Salpeter Initial Mass Function (IMF), assuming that young stars dominate the radiation f eld throughout the UV-visible and that the far infrared luminosity measures the

bolometric luminosity of the starburst. This physical situation holds in dense circumnuclear starburst that power many IR-luminous galaxies. In normal disk galaxies or early type galaxies, the situation is much more complex as dust heating from the radiation f eld of older stars may be very important. Strictly speaking, as remarked by Kennicutt, the relation above applies only to starburst with ages less than 10^8 yr, while, for other cases, it would be probably better to rely on an empirical calibration of SFR/L_{IR}.

During the PhD, the Herschel Space Observatory was launched into space and the f rst data were ready to be used. The advent of the ESA Herschel Space Observatory, a far-infrared telescope observing at wavelengths that had never previously been explored (from 75 up to 500 μm), allows us to better resolve the IR peak of the SED of star-forming galaxies and therefore to have a more accurate measure of the SFR from the L_{IR} emission. Making use of Herschel data at 100-160 μm from the PEP (PACS Evolutionary Probe) survey (P.I. D. Lutz), sampling the critical far-infrared peak of nearby galaxies, we have tried to empirically derive the relation between the observed L_{IR} and the SFR without associated uncertainties due to extrapolation of the IR peak. To do so, we have analyzed a PEP selected sample of ~500 galaxies in the COSMOS f eld with associated multi-band photometry and 20k zCOSMOS spectral data at $z = 0.1 - 0.46$.

Unfortunately, none of the SFR estimates is totally correct, since all of them are subject to uncertainties due to approximations on the SFR derivations. Although the SFR derived from the Hα emission line is supposed to be one of the better tracers of the young population, thus giving an accurate measure of the SFR, the Hα emission is highly affected by extinction. The Hα emission line luminosity has to be corrected by dust extinction before being used to derive the SFR. Deriving accurate values of extinction from the Hα/Hβ ratio for each galaxy of our sample is of great diff culty as the Hβ emission line cannot be accurately measured for each galaxy. We tried to solve the extinction problem by deriving median extinction values. We constructed median spectra after binning our galaxies in 3 different L_{IR} bins. The median spectra have higher S/N that the single spectra, allowing us to measure the Hβ line with more accuracy. We also made use of Brinchmann et al. (2004) recipes to derive the Hα emission line extinction. These authors propose different extinction values depending on the mass of the galaxies.

We have compared the SFR values derived from L_{IR} emission (using the simple transformation from luminosity to SFR given by Kennicutt 1998) with that obtained

from the Hα emission line using different recipes. We studied how these SFR values compare with each other and how different intrinsic properties of galaxies, such as redshift, mass, metallicity, SSFR or morphology, affect the comparison of both SFR estimates.

The comparison of the SFR indicators at low redshift is crucial to test the validity of the SFR estimates which are often used in high redshift studies. If the SFR values obtained with both methods are in agreement for the low redshift samples, we can extend their validity at higher redshifts. This allows us to derive the SFR of distant galaxies when only the L_{IR} or the Hα information are available, with the assurance that we are not introducing important systematic effects.

Structure of the Thesis

The thesis is organized as follows: In Chapter 1 we give a brief explanation of the galaxy formation theory, from the initial perturbations to the formation of stars in galaxies. In Chapter 2 we explain the main ingredients to study the stellar populations in galaxies, while in Chapter 3 and 4 we study in detail the observed properties of the Late Type Galaxies (LTGs) and the Early Type Galaxies (ETGs), respectively. In Chapter 5 we explain how we have derived the main properties of our IRAC selected sample (photometric redshifts, stellar masses, SFR), considered to study the evolution of the different galaxy classes at high redshift ($1.4 < z < 3.0$) in Chapter 6. In Chapter 7 we show the comparison between the SFR derived from the L_{IR} and the SFR derived from Hα for a PEP selected sample of $\sim$ 500 galaxies and the dependence of this comparison on different galaxy properties. Finally, in the Conclusions, we summarize our main results.

Throughout this thesis we use standard cosmology ($\Omega_m = 0.3, \Omega_\Lambda = 0.7$), with $H_0 = 70$ km s^{-1} Mpc^{-1}. Magnitudes are given in AB system. The stellar masses are given in units of solar masses ($M_\odot$).

CHAPTER 1

Galaxy Formation Theory

UNDERSTANDING how galaxies in the Universe have been formed and evolved during cosmic times is one of the major aims of current astrophysics. However, galaxy formation is a very complicated process involving many orders of magnitude in time and space-scales, with many different physical process taking place, and where also feedback plays a very important role. Therefore, studying these objects in detail requires a multidisciplinary view and a detailed comprehension of all the elements influencing their formation and subsequent evolution.

In order to illustrate the great complexity of the galaxy formation, we show in Fig. 1.1 a flow chart that reflects our current view of galaxy formation with all the various physical interconnected processes. Starting from the cosmological initial and boundary conditions and after gravity instabilities, large mass systems begin to collapse. If cooling is effective, and depending on different physical properties, such as angular momentum, gas instabilities, etc., the formation of the different types of observed galaxies (ellipticals, disk systems...) can roughly be explained. In this Section we aim to give a summary on how, starting form the initial perturbations soon after the Big Bang, matter aggregates in a determined manner giving rise to large structures such as galaxies where the first stars are formed.

1.1 Cosmology

Modern cosmology is based upon the cosmological principle, *i.e.* the hypothesis that the Universe is spatially homogeneous and isotropic, meaning that in the rest

Figure 1.1: Reproduced from Mo et al. (2010). A logic f ow chart for galaxy formation. In the standard scenario, the initial and boundary conditions for galaxy formation are set by the cosmological framework. The paths leading to the formation of various galaxies are shown along with the relevant physical processes. Note, however, that processes do not separate as neatly as this f gures suggest.

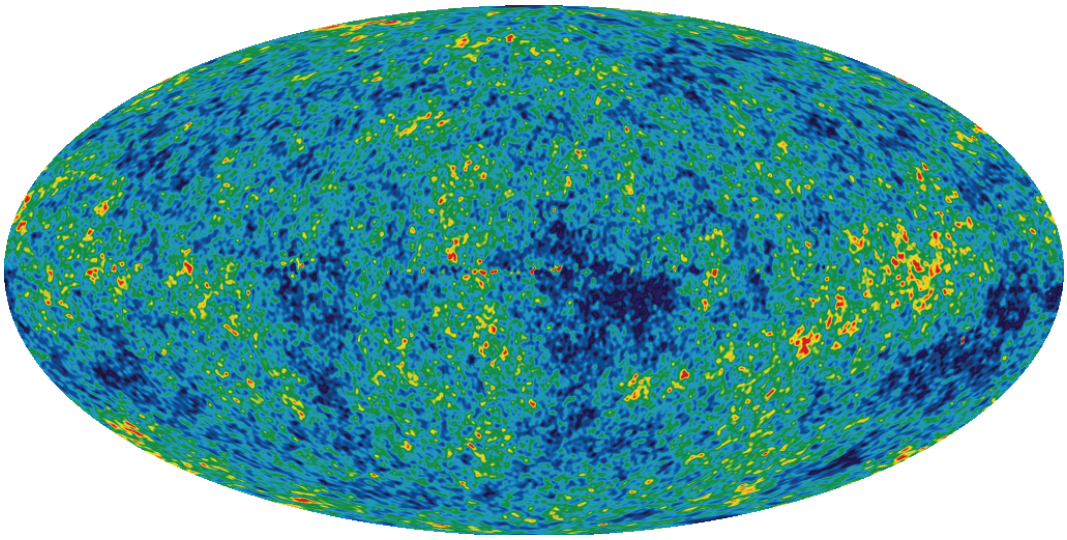

Figure 1.2: CMB map of WMAP data.

system of matter there is no preferred point and no preferred direction. There are many strong and independent observational evidences of the goodness of these assumptions, such as the large-scale distribution of galaxies and the near-uniformity of the Cosmic Microwave Backgroud (CMB) temperature. Results from the COBE mission in 1994 showed that the spectrum of the cosmic background radiation is consistent with a black body at temperature ($2.726 \pm 0.010K$) over more than three decades in wavelength (Mather et al., 1994), showing anisotropies only of the order of $\Delta T/T \approx 10^{-5}$. More recent surveys, such us WMAP (Jarosik et al., 2011; Komatsu et al., 2011) or the Planck satellite (Planck Collaboration et al., 2011), conf rm the picture shown by COBE satellite with an extraordinary precision (see Fig. 1.2)

Another key piece of modern cosmology is the Einstein's theory of general relativity, according to which the structure of space-time is determined by the mass distribution in the Universe. These two assumptions lead to what is known as the standard model of cosmology, that can be completely specif ed by the curvature of the Universe K and the scale factor a(t), which describes the change of the length scale of the Universe with time.

The most popular cosmological model is the so-called ΛCDM model. In this model, the Universe is f at and it consists of three main components: $\sim$ 75% is supposed to be dark energy, $\sim$ 21% is due to 'cold' dark matter and the remaining $\sim$ 4% is due

to the ‘ baryonic’ matter, *i.e*. the protons, neutrons and electrons that make up the visible matter.

The f rst evidence that the Universe may contain dark matter came in 1933, when Zwicky studied the velocities in the Coma cluster, f nding that the total mass required to maintain the system in equilibrium had to be much more than the observed matter. Later studies conf rmed the results by Zwicky discovering that massive halos are required around the Milky Way and other nearby galaxies in order to explain the motions of their satellites.

Three different kinds of dark matter can be postulated: a ‘ hot dark matter’ (HDM) composed by ultra-relativistic particles ($v/c > 0.95$), a ‘ warm dark matter’ (WDM) composed by relativistic particles ($0.1 < v/c < 0.95$), and a ‘ cold dark matter’ (CDM) composed by particles with non-relativistic speed ($v/c < 0.1$). These categories of dark matter are theoretically equally valid. However, both WDM and HDM are characterized by temperatures and speeds too high to match many observed phenomena. For example, they do not properly explain the observed galactic rotational curves and velocity dispersions, neither can they account for the observed weak lensing properties.

The dark energy can be associated to a cosmological constant which causes the Universe to accelerate its expansion. The f rst piece of evidence of the expansion of the Universe came with the Hubble discovery (Hubble, 1929) that the recession velocities of galaxies were related to their distances, demonstrating that our Universe is expanding. Previously, when trying to solve its own equations of general relativity, Einstein found that all the solutions required the Universe to expand or to contract. In order to obtain a static solution, he introduced a cosmological constant into his f eld equations to oppose the standard gravitational attraction. Many years later, in the 1998, two teams independently used the Type Ia supernova data to show that the Universe expansion is accelerating at the present time. The present acceleration requires the introduction of a cosmological constant in the Einstein’s equations that, rather than counterbalancing the attractive effects of normal gravitation, induces an even more rapid expansion.

1.1.1 Density Perturbations

If the cosmological principle held perfectly and the uniformity and isotropy of matter in the Universe were perfect, there would be no structure formation. To

be able to have more and less dense regions, as we observe nowadays, we need some deviations from uniformity at the very beginning of the Universe to induce the subsequent evolution of structures. The answer to this deviation from uniformity can be found in the quantum fluctuations. At very early times (t ~ sec after the Big Bang) the Universe is so dense that the quantum effects are important. The expansion of the Universe generates density perturbations by quantum fluctuations, responsible for the formation of the structures that are observed in today's Universe. The Universe is supposed to have gone through a phase of rapid, exponential expansion, known as inflation. Some inflationary models are able to reproduce the observed properties of large scale structure by assuming that quantum fluctuations in the vacuum energy produce density perturbations responsible of the formation of the large scale structure.

In an expanding Universe dominated by non-relativistic matter (CDM), perturbations grow with time. If we imagine an almost homogeneous Universe with a slightly over-dense region, it is easy to understand that, due to gravitational forces, this region will attract matter slightly stronger that its surroundings, thus producing a denser region which has an ever stronger attraction effect. On the other hand, under-dense regions become less dense as matter flows away from them, and also expand quicker as the gravitational force opposing to the expansion of the Universe is less strong in those regions. This amplification of density perturbations is known as gravitational instability. In a static universe, the amplification is out of control and the density contrast, $\delta\rho/\rho$ grows exponentially with time. The effect of the expansion, prevents the accretion flows, so the resulting growth rate is usually a power law as a function of time $\delta\rho/\rho \propto t^{\alpha}$, with $\alpha > 0$. The value of α depends on the cosmological model. At early times, the perturbations are still in the linear regime ($\delta\rho/\rho \ll 1$) and the size of an over-dense region increases with time due to the overall expansion of the universe. Once the linear regime is broken and the perturbation reaches the over-density ($\delta\rho/\rho \sim 1$) it stops expanding and starts collapsing.

In a universe with both baryonic and dark matter, each initial perturbation contains both ingredients in roughly their universal proportions. When the collapse takes place, the dark matter violently relaxs to form a dark matter halo, while the gas shocks to the virial temperature, T_{vir} [1] and, if the cooling time-scale is slow enough,

[1] T_{vir} is the temperature of an object in virial equilibrium ($2E_K + E_G = 0$, where E_K is the kinetic energy and E_G is the gravitational energy).

may reach hydrostatic equilibrium in the potential well of a dark matter halo. This, as we will see later, is the origin of a galaxy to be formed.

1.1.2 Dark Matter Halos and Gas Cooling

It seems to be conf rmed that galaxies reside in extended halos of dark matter. As we have previously seen, once the density perturbations become non-linear, the dark matter collapses and forms virialized dark matter halos. These halos continue to grow in mass and size by merging with other halos or by accreting material from the neighborhood. At later stages, halos merge together to form a single virialized dark matter halo with an ellipsoidal shape, containing some substructure in the form of dark matter sub-halo. Many recent numerical simulations are able to reproduce the formation of a dark matter halo in a CDM cosmology. In Fig. 1.3 we show a numerical simulation from the cosmological simulation MultiDark (Klypin et al. 2001, Prada et al. 2011) for different redshifts, from z=4.000 up to z=0.000. It can be seen how structures are formed with the cosmic time. At z=0.000 the resulting structure contains different clusters of galaxies. In particular, one of the most massive galactic clusters from the simulation can be observed at z=0.000, with an estimated mass of 2.39×10^{15} $M_{\odot}$.

Since dark matter halos are the host of galaxies, their properties have a direct impact on the galaxy observed properties. Understanding the structure and formation of dark matter halos is fundamental to assess the formation and evolution of galaxies and many recent studies focus on the dark matter halo mass function, density prof les, shapes, angular momentum or large-scale environment. It is not the purpose of this work to give a detailed explanation of all these properties, but it is interesting to remind that dark matter halos and galaxies are intimate related.

Gas cooling is another crucial ingredient in galaxy formation. Depending on the temperature and density of the gas many different processes can take place, like bremsstrahlung emission for very hot ionized gas ($T_{vir} \gtrsim 10^6 K$), excitations and de-excitations at lower temperatures or inverse Compton scattering of CMB photons at high redshifts ($z \gtrsim 6$). As normally these processes (with the exception of the inverse Compton scattering), involve two particles, cooling is generally more effective in higher density regions. After the nonlinear gravitational collapse, the hot gas in virialized halos may be dense enough to effectively cool. If the cooling time is shorter than the dynamical time of the halo, the gas losses pressure support

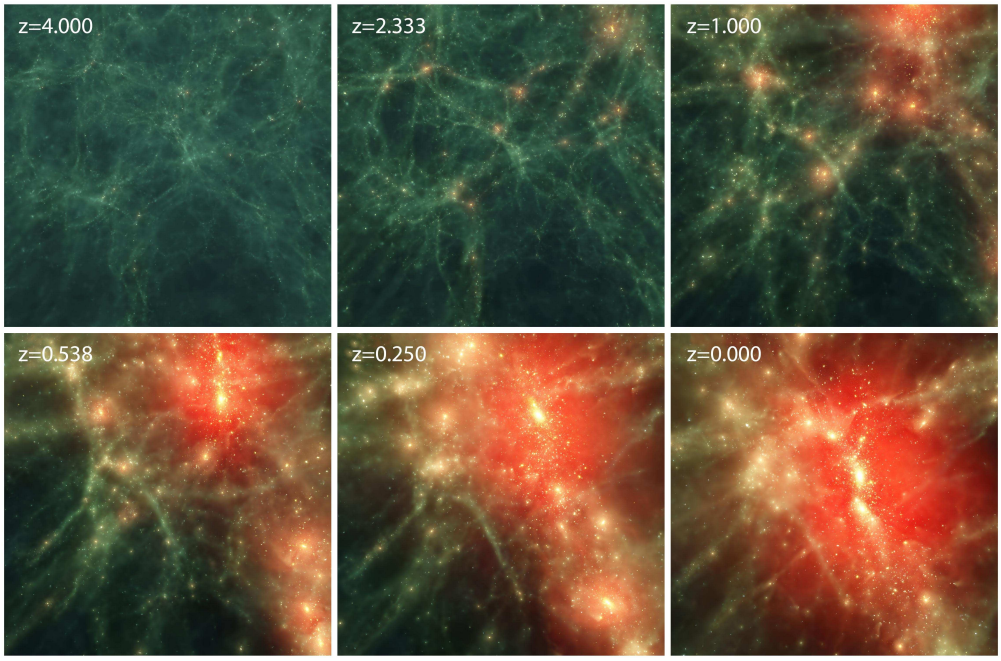

Figure 1.3: Dark matter distribution in the cosmological simulation MultiDark (Klypin et al. 2001, Prada et al. 2011) for different redshift, from z=4.000 up to z=0.000. The region in the f gure is a 6Mpc^3 volume that has been resimulated with high resolution, including gas particles and radiative physics.

and falls towards the center of the halo potential well, increasing its density. When the density of the gas exceeds that of the dark matter in the central region of the halo, the gas becomes self-gravitating and collapses under its own gravity. If the colling is eff cient enough, it causes the gas to catastrophically collapse, leading to the formation of dense clouds of cold gas within which star formation can occur.

1.2 Star Formation in Galaxies

From studies of the Milky Way and nearby galaxies we know that star formation always takes place in dense molecular clouds. CO emission is commonly used to trace the presence of H_2. H_2 is a symmetric molecule, so its associated emission is very weak. CO emission is much easier to detect, so it is used to detect H_2 since it is usually present in regions where there is also H_2. Observations of CO emission from starburst galaxies show that star-formation is associated with large amounts of molecular gas ($10^8 - 10^{10} M_\odot$) conf ned to small volumes of sizes $\lesssim 2$ kpc. To study the star formation process in galaxies is often useful to dive it into 'microphysics', *i.e*. the formation of individual stars in dense molecular clouds, and 'macrophysics', which deals with the formation and structure of molecular clouds in galaxies.

1.2.1 Giant Molecular Clouds

Star formation takes place in the core of giant molecular clouds (GMC). In Fig. 1.4 we show an impressive image of a GMC from the Eagle nebulae taken with the Hubble Space Telescope where star-formation is happening. GMCs of very different sizes and densities have been observed, ranging from the largest clouds with masses of $10^5 - 10^6 M_\odot$, densities of the order of $n_{H_2} \simeq 100 - 500$ cm^{-3} and sizes of a few tens of parsecs, to the smallest 'cores' with masses of $0.1 - 10 M_\odot$ and densities $n_{H_2} > 10^5$ cm^{-3}. However, the star formation eff ciency is very low and star formation seems to happen only in the most massive clumps (given as a result a star cluster) or in the cores of GMC (forming single stars).

GMCs have very homogeneous temperatures (~ 10 K), large line-widths (~ 10 km s^{-1}) indicative of supersonic turbulence and short lifetimes ($\sim 10^7$ yr). In the mass range $10^2 - 10^6 M_\odot$, the masses and velocity widths of individual molecular clouds and clumps is observed to be tightly correlated with their radii:

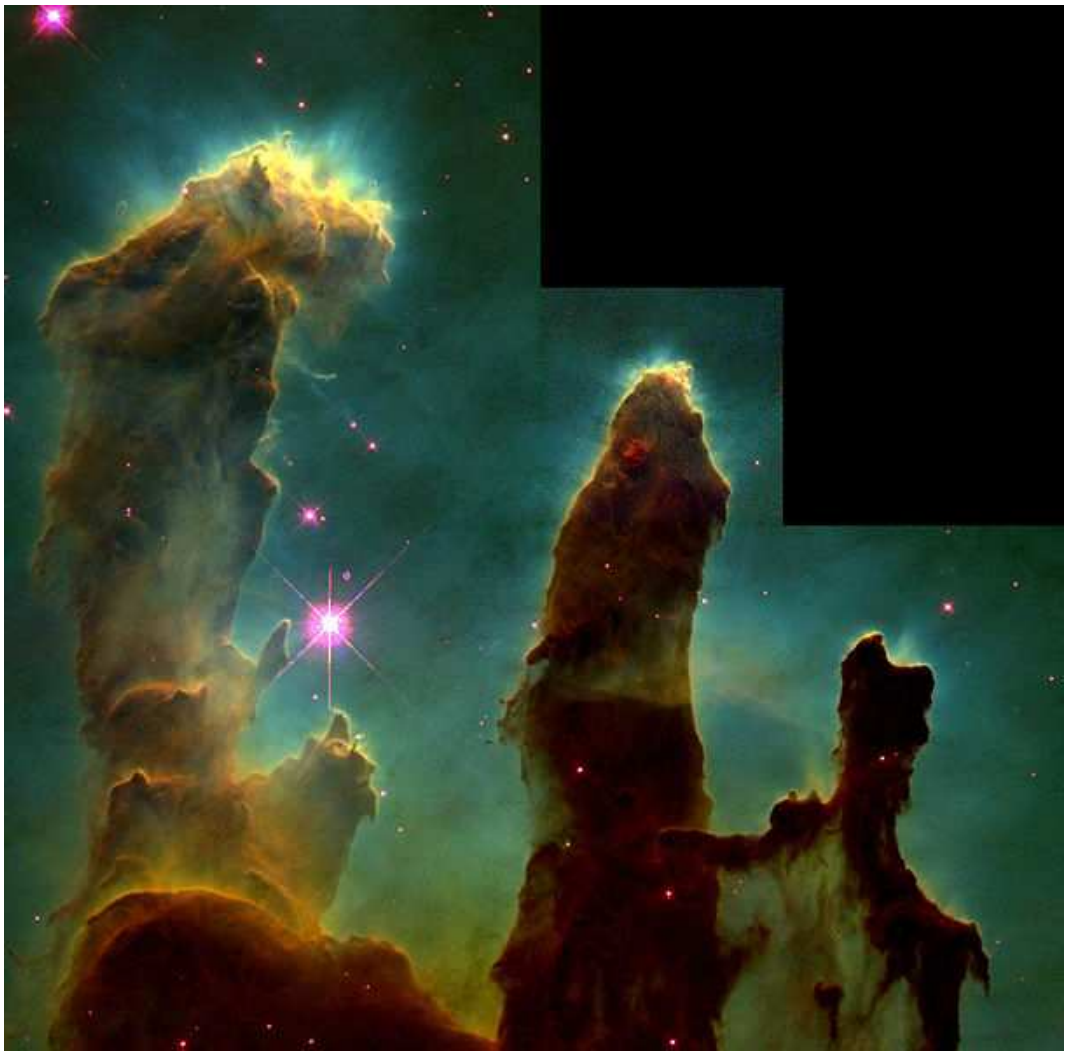

Figure 1.4: Hubble image of a GMC in the Eagle nebulae were stars are being formed.

$$M \propto R^2, \Delta v \propto R^{1/2} \propto \rho^{-1/2} \tag{1.1}$$

Star formation starts when a GMC collapses under its own gravity, thus producing such high densities and temperatures in the center that nuclear reactions can happen, giving rise to a protostar that will become a star at later times. For a GMC to collapse under its own gravity, its mass must exceed the Jeans mass. If we consider the simplest case of a self-gravitating, homogeneous, isothermal sphere of gas, we can derive the Jeans mass, which is the mass for which the gravitational potential energy is higher than the internal thermal energy, causing the cloud to collapse.

Considering the virial theorem $2E_K + E_G = 0$, where E_K is the internal thermal energy and E_G is the gravitational energy. If $E_K < -1/2E_G$ the system collapses, while for $E_K > -1/2E_G$ the system expands. Assuming an ideal gas, its internal thermal energy can be expressed as

$$E_K = \frac{3}{2}NkT \tag{1.2}$$

where N is the number of particles, T is the temperature of the gas and k is the Boltzmann constant. Therefore, the minimum mass for the system to collapse is the Jeans Mass:

$$3NkT < \frac{3GM^2}{5R} \tag{1.3}$$

$$M_J = \left(\frac{5NkTR}{G}\right)^{1/2} \tag{1.4}$$

Considering that N can be expressed in terms of the gas number density for mean mass per particle μ, the gas mass M_g and the particle mass m_p as $N = M_g/\mu m_p$ and that the gas mass is related to the density and size of the GMC ($M_g = 4/3\pi R^3\rho$), we can re-write the Jeans Mass in the form:

$$M_J \propto \rho^{-1/2}T^{3/2}\left(\frac{5k}{G\mu m_p}\right) \tag{1.5}$$

It can also be expressed in terms of the speed of sound c_s and the H_2 column number density N_{H_2}:

$$M_J = \frac{\pi^{5/2} c_s^3}{6(G^3\rho)^{1/2}} \simeq 40 M_\odot \left(\frac{c_s}{0.2 kms^{-1}}\right)^3 \left(\frac{n_{H_2}}{100 cm^{-3}}\right)^{-1/2} \quad (1.6)$$

A more appropriate approximation for molecular clumps and cores is to consider an isothermal sphere in pressure equilibrium with its surrounding. Then, the equivalent mass to the Jeans mass is called the Bonnor-Erbert mass:

$$M_{BE} = 1.182 \frac{c_s^3}{(G^3\rho)^{1/2}} = 1.182 \frac{c_s^4}{(G^3 P_{th})^{1/2}}, \quad (1.7)$$

where $P_{th} = \rho c_s^2$ is the surface pressure (Bonnor 1956; Ebert 1957). GMCs have usually masses exceeding the Jeans mass or the Bonnor-Erbert mass, meaning that they should collapse and subsequently form stars on a free-fall time τ_{ff} [2]

$$\tau_{ff} = \left(\frac{3\pi}{32 G\rho}\right)^{1/2} \simeq 3.6 \times 10^6 yr \left(\frac{n_{H_2}}{100 cm^{-3}}\right)^{-1/2} \quad (1.8)$$

However, this is much shorter that the inferred lifetimes of the GMCs, indicating that these must be supported against gravity by some non-thermal pressure. The most probable sources of non-thermal pressure are turbulence and magnetic fields. Both turbulence and magnetic fields can prevent the GMCs from collapsing, thus regulating the overall star-formation efficiency.

The formation of GMCs is still a controversial topic. The most basic picture is that they are the cold gas parcels in a three phase medium where hot ($\sim 10^6$ K), warm ($\sim 10^4$ K) and cold ($\sim 10^2$ K) gas phases coexist as a result of thermal instability. However this seems to be insufficient to produce GMCs but gives rise only to molecular gas. More important is the gravitational instability, which can be triggered by thermal instability. Turbulence may play a very important role in GMCs formation and it has been suggested that GMCs may be transient objects forming at converging points of the larger-scale turbulent flow of the galaxy. Most of the molecular gas in spiral galaxies is found in their spiral arms. Spiral arms are supposed to be density waves that compress the gas clouds, thus inducing thermal and gravitational instability and hence GMCs formation. Galaxy interactions and mergers are also of great importance for the triggering of star formation, as gas can be compressed by shocks when two galaxies merge and the energy of the merger is converted in turbulent motion.

[2] The free-fall time is the characteristic time that would take a body to collapse under its own gravitational attraction, if no other forces existed to oppose the collapse.

Once GMCs have been formed some process must regulate the star formation efficiency (SFE) within them. It is known that in disk galaxies the angular momentum due to the rotation prevents from gravitational collapse, thus suppressing possible star formation. This seems to be one of the major differences between spiral galaxies and starbursts: some merging event removes angular momentum and allows a great SFE in the starbursts. It was generally accepted in the 1980's that magnetic fields had a great influence in the regulation of the SFE, although this picture has been recently debated by observational and theoretical shortcomings. Supersonic turbulence also affects the SFE within GMCs in two different ways: turbulence motion increases the velocity dispersion of the gas, thus suppressing gravitational collapse. On the other hand turbulent shocks compress the gas, promoting gravitational collapse by increasing the gas density. Another very important mechanism that controls SFE is self-regulation. Star formation itself may prevent from further star formation due to galactic winds, supernovae explosions or OB massive stars ionization that destroys GMCs. However, this processes may also promote star-formation due to the compression of the surrounding gas.

1.2.2 The Formation of Individual Stars

Once a GMC has been formed and the gravitational collapse cannot be prevented, individual stars are formed in the central cores of GMCs. It is beyond the scope of this thesis to give a detailed explanation of this formation process, very complicated and not very well understood. However, we will briefly explain how this event happens.

First of all, the dense cores in GMCs collapse due to gravity, forming a highly stratified density profiles within which protostars form. Then, in-falling material from the original cloud is accreted, leading to the growth of the protostar. The material with high angular momentum are first accreted into a disk and then transported inwards by viscous processes. Further accretion may be prevented or reduced by the protostellar feedback, such as outflow and radiation, that tends to disperse the gas around a protostar. Finally, the protostar keeps on contracting until its internal energy and temperature are high enough to produce nuclear reactions in its nucleus, when the protostar becomes a star with a particular emitted luminosity, temperature and mass. The mass of a star is the most important parameter in the subsequent evolution of a star's life. Very high mass stars burn their internal material

very quickly and have much shorter life times than lower mass stars, as we will see in more detail in Sect. 2.1.

1.2.3 The Kennicutt-Schmidt Law

To characterize the star-formation rate (SFR) of a galaxy, the value $\dot{\Sigma}_\star = \dot{M}_\star / area$ is often used, *i.e.* the mass in stars formed per unit time per unit area. Another important quantity is the gas consumption time $\tau_{SF} = \Sigma_{gas}/\dot{\Sigma}_\star$ (with Σ_{gas} being the gas surface density), which gives an idea of the time a galaxy would need to convert all of its gas into stars if it continued forming stars at the same rate. Relating these parameters to galaxy intrinsic properties, such us density, temperature, magnetic f eld, etc. is very complicated because of our lack of knowledge in the physical processes involved. However, some empirical laws have conf rmed the relation between gas density and star formation rate density.

The f rst to investigate this issue was Schmidt (Schmidt, 1959), who found a power law in the form

$$\dot{\Sigma}_\star \propto \Sigma_{gas}^N, \tag{1.9}$$

with N $\sim$ 2 for the observed distribution of HII and stars perpendicular to the Galactic plane. This relation is known as the Schmidt law. The analysis was extended to star-formation in normal spiral galaxies, as well as to starbursts galaxies by Kennicutt (1998b). Interestingly, different kinds of galaxies seem to follow the Schmidt law with a very small scatter (see Fig. 1.5). The best f t to the observational data gives the Kennicutt-Schmidt law that can be expressed as:

$$\dot{\Sigma}_\star = (2.5 \pm 0.7) \times 10^{-4} \left(\frac{\Sigma_{gas}}{M_\odot pc^{-2}} \right)^{1.4\pm0.15} M_\odot yr^{-1} kpc^{-2} \tag{1.10}$$

This Kennicutt-Schmidt law is interpreted as an indication that the SFR is controlled by the self-gravity of the gas. In that case, the SFR is proportional to the gas mass divided by the time scale for gravitational collapse. If $\tau_{ff} \propto 1/\sqrt{\rho}$, then

$$\dot{\rho}_\star = \varepsilon_{SF} \frac{\rho_{gas}}{\tau_{ff}} \propto \rho_{gas}^{1.5}, \tag{1.11}$$

where ε_{SF} is a measure of the eff ciency of the star formation. For galaxies with same scale hight this implies $\dot{\Sigma}_\star \propto \Sigma_{gas}^{1.5}$, in good agreement with the Kennicutt-Schmidt law.

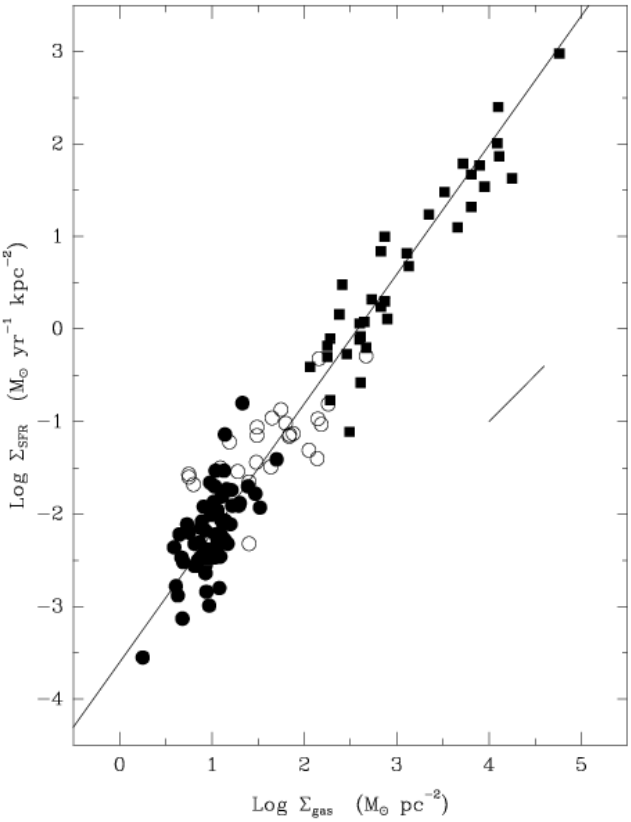

Figure 1.5: Reproduced from Kennicutt (1998b). Composite star-formation law for normal disk galaxies (filled circles), starbursts (squares) and centers of normal galaxies (open circles). The solid line corresponds to the Kennicutt Schmidt law (Eq. 1.10).

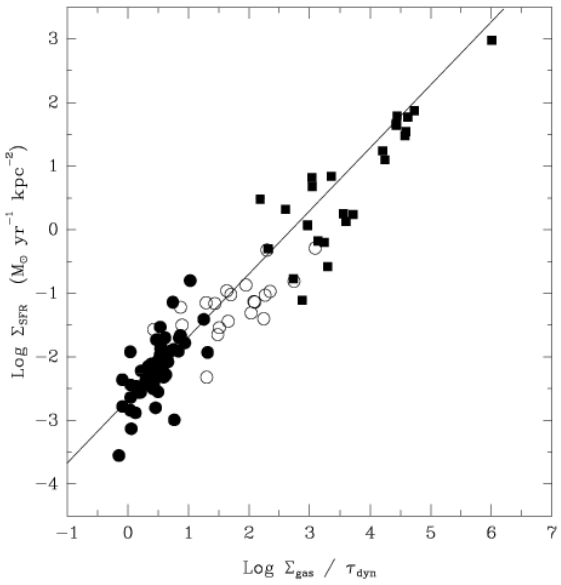

Figure 1.6: Reproduced from Kennicutt (1998b). SFR per unit area as a function of Σ_{gas} divided by the dynamical time. Symbols like in Fig. 1.5. Solid line is the best f t to the data (Eq. 1.12).

Kennicutt (1998b) also found a very tight correlation between $\dot{\Sigma}_\star$ and Σ_{gas}/τ_{dyn}, were $\tau_{dyn} = 2\pi R/V_{rot}(R)$. This is shown in Fig. 1.6, were the solid line represents the best f t to the data:

$$\dot{\Sigma}_\star \approx 0.017\Sigma_{gas}\Omega, \tag{1.12}$$

with Ω the circular frequency, implying that about 10% of the available gas is consumed by star formation per orbital time.

CHAPTER 2

Analysis of Stellar Populations in Galaxies

GALAXIES are mainly composed by stars. To understand the properties of observed galaxies it is then very useful to be able to predict the different observational properties of a certain stellar population. Stellar population synthesis models put together all the relevant information known of a given stellar population and reproduce the expected spectra of the composite population so that it can be compared with the observations to recover the physical properties of galaxies.

2.1 Stellar Evolutionary Tracks

Stellar evolution is one of the best understood topics in the present day astrophysics. Although there are still some uncertainties remaining, the evolution of stars with time has been deeply studied and we are able to predict the properties of stars of different masses and chemical compositions at different times. Stellar evolution is however, a very complex and wide aspect of astrophysics, and we will not enter into any detail in this work.

It is very important to be aware that, for physical reasons, the evolution of a star is almost completely determined by its initial mass and chemical composition. Thus, given these two quantities, a stellar evolution model yields all the properties of a star at any time t after its birth. The two most important properties of a star changing with time are its luminosity, L, and its effective temperature, T_{eff}. Stars

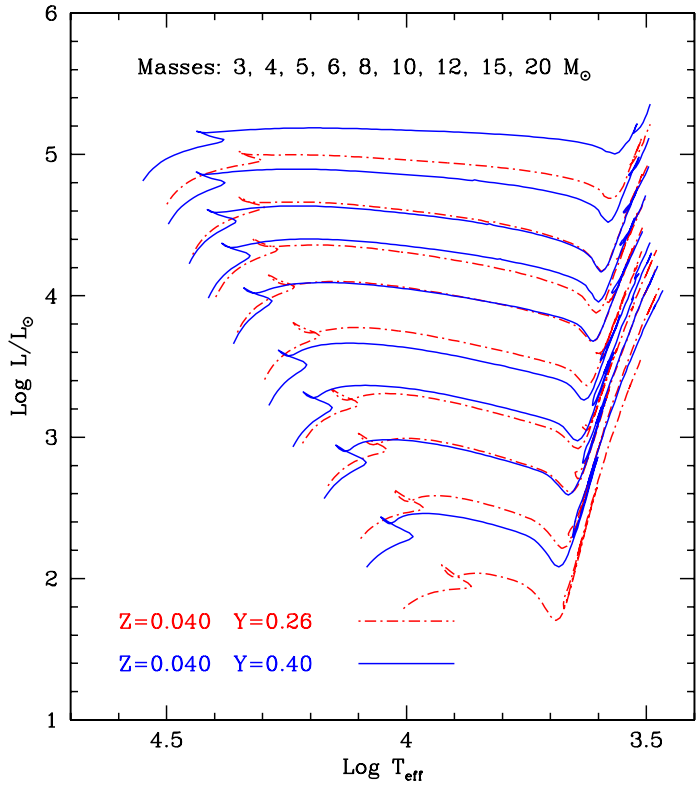

Figure 2.1: Reproduced from Bertelli et al. (2009). Evolutionary tracks in the HR diagram for the composition Z=0.040, Y=0.26 (dot-dashed line) and Z=0.040, Y=0.40 (solid line).

evolutionary tracks are usually represented in the so-called Hertzsprung-Russell (H-R) diagram, representing the color-magnitude plane, related to the L and T_{eff} of the stars. An example of evolutionary track from the Padova group can be seen in Fig. 2.1 for stars of different masses and metallicities.

In a very simplif ed manner, we can summarize that stars suffer a pre-main sequence evolution before entering to the main sequence, were the star spends most of its lifetime and were the burn of the internal H occurs in the nucleus of the star. The post-main sequence evolution strongly depends on the star mass, with the most massive stars evolving faster and entering the Red Giant Branch (RGB) and the Asymptotic Giant Branch (AGB) to end their lives as neutron stars or black holes (for stars with M > 8 $M_{\odot}$), while the less massive galaxies evolve slower and may end up converted in white dwarfs.

Once the evolutionary tracks of stars are known, theoretical spectra can be constructed. The values of the effective temperature T_{eff} and surface gravity g

of a star allow us to determine its density, temperature and ionization, assuming the atmosphere to be in both thermal and hydrostatic equilibrium. Sophisticated stellar-atmosphere codes including radiative transfer are used to predict the spectra of stars with wide ranges of properties.

2.2 Initial Mass Function

Once we know what is the output emission of light from a given star along its life, *i.e.* its spectra, it is fundamental to know what kind of stars are formed within a starburst. Then the emitted light from the whole population is just the integrated spectra of each single star. The nature of the formed stars is often expressed in the form of the Initial Mass Function (IMF).

The IMF $\phi(m)$ is def ned so that $\phi(m)dm$ is the relative number of stars that were originally created in the mass range $m \pm dm/2$. It is frequently assumed to be a simple power law:

$$\phi(m) = cm^{-x} \tag{2.1}$$

The IMF is supposed to be a continuous function and is usually normalized as:

$$\int_{m_l}^{m_u} m\phi(m)dm = 1M_{\odot} \tag{2.2}$$

with m_u and m_l the upper and lower limits for stars, which normally take the values $m_u \simeq 100$ M$_{\odot}$ and $m_l \simeq 0.08$ M$_{\odot}$.

In principle, the IMF could vary from galaxy to galaxy and within the galaxy itself. Observations of the Milky Way seem to suggest that the IMF is independent of the galaxy location. It is generally accepted that the IMF is universal, not only in the Milky Way, but also in other galaxies. However, current observational constrains are subject to high uncertainties, thus leaving as an open question the universality of the IMF.

Some of the most commonly used IMFs are the Salpeter (1955), Chabrier (2003) or Kroupa (2002) IMFs, although many other IMFs can be found in literature (*e.g.*, Tinsley 1980, Scalo 1986 or Scalo 1998).

The f rst determination of the IMF in the solar neighborhood was estimated by Salpeter (1955), who obtained

$$\phi(m)dm \propto m^{-b}dm,\ b = 2.35 \tag{2.3}$$

A more recent analysis of the stars near the sun form Kroupa (2002) gives a similar shape as the Salpeter IMF, but f attens at lower masses:

$$\phi(m)dm \propto \begin{cases} m^{-2.7}\ (1.0M_{\odot} < m < 100M_{\odot}) \\ m^{-2.3}\ (0.5M_{\odot} < m < 1.0M_{\odot}) \\ m^{-1.3}\ (0.08M_{\odot} < m < 0.5M_{\odot}) \\ m^{-0.3}\ (0.01M_{\odot} < m < 0.08M_{\odot}) \end{cases}$$

An analysis of the IMF in diverse stellar components of the galaxy, such as disk stars, bulge stars or stars in globular clusters, has been done by Chabrier (2003) f nding that all these IMFs have similar forms. For disk stars the IMF is:

$$\phi(m)dm \propto \begin{cases} m^{-1.35}\ (m > 1.0M_{\odot}) \\ exp{-}[log(m/0.2M_{\odot})]^2/0.6\ (m < 1.0M_{\odot}) \end{cases}$$

In Fig 2.2 (Fig. 1a from Romano et al. 2004) we show the values of different IMFs. The different slopes of the laws produce different spectral energy distributions, so having a good approximation of this function is fundamental to study the properties of observed galaxies.

2.3 Spectral Synthesis

Knowing the spectral emission of stars of given masses and chemical composition, assuming an universal IMF and a given metallicity, it is possible to reproduce the expected emission of an ensemble of stars and, as an extension, of a galaxy. Suppose that $\Psi(t)$ is the star formation rate and $\mathcal{L}_{\lambda}^{cp}$ is the luminosity per unit stellar mass of all stars of a coeval population of age τ, were

$$\mathcal{L}_{\lambda}^{cp}(\tau) = \int \mathcal{L}_{\lambda}(m,\tau)\frac{\phi(m)}{M_{\odot}}dm \tag{2.4}$$

m is the mass of a star, $\phi(m)$ is the normalized IMF and $\mathcal{L}_{\lambda}(m,\tau)$ is the luminosity of a star with initial mass m at age τ.

Then, the luminosity of the galaxy at a given time t at some given wavelength λ can be written as:

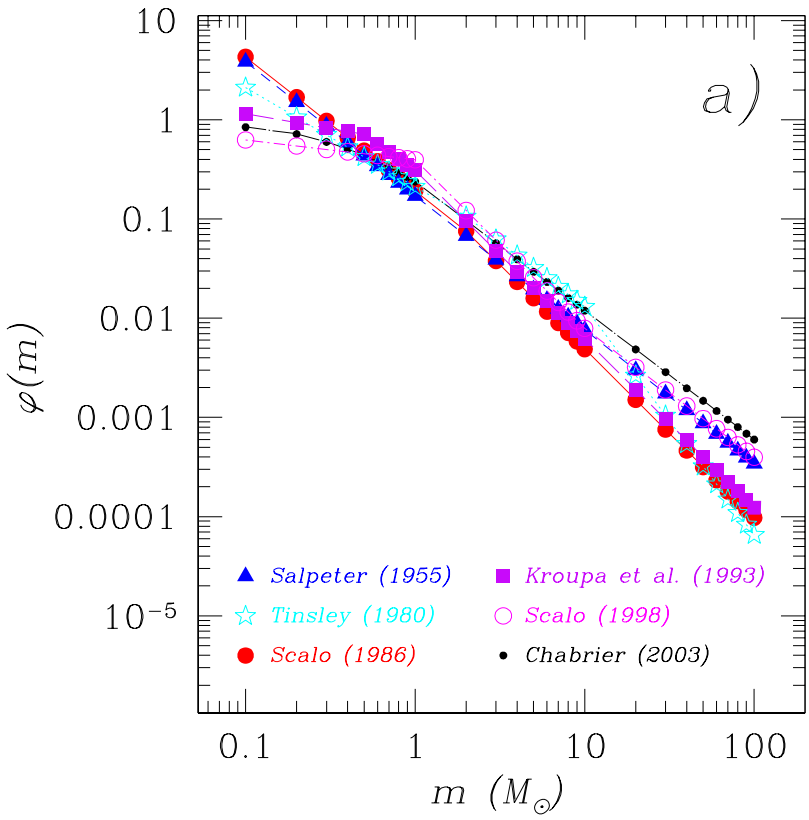

Figure 2.2: Reproduced from Romano et al. (2004). Stellar IMF according to Salpeter (1955), Tinsley (1980), Scalo (1986), Kroupa et al. (1993), Scalo (1998) and Chabrier (2003)

$$L_\lambda(t) = \int_0^t \mathcal{L}_\lambda^{cp}(t - t')\Psi(t')dt' \tag{2.5}$$

Therefore, once the star-formation rate $\Psi(t)$ and $\phi(m)$ are specif ed, we can calculate the Spectral Energy Distribution (SED) of a galaxy at any given time by summing the spectra of coeval populations with different ages.

To better understand the most important features of coeval stellar populations SEDs of different ages, we show in Fig. 2.3 the theoretical SEDs of a coeval stellar population as a function of age, with τ ranging from 0 to 11 Gyrs. In very young populations ($< 10^7$ yr) the spectra is completely dominated by the blue main sequence stars, thus resulting in a very strong UV emission due to their high effective temperatures. At later times, the most massive stars begin to leave the main sequence and become red giants, producing a drop in the UV f ux and an increase in the near IR part of the spectrum. From 10^8 to 10^9 yr, the UV f ux continues to drop while the near IR f ux is maintained by the AGB stars. The small increase in the UV at ages later than 3-10 Gyr is produced by low mass stars entering their post-AGB phase.

The simplest application of spectral synthesis modeling is to consider a star-formation history given by a delta function $\Psi(t) \propto \delta(t-t_{form})$. This kind of evolution is often called passive evolution, and could be considered as a an approximation for the evolution of the elliptical galaxies that we will study in more detail (see Chapter 4).

The colors of a passive evolving populations change with age in a very similar way to the spectra of coeval populations at different ages. The broad-band luminosities decrease with age, but this decrease is much more rapid in the bluer bands because of the disappearance of bright main-sequence stars and super-giants. Stars with masses > 1.25 $M_\odot$ have lifetimes shorter than 4 Gyr, so any coeval population older than ~ 4 Gyr contains only stars with $\lesssim 1\ M_\odot$. Besides, since the temperature of the giant branch stars does depend weakly on the age, old stellar populations have red colors that change very slow with time.

Unfortunately, the evolution of real galaxies is not as simple as the passive evolution. Instead, the star-formation history of a galaxy can be very different, ranging from a single burst with subsequent passive evolution, a continuous burst or a burst exponentially declining with time ($\psi(t) \propto e^{-t/\tau}$). The star-formation can stop and be triggered again (for example from mergers or tidal interactions) and

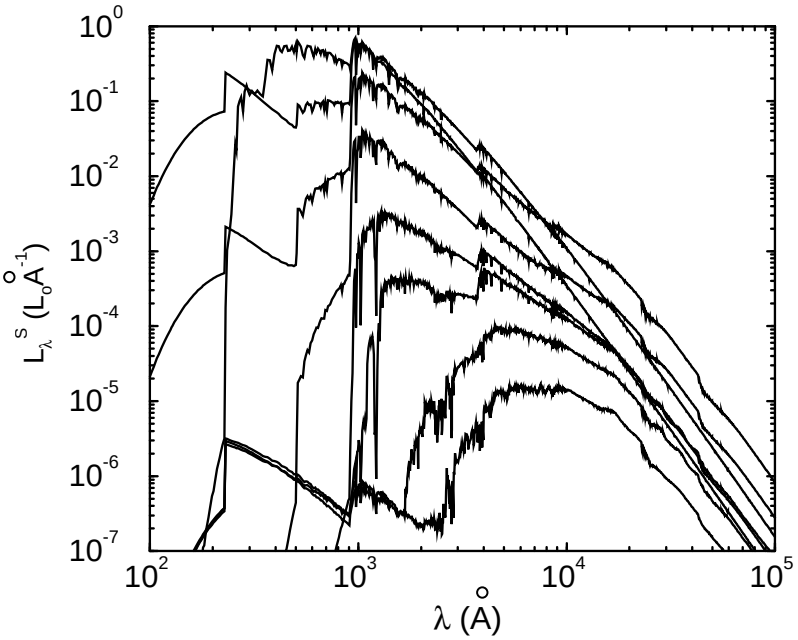

Figure 2.3: Reproduced from Kneiske et al. (2002). Spectral energy distributions (SEDs) of a coeval stellar population as a function of age τ. The specif c luminosity of the evolving stellar population is normalized to one solar mass. The stellar models assume standard solar composition. Shown are the SEDs for τ = 0, 0.0038, 0.00724, 0.0138, 0.07187, 0.28612, 1.434, and 11 Gyrs (from top to bottom, based on calculations by Bruzual A. & Charlot 1993).

this process can happen more than once. The inclusion of these complicated star-formation histories makes it more diff cult to unequivocally interpret the spectra of a given galaxy, although general properties can be usually recovered.

2.3.1 Spectral Features

There are some parts of the spectrum of galaxies that contain more information than the rest of it. These are the spectral discontinuities and the spectral indices.

The spectral discontinuities are clearly observed from Fig. 2.3 as pronounced discontinuities in the spectra at 912 Å (Lyman break) and at 4000 Å (the D(4000) break). The Lyman break of an stellar population increases rapidly at 10^7 yr, when the most massive stars move off the main sequence. At 10^9 yr more UV photons are generated due to the stars in the post-AGB phase and the break is no longer detectable. For a galaxy in which the stars have formed over an extended period of time, the change in the amplitude of the Lyman break is smaller due to the spread in stellar ages of the stars of the population. Therefore, a large Lyman break is a signature of a young population that has been produce on a short burst. Unfortunately, absorption due to the neutral hydrogen in the intergalactic medium between the observed galaxy and the observer can produce similar features in the galaxy spectra, thus complicating the interpretation of the Lyman break. The 4000 Å break is used to predict the stellar age of a galaxy as it is controlled by the most massive stars in the main sequence and continuously increases with time from 10^7 yr to about 10 Gyr. However, it also depends strongly on the metallicity, again making it more diff cult to determine the galaxy properties if the chemical composition of the galaxy is unknown.

Based on the theoretical spectra obtained from the spectral synthesis models, one can describe several spectral indices, like for example the Lick indices, which contain information about the abundance of certain elements and about the age of the stellar population. Each index is def ned by a central band of width $\Delta\lambda_0$ and two side bands. The side-band intensity, I_s, is def ned as the mean intensity over the two side bands. The central band intensity, I_c, is the mean intensity over the central band. Examples of these spectral indices are Hβ, Hδ_A, Mgb, Fe_1, Fe_2, Mg_1, Mg_2, etc. A systematic study of these indices can help to understand the given properties of a stellar population such as age and metallicity.

2.3.2 Age-Metallicity Degeneracy

The metallicity, usually noted as Z in the literature, is another parameter that affects the emitted spectra of a stellar population. Stars with higher metallicities evolve faster. Thus, an increase in the amount of metals contained in a galaxy produces redder colors in its spectra. A population of stars with very high metallicity has a spectral energy distribution with a very similar shape to that of an older population with less metallic content. In fact, it has been demonstrated that galaxies with the same $\tau Z^{3/2}$ have identical colors. This is known as the age-metallicity degeneracy and is one of the most important limitations in the study of galaxy populations. Making use of additional information, such as Hα and Hβ emission lines (more sensitive to the stellar age) or metal line strengths as Mg_b, Fe_1 or Fe_2 (sensitive to the metallicity), the age-metallicity degeneracy can be broken.

2.4 Emission and Absorption by the Inter-Stellar Medium

Real galaxies are not only made by stars, but are embedded in the inter-stellar medium (ISM) composed by dust and gas. The ISM affects the light emitted by the stars of a galaxy both through emitting and absorbing processes.

2.4.1 Emission

Emission by the ISM can ascribe mainly to HII regions or to heated dust. An HII region is a large, low-density cloud of partially ionized gas in which star formation has recently taken place. The young blue stars emit at the ultraviolet wavelengths, thus ionizing the surrounding gas. In fact, HII regions are named for the large amount of ionized atomic hydrogen that they contain, referred to as HII (HI region being neutral atomic hydrogen). In a HII region a hydrogen nucleus can recombine with a free electron to form a hydrogen atom. If the resulting atom is in an excited state, the atom will cascade to the ground state, emitting line photons. If the optical depth of the HII region is small, they will escape the HII region. In the opposite case the recombination photons will be absorbed, causing further ionizations or excitations of the gas.

Another source of emission are dust grains heated when absorbing photons which are then re-radiated in the mid to far-IR wavelengths. There are three main

components in the dust emission curve. Big grains ($a > 100$Å), whose emission ca be approximated to that of a gray body at a given temperature; small grains ($a \lesssim 100$Å), which contribute signif cantly to the emission in the mid-IR ($\lambda \sim 20 - 50\mu$ m); and Polycyclic Aromatic Hydrocarbons (PAHs) which dominate the emission at $\lambda \sim 3 - 10\mu$m, producing strong bands at 3,6,8 and 11 μm due to vibrational modes.

2.4.2 Dust Extinction

Dust in galaxies absorbs part of the light emitted by the stars. Dust extinction is higher at shorter wavelengths, causing the resulting spectra to be redder. To apply the dust extinction effect to the spectra of a galaxy the extinction law , *i.e*. the variation of extinction with wavelength, must be known

The dust extinction along a given optical line of sight is usually described by means of the optical depth τ_λ [1]. The observed intensity at a given wavelength I_λ and the intensity that would be observed in the absence of dust extinction $I_{\lambda 0}$ can be related to the optical depth in the form:

$$I_\lambda = I_{\lambda 0} e^{-\tau_\lambda} \tag{2.6}$$

The dust extinction is usually expressed in the form of an empirical extinction law, $k(\lambda)$ where

$$k(\lambda) \equiv \frac{A_\lambda}{E(B-V)} \equiv R_V \frac{A_\lambda}{A_V} \, , \tag{2.7}$$

$A_\lambda = (2.5 log e)\tau_\lambda$ is the change in magnitude at wavelength λ due to the extinction, $E(B-V) \equiv A_B - A_V$ is the color excess between the B and V bands and R_V is def ned as $A_V/E(B-V)$.

The extinction law depends on the physical properties and composition of the dust grains, as well as on the geometry of the dust cloud. Normally, empirically derived extinction laws are used, like the extinction laws from the Milky Way (MW, Allen 1976), from the Large Magellanic Clouds (LMC, Fitzpatrick 1985) or from the Small Magellanic Clouds (SMC, Prevot et al. 1984). In Fig. 2.4 we show the

[1] The optical depth τ_λ is a measure of how opaque a medium is to radiation passing through it. It is measured along the vertical optical path dz: $\tau_\lambda = \int_0^z K dz$, where K is the extinction coeff cient.

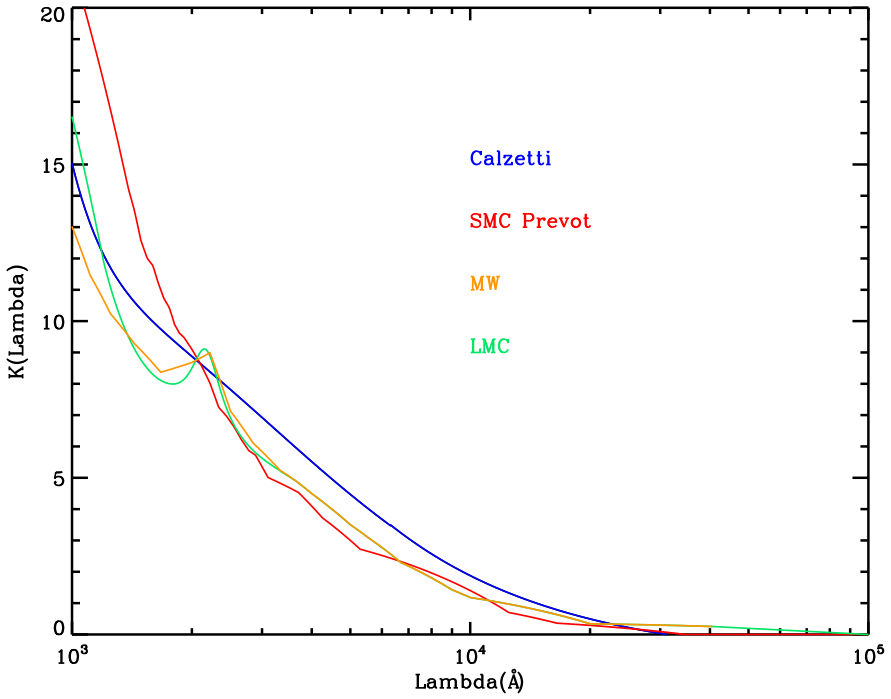

Figure 2.4: Extinction curves k(λ) for different extinction laws commonly used.

extinction curves derived for the MW, LMC and SMC, as well as the derived extinction law by Calzetti et al. (2000) for starburst galaxies.

Both the extinction laws for the MW and the LMC show a strong feature at 2175 Å, which is supposed to be produced by graphite dust grains. The peculiarity of the SMC extinction law by Prevot et al. (1984) is the lack of the graphite 2175 Å bump. The non detection of this bump is probably related to the large under-abundance of carbon in the SMC. The most commonly used attenuation curve in high redshift studies is the law derived by Calzetti as a purely empirical result from a sample of near Starburst (SB) galaxies. As it can be observed from Fig. 2.4 the Calzetti extinction law, as the SMC law, does not show the 2175 Å bump.

CHAPTER 3

Late Type Galaxies

In this Chapter we introduce the concept of bimodality, which separates the galaxies in two main groups: Late Type Galaxies (LTGs), usually associated with blue colors and disk morphologies, and Early Type Galaxies (ETGs), related to red colors and elliptical morphologies. We also discuss some of the observed properties of LTGs, such as the SFR-Mass relation and explain the methods usually used to derive the SFR values.

3.1 The Existence of Bimodality in Observed Galaxies

The first classification of galaxies was made by Hubble (1926) and was purely based on the morphological properties of the galaxies. He ordered the galaxies in a morphological sequence, the now called Hubble sequence (Fig. 3.1), dividing the galaxies into four broad classes:

- Elliptical galaxies: These galaxies have elliptical shapes and smooth elliptical isophotes. They are subdivided into En, where the integer n reflects the ellipticity of the galaxy (n=10(1 – b/a); a and b the lengths of the semi-major and semi-minor axes).

- Spiral galaxies: These galaxies are thin disks with spiral arm structures. They are subdivided into barred and normal spirals, depending on the presence of a barred structure in the central part of the galaxy. A further division on each branch into a, b or c is based on the fraction of light in the central bulge, the tightness with which the spiral arms are wounded and the degree to which the

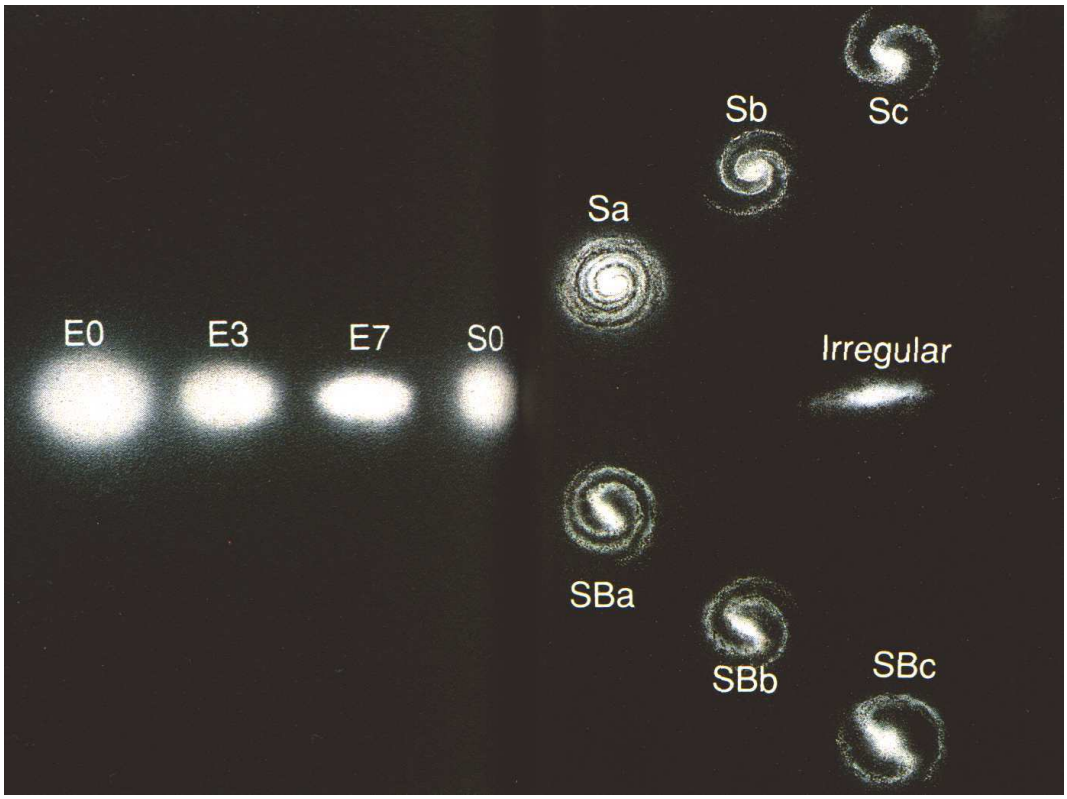

Figure 3.1: Hubble galaxy classif cation Scheme.

spiral arms are resolved into stars, HII regions and dust.

- Lenticular or S0 galaxies: These galaxies are an intermediate class between ellipticals and spirals.
- Irregular galaxies: These galaxies have no ordered structure and are usually asymmetric, showing irregular shapes.

Astonishingly, this pure morphological classif cation is deeply related to the stellar content and physical properties of the galaxies, with the elliptical or early type galaxies (ETGs) showing almost no star formation, a rather old stellar population and red colors, while most of the star formation is known to take place in blue disk systems, also known as late type galaxies (LTGs). Irregular galaxies are mostly the result of recent mergers, thus containing also merger induced star forming regions. Other intrinsic properties such as the dynamical structure or kinematics are also very different for different morphological types.

Studying local samples of galaxies a clear bimodality is seen in the local Universe in terms of galaxy properties (e.g., color, morphology, star formation, and spectral

features; Kauffmann et al. 2003; Baldry et al. 2004; Brinchmann et al. 2004). Galaxies in the local Universe exhibit distinctive bimodal color distributions, suggesting that different evolution histories exist for galaxies lying on the two sequences (Menci et al. 2005; De Lucia et al. 2007). The existence of this bimodality is confirmed to exist up to redshift $z \sim 1$ (Bell et al. 2004; Weiner et al. 2005) and possibly up to $z \sim 2$ (Giallongo et al. 2005, Cirasuolo et al. 2007, Cassata et al. 2008).

In Fig. 3.2 we show the color distribution (left panel) of a sample of galaxies at $0.5 < z < 0.9$ studied by Pozzetti et al. (2010) from the 10k sample in the COSMOS field. The bimodality is clearly observed in terms of colors (left panel) and specific star formation rates (SSFR, right panel).

These two main classes of galaxies are also often referred as the 'blue cloud' and 'red sequence' galaxies. The red sequence galaxies include mostly passive galaxies with an elliptical morphology (*e.g.* Cassata et al. 2007), but also a significant fraction of dust-extincted star-forming galaxies and Spi/Irr galaxies with quenched star formation. Both populations can be separated in terms of colors, spectral features or morphological types. However, these classifications do not completely overlap. For example, in a study of local $z \sim 0$ ETGs from the Sloan Digital Sky Survey (SDSS), out of the morphologically selected ETGs, 70% satisfy also the color selection. The correlation between color and morphology selection persists at high redshifts, as shown by Bell et al. (2004). At $z \sim 0.7$ about 85% of color-selected, red sequence galaxies are also morphologically early type (E/S0/Sa). Besides, there are intermediate objects, supposed to be the transition between actively star-forming galaxies and passive galaxies, located in the color-color diagram in what is known as the green valley (*e.g* Pozzetti et al. 2010).

3.2 Late Type Galaxy Properties

As we have already mentioned, Late Type Galaxies have blue colors and disk morphologies, usually presenting different components on its structure (thin disk, thick disk, bulge, stellar halo). The stellar populations are far more complicated that those of elliptical galaxies and show significant on going star formation. Their star formation histories are clearly inconsistent with a single burst, and are generally modeled as exponentially declining function of time. Moreover, the different

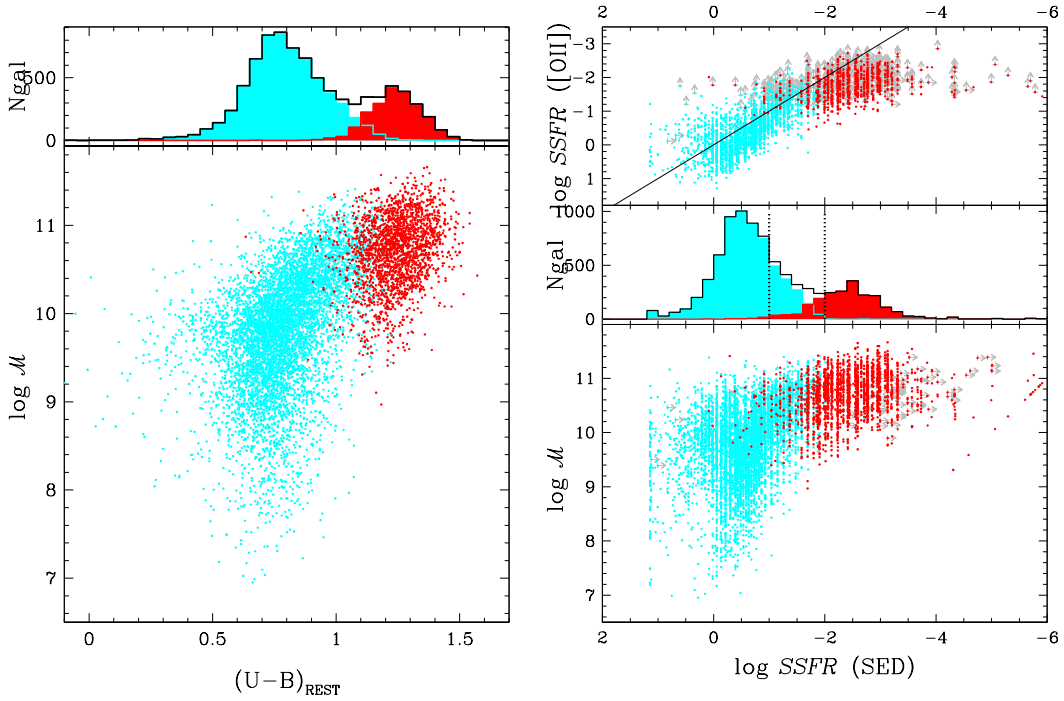

Figure 3.2: Reproduced from Pozzetti et al. (2010). Left f gure: the upper panel shows the $U - B$ rest-frame color distribution of galaxies. The bottom panel shows the color-mass diagram. Right f gure: $SSFR$ of galaxies with different photometric types. The upper panel shows the comparison between estimates from the SED-f tting and from [OII] for galaxies in the range $0.5 < z < 0.9$. The middle panel shows the $SSFR$ distribution of galaxies, along with the two dotted lines used to separate active from quiescent (log($SSFR$ [Gyr^{-1}])$= -1$) or from passive galaxies (log($SSFR$ [Gyr^{-1}])$= -2$). The bottom panel shows the log($SSFR$[Gyr^{-1}])-mass diagram. Red dark and light cyan colors represent SED-ETGs and SED-LTGs respectively.

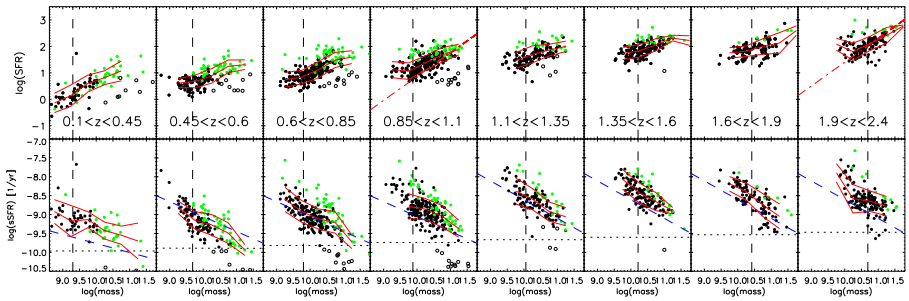

Figure 3.3: Reproduced from Rodighiero et al. (2010). Relation of the stellar mass as a function of SFR (*top panels*) and SSFR (*bottom panels*). Green points represent PACS detected sources for which the L_{IR} has been computed including all data points. Black points are MIPS 24μm sources undetected by PACS: in this case the L_{IR} has been derived from the SED f tting procedure limited at 24μm. Open symbols are passive sources with color mag[24]-mag[3.6]<0.5. Also reported with red lines the average of the relations and the $\pm 1\sigma$ limits. The red dot-dashed lines correspond to literature observed relations between mass and SFR: at $z \sim 1$ the GOODS relation by Elbaz et al. (2007); at $z \sim 2$ the relation for star-forming *BzK* by Daddi et al. (2007). Vertical dashed lines mark the mass completeness limit as a function of z, and the horizontal dotted lines indicate the inverse of the age of the universe at the mean redshift of each bin. The dashed blue lines in the bottom panels show the relations derived from our stacking analysis on PACS maps.

components of a disk galaxy seem to have different stellar populations. While the stellar populations of the bulge and the stellar halo are dominated by old stars, the disk component is populated by stars of various ages and metallicities. Besides, thick disk stars are older and more metal poor than thin disk stars.

3.2.1 The Star Formation Rate-Mass Relation

One of the most important properties of blue, star forming galaxies is the tight correlation observed between the stellar mas and the SFR, also known as the Main Sequence of star forming galaxies. This was clearly observed at $z = 0$ (Noeske et al., 2007) and $z = 1$ (Elbaz et al., 2007). Daddi et al. (2007) found that a relatively tight stellar mass-SFR relation is already in place at $z = 2$, with a scatter of 0.16 dex in the SSFR. A recent work based on PEP Herschel data by Rodighiero et al. (2010) found the existence of positive correlations between the SFR and the stellar mass at all redshifts up to $z = 2.4$, although the SFR-Mass relation seems to be more robust at $z < 1$ (see upper panel in Fig. 3.3). The authors also studied the relation

between the SSFR and the stellar mass, finding a negative trend at all redshifts, although presenting a quite large scatter (lower panel in Fig. 3.3). They also found that the mean SSFR of star forming galaxies rises with redshifts, implying that galaxies tend to form their stars more actively at high redshifts. Besides, the most massive galaxies at any redshift have the lowest SSFR, meaning that they are the fastest stellar mass assemblers, in agreement with the so-called downsizing scenario (Cowie et al., 1996).

3.3 Star Formation Diagnostics

The star formation contains significant information on the population of a certain galaxy and it is a key parameter when studying galaxy formation and evolution. Many methods have been developed to estimate the star formation rate of a galaxy, although many uncertainties are still remaining. In this section we will explain some of the most commonly used methods to derive SFR, trying to give a physical explanation and to comment their advantages and disadvantages. For a more detailed discussion on the topic see the review by Kennicutt (1998a).

3.3.1 Ultra-Violet Continuum

The most massive stars have lifetimes much shorter than the typical age of the galaxy. Since the most massive stars emit most of their energy in the UV continuum, the UV part of the spectrum is dominated by young stars, so that the SFR scales linearly with UV luminosity. The optimal wavelength range is 1250–2500 Å, longward of the Lyα forest but short enough to minimize spectral contamination from older stellar populations. Although these wavelengths are inaccessible from the ground for local galaxies ($z < 0.5$), the region can be observed in the redshifted spectra of galaxies at $z \sim 1$–5.

The conversion between the UV luminosity over a given wavelength interval and the SFR can be derived using the synthesis models. It is appropriate to assume that the SFR has remained constant over timescales that are long compared to the lifetimes of the dominant UV emitting population ($<10^8$ yr), in the 'continuous star formation' approximation. Considering a Salpeter (1955) IMF with mass limits 0.1 and 100 $M_\odot$ the calibration between UV and SFR yields (Kennicutt, 1998a):

$$\text{SFR}\ (M_{\odot}\, yr^{-1}) = 1.4 \times 10^{-28}\ L_{\nu}\ (\text{ergs s}^{-1}\ \text{Hz}^{-1}). \tag{3.1}$$

This calibration is valid for galaxies were the burst duration is $\sim 10^8$ yr or longer. For a shorter burst, Eq. 3.1 may underestimate the SFR because the star-formation timescale is overestimated.

The most problematic aspects of using an UV-SFR calibration are the effect of the IMF and the dust extinction. Since the UV luminosity is dominated by stars with $M \gtrsim 5$ $M_{\odot}$, the conversion from UV to SFR is very sensitive to the shape of the IMF. Beside, most of the SFR occurs in obscured regions by dust clouds. As we have seen in Sect. 2.4.2, shorter wavelengths are more strongly affected by dust extinction. Therefore the UV luminosity must be corrected by dust extinction before transforming it into SFR.

3.3.2 Recombination Lines

The nebular lines effectively re-emit the integrated stellar luminosity of galaxies short-ward the Lyman limit, so they provide a direct, sensitive probe of the young massive stellar population. Many recombination lines can be used to estimate SFR, like Hβ, Pβ, Brα and Brγ, although the most popular is the Hα emission line.

The conversion factor between the ionizing f ux and the SFR is usually computed using an evolutionary synthesis model. Only stars with masses > 10 $M_{\odot}$ and lifetimes <20 Myr contribute signif cantly to the integrated ionizing f ux, so the emission lines provide a nearly instantaneous measure of the SFR, independent of the previous star formation history. For solar abundances and a Salpeter IMF, the conversion between Hα and the SFR is given by (see Kennicutt et al. 1994, Madau et al. 1998):

$$\text{SFR}\ (M_{\odot}\, yr^{-1}) = 7.9 \times 10^{-42}\ L(H\alpha)\ (\text{ergs s}^{-1}) \tag{3.2}$$

However, as for the UV calibration, the main limitation is that a great part of the light emitted by young stars, which mostly reside within or behind clouds of gas and dust, is absorbed by dust and then re-emitted at longer wavelengths. To properly calculate the SFR form Hα emission line an extinction correction must be applied to take this effect into account. This method is also affected by the shape of the IMF as the Hα luminosity is a measure of the formation rate of very massive stars.

3.3.3 Forbidden Lines

For sources at $z > 0.5$ the Hα emission line is redshifted out of the visible window so other emission lines have to be used as quantitative SFR tracers. Unfortunately the Hβ and the higher order Balmer emission lines are so weak that they are poor SFR diagnostics.

The strongest emission feature in the blue is the [OII]λ3727 forbidden-line doublet. The luminosities of forbidden lines are not directly coupled to the ionizing luminosity, and they are affected by the metallicity and the ionization state of the gas. However, the excitation of [OII] is sufficiently well behaved that it can be calibrated empirically (through Hα) as a quantitative SFR tracer, with the following calibrations (Kennicutt, 1998a):

$$SFR\,(M_{\odot}\,yr^{-1}) \approx (1.4 \times 10^{-41}\,L[OII]\,(\text{ergs s}^{-1}), \tag{3.3}$$

As with Eq. 3.1, 3.2, the observed luminosities must be corrected for extinction. Besides, since this relation is calibrated through Hα, it includes the previously mentioned uncertainties, as well as its own intrinsic uncertainties.

3.3.4 Far-Infrared Continuum

As already mentioned, most of the star-formation takes place in dense dust clouds were stars are born. The light form these young stars, absorbed by the dust, is re-emitted at IR wavelengths. Therefore, the SFR can also be derived from the IR emission of the galaxies. In this case the calibration adopts the form (Kennicutt, 1998b):

$$\text{SFR}\,(M_{\odot}\,yr^{-1}) = 4.5 \times 10^{-44}\,L_{FIR}\,(\text{ergs s}^{-1}) \tag{3.4}$$

This is a theoretical relation based on the starburst synthesis models of Leitherer & Heckman (1995b) obtained for a continuous burst, solar abundances and a Salpeter (1955) IMF, assuming that young stars dominate the radiation field throughout the UV-visible and that the FIR luminosity measures the bolometric luminosity of the starburst. This physical situation holds in dense circumnuclear starbursts that power many IR-luminous galaxies. In the disk of normal galaxies or early type galaxies, the situation is much more complex as dust heating from the radiation field of older stars may be very important. Strictly speaking, as remarked by Kennicutt (1998b),

the relation above applies only to starburst with ages less than 10^8 years while, for other cases, it would be probably better to rely on an empirical calibration of SFR/L_{IR}.

One of the scopes of this thesis work is precisely to empirically calibrate the SFR-L_{IR} relation making use of recent Herschel data. In Chapter 7 we analyze in detail a far-IR selected sample of 474 star-forming galaxies and we compare the SFR derived from the IR emitted light using Eq. 3.4 with the SFR derived from Hα luminosity corrected by extinction (Eq. 3.2). We study in detail how different intrinsic properties of the galaxies affect the SFR estimates derived from the IR continuum emission. We also investigate if galaxies with different morphological types follow Eq. 3.4.

CHAPTER 4

Early Type Galaxies

In this Chapter we aim to give an overview of the main observed properties and the evolution pattern of early type galaxies (ETGs), which are a fundamental piece to put constrains on cosmological models.

4.1 Early Type Galaxy Properties

ETGs at $z \sim 0$ are known to be rather simple and homogeneous systems, with similar morphologies and colors and following tight scaling relations such as the fundamental plane or the color-magnitude relation. In Fig. 4.1, we show the contribution to the total stellar mass by red and blue galaxies in the various mass bins, as well as the contributions to the total number of galaxies, as derived from the local mass function of Baldry et al. (2004). Although ETGs represent only the 17% of the total number of galaxies, their mass accounts for $\sim$ 57% of the total mass. Besides, $\gtrsim$ 80% of the stellar mass in ETGs belongs to galaxies more massive than $\sim 3 \times 10^{10}$ $M_{\odot}$. With spheroids holding the major share of stellar mass in galaxies, they are a key piece for understanding galaxy formation and evolution in general. In this Section we aim to describe some of the most important observed properties of the ETGs population.

4.1.1 The Color-Magnitude Relation

As already mentioned, ETGs have red colors. Many studies have shown that the colors of ETGs are tightly correlated with their luminosities, in the sense that more luminous galaxies are redder. In Fig.4.2 we show the color-magnitude relation for

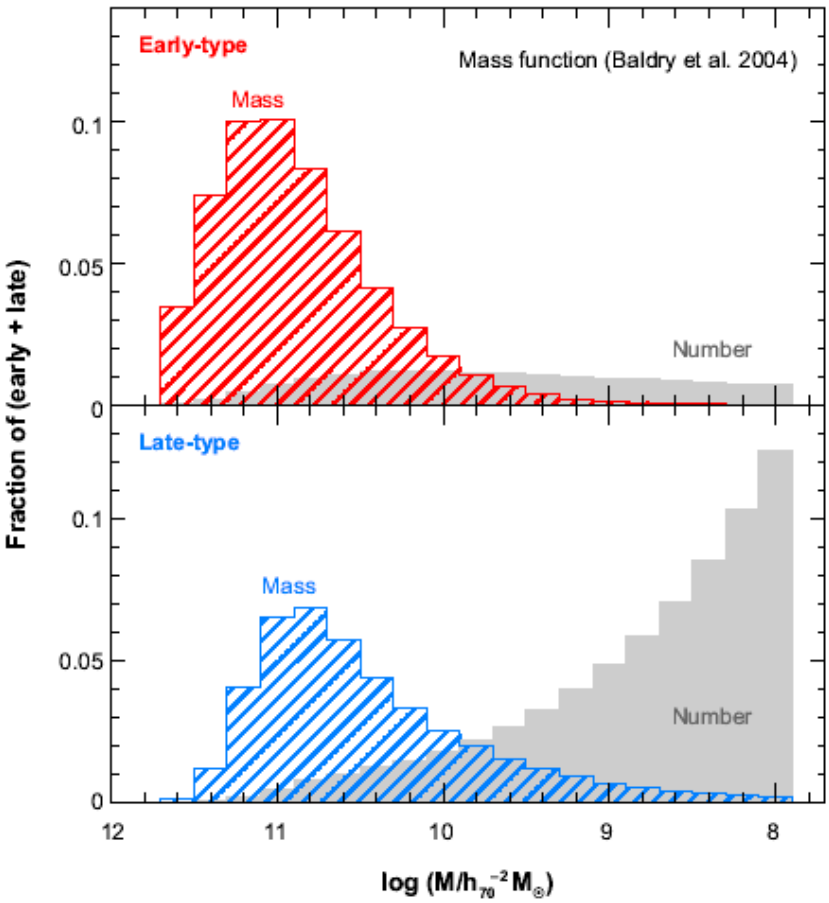

Figure 4.1: Reproduced from Renzini (2006). Contribution to the total stellar mass and to the number of galaxies by early-type (red) and late-type (blue) galaxies in the various mass bins, derived from the best-fit in mass functions of Baldry et al. (2004).

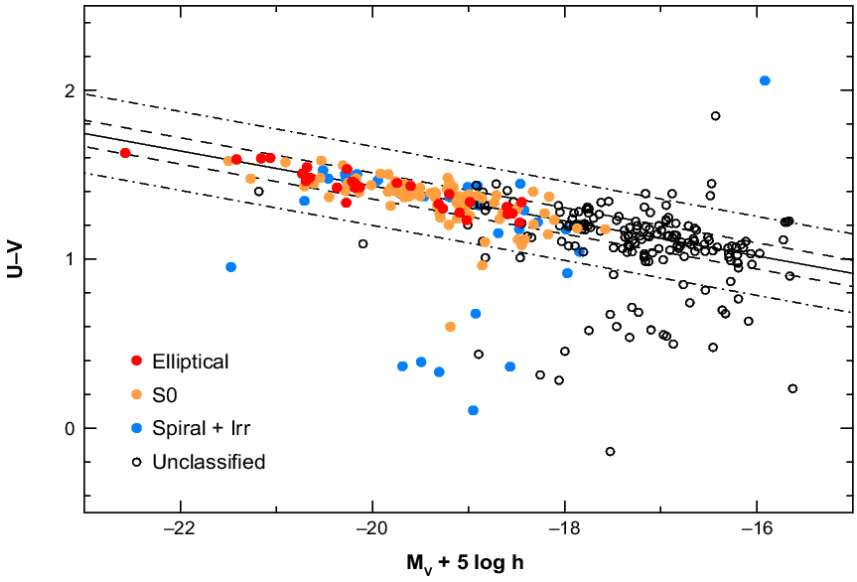

Figure 4.2: Reproduced from Renzini (2006). The $(U-V)-M_V$ color-magnitude relation for galaxies that are spectroscopic members of the Coma cluster (Bower et al., 1999).

spectroscopic galaxies of the Coma cluster studied by Bower et al. (1999).

Unfortunately, the interpretation of this relation is severely impeded by the age-metallicity degeneration. Taking the naive assumption that all ETGs have the same metallicity, then the color-magnitude relation implies that more massive galaxies are older. However, using additional data to break this degeneracy, recent studies (*e.g.*Kodama & Arimoto 1997, Graves et al. 2009) have demonstrated that more luminous ETGs are both redder and older, with the slope of the color-magnitude relation mainly driven by metallicity, while the small amount of scatter mainly ref ects that ETGs have old, passively evolving stellar populations.

4.1.2 The Fundamental Plane

Three main parameters relate the structural/dynamical properties of ETGs to their stellar content: the effective radious R_e, the central velocity dispersion σ and the luminosity L (or equivalently the effective surface brightness $I_e = L/2\pi R_e^2$). ETGs obey a tight scaling relation occupying a region in the (R_e, σ, I_e) space similar to a plane, know as the fundamental plane (FP):

$$R_e \propto \sigma^a I_e^b \tag{4.1}$$

where the exponents a, b depend on the specif c band to measure the luminosity. The projection of the FP over the (R_e,I_e) plane generates the Kormendy relation (Kormendy, 1977), while the projection over the (σ, L) plane is known as the Faber-Jackson relation (Faber & Jackson, 1976).

The existence of a FP implies that ETGs are well-virialized systems, have self-similar structures and contain stellar populations that must follow tight age and metallicity constraints.

4.1.3 Absorption Line Indices

Making use of absorption line indices, like the Lick indices discussed in 2.3.1, the age-metallicity degeneration can be broken. Thomas et al. (2005) studied 124 ETGs and compared their Lick indices with SSP models, showing that the Mg-σ relation is mainly driven by metallicity, with similar contributions from the α/Fe ratio (23%) and age (17%). In addition, there is a weak indication that ETGs galaxies in more dense environments have older stellar populations. The authors also found that more massive ellipticals are older, more metal enriched and more enhanced in α elements, implying that more massive ellipticals have formed their stars on a shorter time-scale.

4.2 The Formation of Elliptical Galaxies

Elliptical galaxies are less ordered systems than disks galaxies, suggesting that their formation was followed by violent relaxation. There are two main proposed theories to explain the formation of elliptical galaxies: the monolithic collapse and the hierarchical merger.

4.2.1 The Monolithic Collapse Scenario

In the monolithic collapse scenario elliptical galaxies form in a single intense starburst at high redshift at the same time as they collapse to equilibrium, then following a passive evolution. This idea comes from the fact that all elliptical galaxies have very similar properties and old evolved stellar populations. Depending on the collapse and star-formation timescales, the system can loose radiative energy or not.

In the most extreme dissipationless case, all the gas is transformed into stars prior to or during the collapse. Given the sizes and masses of observed ellipticals, these should imply that these galaxies must have been formed at $z \sim 20$, in a great conf ict with observations, which suggest that only a very small fraction of stars was formed before $z \sim 6$. Besides, under these assumption, violent relaxation cannot separate between stars and dark matter, thus producing the collapse of the total mass. This, again, is not in agreement with the observed matter distribution of elliptical galaxies, where most of the stars occupy a small central region surrounded by large dark matter halos. In the case that the star-formation timescale is comparable or longer than the collapse, then dissipation can occur during the collapse, so the gas can separate from dark matter at the center of the potential well before turning into stars.

The monolithic collapse assumes that the f nal assembly of an elliptical galaxy occurs simultaneously with the formation of the bulk of its stars in a short time interval. Normal elliptical galaxies seem to have old stellar populations with a mean age of 10 Gyr or more. This would imply that the formation events should have happened before $z \gtrsim 2$ and that galaxies should have evolved passively thereafter. However, as explain in Sect. 4.3, the total mass density in massive, passive galaxies is a factor of $3-4$ lower at $z \sim 1$ than it is today, meaning that at least 70% of present-day ellipticals were still forming stars or not yet assembled at z=1. Another conf ictive point is the observed evolution in size. Passive galaxies at $z \gtrsim 1.5$ seem to have much smaller sizes than present-day elliptical galaxies with same mass values (*e.g.* Daddi et al. 2005, van Dokkum et al. 2008), in disagreement with a purely passive evolution. Therefore, the simple monolithic collapse scenario does not seem to be able to explain many of the observed properties of elliptical galaxies.

4.2.2 The Hierarchical Merger Scenario

In the merger scenario, f rst introduced by Toomre (1977), star-formation is supposed to happen only in disk systems and all elliptical galaxies are the result of the merger of two or more galaxies. The f rst assumption is plausible since star formation in the local Universe seems to be restricted to the disks of spirals. To asses the second assumption the remnant of a merger between two galaxies has to resemble present-day ellipticals and the merger rate has to be consistent with the $z = 0$ population.

Hydrodynamical simulations have shown that the result of a merger does strongly depend on the mass ratio of the galaxies merging, their angular momentum or the event being dissipational or not. For example, it has been suggested that massive ellipticals are the remnants of dissipationless (also called dry, because they are mergers of progenitors without much gas) mergers of elliptical galaxies, while their less massive counterpart require dissipational (also called wet) mergers.

Since the merger scenario predicts two or more galaxies to merge to form a new elliptical galaxy, and given that the progenitor galaxies have independently evolved forming stars over extended periods of time, it could be expected the remnant to have stars of different ages, in contradiction with the homogeneous old stellar populations observed in elliptical galaxies. However, if mergers happen early, the evolution of the stellar population is almost indistinguishable from an old SSP. Besides, data suffer from progenitor bias. If the progenitors of a present-day elliptical galaxy were spirals, these would not be included in observed samples of high-redshift ellipticals, causing evolution to appear more passive than it actually is.

Detailed galaxy formation models in the hierarchical CDM framework show that the predicted scatter in the color-magnitude relation is small, as observed. These models also predict galaxies in dense environments to form their stars earlier than galaxies in low-density environments. Since galaxy clusters correspond with the highest peaks in the primordial density f eld, their dark matter halos collapse earlier, producing more rapid mergers.

One of the most important problems when comparing results from hierarchical merging simulations and observed properties of galaxies come with the so-called downsizing scenario. Observations shows that most massive (elliptical) galaxies have older stellar populations and that most massive galaxies were already in place at high redshifts (see Sect 4.3). In the hierarchical models the most massive halos assembly later with time. If stars form when the assembly of the galaxy takes place, then the most massive galaxies should have younger populations. However, this is not the case. Although more massive halos assemble later, their progenitors form earlier, so the stellar population of a massive halo can be old.

Two improvements have been included in the hierarchical models that help reproducing the observed data. First, the appearance of the new currently popular ΛCDM cosmology reduced the merger rate with respect to the Einster-de

Sitter cosmology previously used. Second, more recent models include feedback mechanisms that prevent star-formation. These feedback mechanisms from active galactic nucleus (AGN) or galactic winds, which prevent gas from cooling in massive halos, help reproducing the observed trend between mass and stellar age. Other aspects, such as the metallicity gradients, have been successfully reproduced by the hierarchical formation scenario models.

As a conclusion, the most favored present theory for the formation of elliptical galaxies is the hierarchical merger scenario in the ΛCDM cosmology. However, there are many open issues and the high redshift ETGs population must be studied in more detail to put more constraints on the formation and evolution models.

4.3 The Observed Evolution of Early and Late Galaxy Types

A key piece to understand the formation and evolution of galaxies is to study their galaxy stellar mass function (GSMF), *i.e*. how the number of galaxies of a given mass changes with cosmic time. In order to investigate the observed excess of faint blue galaxies at high redshitfts, incompatible with non evolutionary models, many redshift surveys were carried out in the mid-1990 out to $z \sim 1$ using 4-m class telescopes (*e.g*. Lilly et al. 1995, Ellis et al. 1996). Further surveys, such as the deep data from the HST, the Hubble Deep Field (HDF), confirmed that the galaxy population is evolving with redshift.

Stellar mass assembly in galaxies subdivided by spectral and morphological types, as well as by star formation activity has been investigated at $z > 0$ by many authors (e.g., Bundy et al. 2005, Franceschini et al. 2006, Pannella et al. 2006).

In one of the most recent works by Pozzetti et al. (2010), the authors used 10k spectroscopic data from the COSMOS field up to $z \sim 1$ to investigate the total GSMF, as well as the contributions of early- and late-type galaxies, defined by different criteria (broad-band spectral energy distribution, morphology, spectral properties, or star formation activities). In Fig. 4.3 we show the Galaxy Stellar Mass Function by galaxy types, based on the photometric classification (left panel) and the morphological classification (right panel) from Pozzetti et al. (2010). They found that the number density of blue or spiral galaxies with $M > 10^{10} M_{\odot}$ remains almost constant, while the most extreme population of star-forming galaxies at intermediate/high mass is rapidly decreasing in number density with cosmic time.

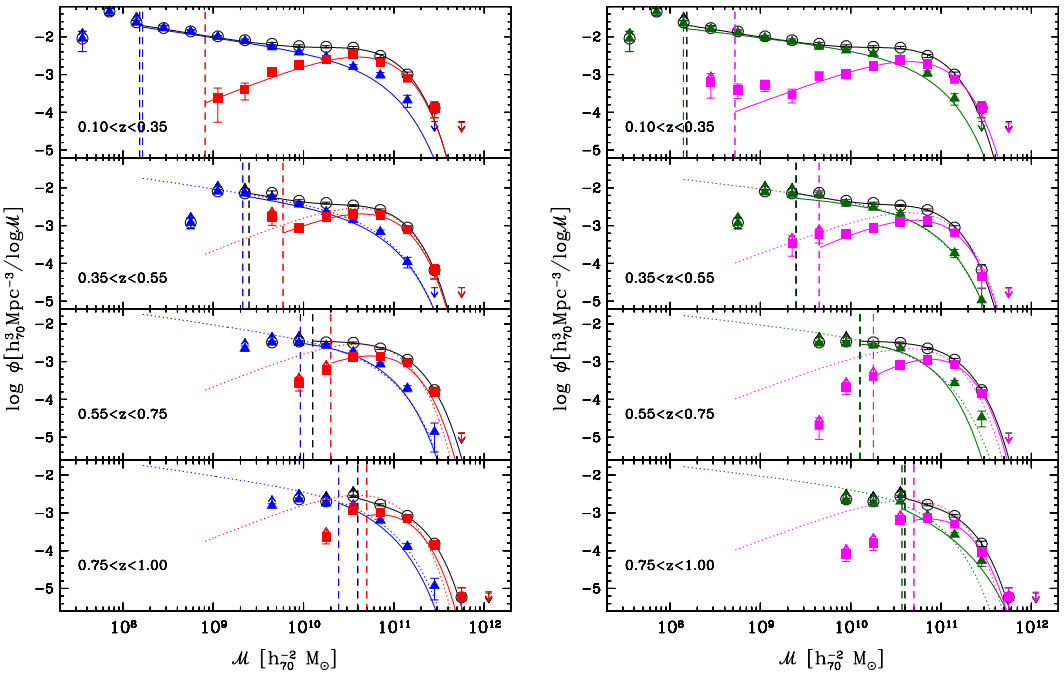

Figure 4.3: Reproduced from Pozzetti et al. (2010). Galaxy stellar mass function by galaxy types. Left panel: GSMFs by photometric types (E/S0 as red squares, early and late spirals plus irregular as blue triangles, total population as empty black circles). Right panel: GSMFs for morphological types (ellipticals and bulge dominated galaxies as magenta squares and disk and irregular galaxies as dark green triangles). In both panels, points represent the $1/V_{max}$ determination, while continuous lines are the Schechter fits. Dotted lines reported in each panel, as a reference, are the Schechter fits to the first redshift bin. Dashed vertical lines represent the mass limit for the corresponding redshift bin.

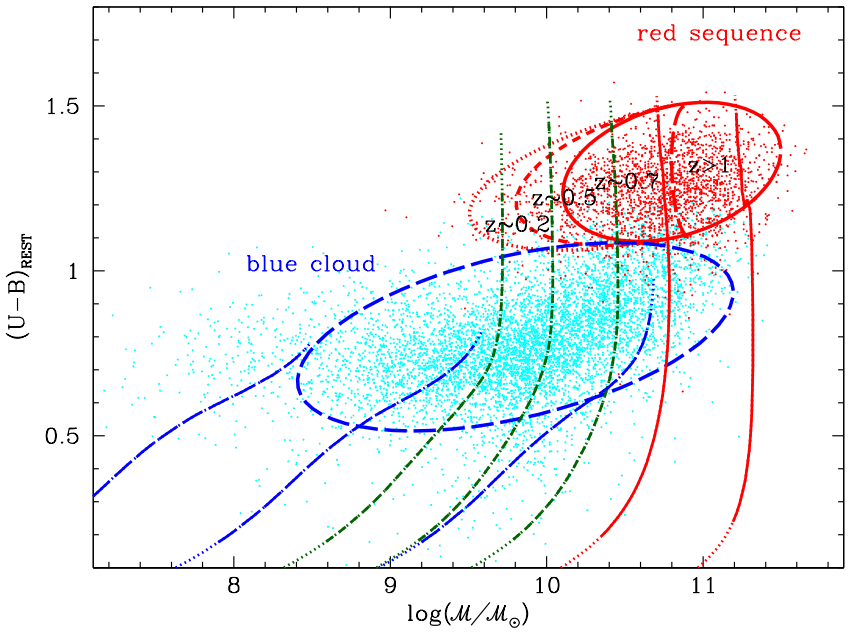

Figure 4.4: Reproduced from Pozzetti et al. (2010). Schematic scenario for galaxy evolution. Different ellipses refer to different redshifts and galaxy populations, while different evolutionary tracks are plotted between 0.1 and 10 Gyr and refer to star formation histories with different timescales and normalized to the total f nal mass.

They also conf rmed that the amount of the evolution for the ETG population depends critically on the range of masses considered, *i.e.* most of the massive ETGs are already in place at $z \sim 1$, while their density is still increasing with time for lower masses. This means that more massive galaxies have older stellar populations and formed their stars earlier and more rapidly than low mass galaxies. This is in agreement with previous works such as Cimatti (2006) or Gallazzi et al. (2006). Therefore, the downsizing pattern (Cowie et al., 1996) could be applied to the assembly process of ellipticals at $z < 1$. The authors suggest a transformation from blue active spiral galaxies of intermediate mass into blue quiescent and successively into red passive types with low specif c star formation. This is in agreement with the result obtained by Faber et al. (2007) who concluded that most present-day E/S0 near L^* arose from blue galaxies with ongoing star-formation that were quenched after $z \sim 1$ and then migrated to the red sequence. The properties of nearby ETGs support a mixed scenario in which quenched galaxies enter the red sequence via wet, gas-rich mergers, followed by a limited number of dry, stellar mergers along the sequence (see Sect. 4.2). In Fig. 4.4 we show an schematic scenario for galaxy evolution as proposed by Pozzetti et al. (2010).

At higher redshifts Arnouts et al. (2007) and Cirasuolo et al. (2007) found a rapid rise in the space density of massive red sequence galaxies from $z \sim 2$ to $z \sim 1$. A recent work by Ilbert et al. (2010) investigated the galaxy stellar mass assembly by morphological and spectral type in the COSMOS field, by deriving the stellar mass functions and stellar mass densities from $z = 2$ to $z = 0.2$ with a sample of $\sim$ 200,000 photometric galaxies.

In Fig. 4.5 we show their derived GSMF divided by spectral type at $0.2 < z < 2.0$. It can be seen that there is a rapid rise of quiescent galaxies at low/intermediate masses. For the quiescent population the stellar mass density of quiescent galaxies of all masses increases by 1.1 dex between $z \sim 1.7$ and $z \sim 1$, while it evolves only by 0.3 dex between $0.8 - 1$ and $z \sim 0.1$. They also found that the GSMF of the "high activity" galaxies shows that the most massive of them end their high activity phase first. Therefore, the low mass star-forming galaxies are able to maintain a high SSFR, while the massive galaxies evolve rapidly into systems with a lower SSFR. This redistribution of the star formation activity follows a clear "downsizing" pattern within the star-forming sample itself.

Similar results are also confirmed by Fontana et al. (2009), who found that the fraction of quiescent galaxies increases from $15 - 20\%$ at $z > 2$ to $\sim$ 40% at $z \sim 1.2$, and recently by Nicol et al. (2011), who found that the red sequence massive galaxies ($M > 10^{11}$ $M_{\odot}$) increase in mass density by a factor $\sim$ 4 from $z \sim 2$ to 1.

Several studies suggest that the critical redshift range where the strongest evolution and assembly took place is $1 \leqslant z \leqslant 2$ (eg., Arnouts et al. 2007, Abraham et al. 2007). However, while the results up to $z \sim 1$ are quite solid thanks to the large samples of galaxies and to the spectroscopic information available, the samples of ETGs studied up to now at $z > 1.4$ are still small. Besides, ETG are the more clustered galaxies in the universe, making their study very complicated given field to field variations which introduce large uncertainties due to the cosmic variance. Anyway, many works have identified these objects spectroscopically, showing that passive/quiescent galaxies with elliptical morphology may exist up to $z \sim 2.5$ (Cimatti et al. 2004, McCarthy et al. 2004, Cimatti et al. 2008). There are even some candidates of ETGs at $z > 4-5$, but their nature is still unknown as they are optically too faint for being spectroscopically observed. Therefore, the uncertainties involved in the study of the evolution of quiescent galaxies at high redshifts are still large due to the observational difficulty to identify large samples of ETGs at high z (> 1.5).

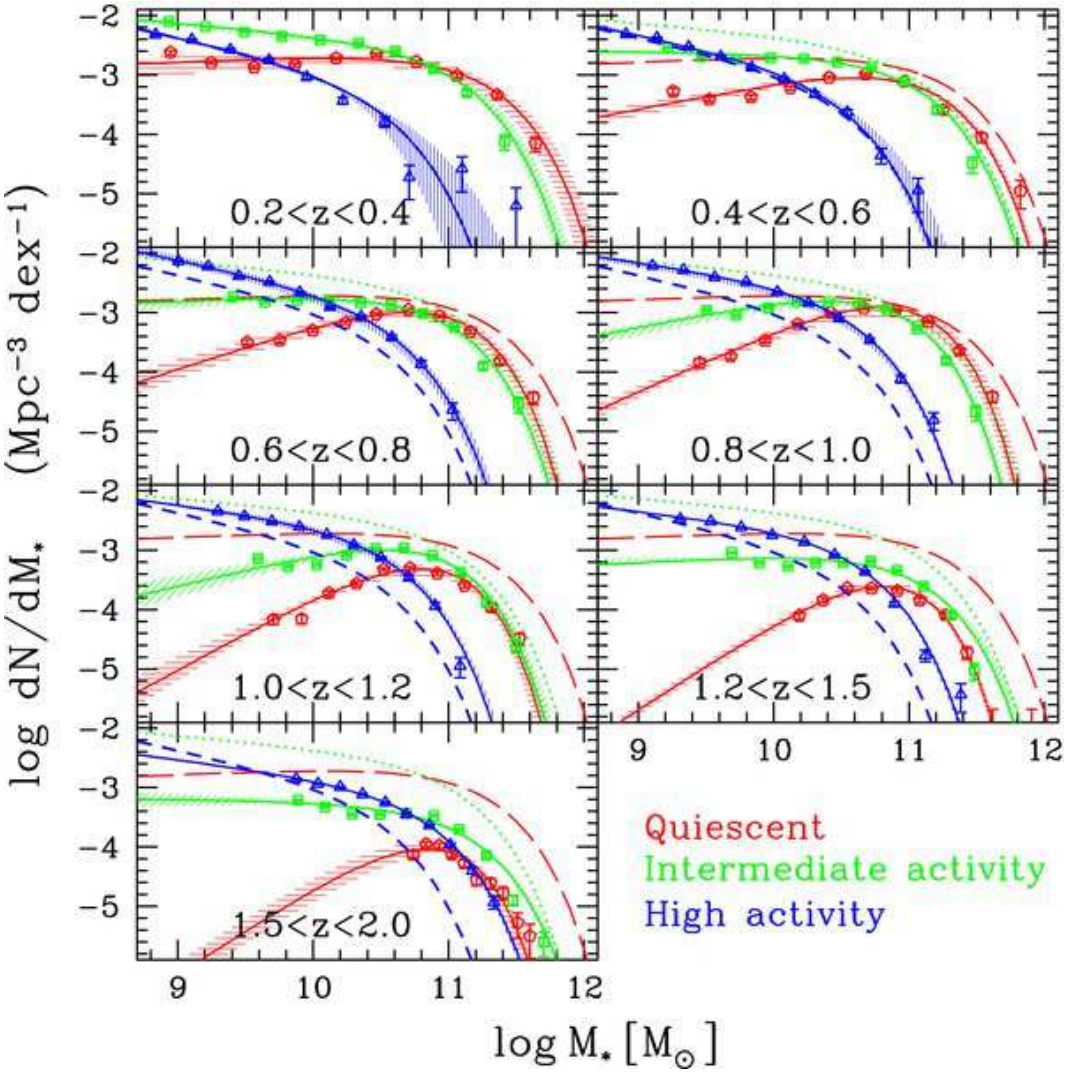

Figure 4.5: Reproduced from Ilbert et al. (2010). GSMF by spectral type. The sample is split into ”high activity” (blue), ”intermediate activity” (green), and ”quiescent” (red) galaxies. The lower and upper limits of the shaded areas are the extreme values of the GSMFs estimated in four quadrants of 0.5 deg^2, which quantifies the impact of cosmic variance. The blue short-dashed lines, the green dotted lines, and the red long-dashed lines are the GSMFs measured at z = 0.2-0.4 for the ”high activity,” ”intermediate activity,” and ”quiescent” galaxies, respectively.

In particular, long wavelength data are necessary to cover the optical-near infrared part of the spectrum of high redshift galaxies, a spectral range fundamental when calculating the galaxy stellar masses. In addition, the collection of a large sample of high redshift galaxies requires a combination of large areas and deep near-IR (NIR) observations. Due to these difficulties, the study of the galaxy stellar mass function (GSMF hereafter) divided by galaxy types at $z > 1.5$ has been explored only roughly and our knowledge of the evolution of galaxies at high z is still rather poor.

Motivated by the limited information available at $z \geq 1.5$, we present in this thesis the evolution of the GSMF with cosmic time at $z \geq 1.4$ for the total galaxy population and for the sample divided on the basis of the galaxy star-forming activity in the COSMOS field. The present work extends to higher redshifts the study of Ilbert et al. (2010). The sample of Ilbert et al. (2010) was selected at 3.6 μm as the present one, but their restriction to IRAC sources with an i^+-band counterpart ($i^+ < 25.5$) limited their study to $z \lesssim 2$ and to larger stellar masses. Our work was possible after a careful analysis of sources not detected in the optical. Studying the evolution of galaxies at such high redshifts is important to put constrains on the theoretical models of galaxy formation and evolution.

CHAPTER 5

Sample Selection and Analysis to Study the Evolution of the Galaxy Stellar Mass Function

In this thesis we have analyzed a sample of ~ 20000 high redshift ($z > 1.4$) sources and studied the different evolution of galaxies with different inferred SSFRs. We built a multiwavelength IRAC selected catalog form the optical to the mid-IR bands and derived accurate photometric redshifts. Then we obtained their important physical parameters through the SED-f tting such us ages, masses and star formation rates. We divided our sample into star-forming, intermediate or quiescent galaxies on the basis of their specif c star formation rates and studied the evolution of the Galaxy Stellar Mass function of the different class of galaxies.

In this chapter we explain the data analysis, from the construction of the catalog with the Likelihood Ratio technique to the derivation of the photometric redshifts. We also explain the SED-f tting procedure to derive the physical parameters of the high redshift sample, as well as our method to classify our galaxies into star-forming, intermediate or quiescent.

5.1 COSMOS f eld

The data analyzed in this thesis come from the *Cosmic Evolution Survey* (COSMOS, Scoville 2007), which is the largest contiguous HST survey ever undertaken,

imagining an equatorial ~ 2 deg ^{2} f eld with single-orbit I-band exposures to a depth $I_{AB} \simeq 28$ mag and 50% completeness at $I_{AB} = 26.0$ mag for sources 0.5 arcsec in diameter. The COSMOS f eld area is large enough to be able to study the coupled evolution of large scale structure, galaxies, active galactic nuclei (AGN) and star formation rate without problems related to cosmic variance that smaller surveys can suffer.

The survey includes multi-wavelength imaging and spectroscopy from X-Ray to radio wavelengths, including HST imaging of the entire f eld. The instruments used for the multi-wavelength coverage are GALEX for the UV (Zamojski et al. 2007), Subaru for the optical (Taniguchi et al. 2007, Capak et al. 2007), CTIO, KPNO and CFHT for the NIR (Capak et al. 2007, McCracken et al. 2010), Spitzer and Herschel for the MIR to FIR bands (Sanders et al. 2007, Lutz et al. 2011), the VLA for the radio data, (Schinnerer et al. 2007), MAMBO for the sub-millimeter (Bertoldi et al. 2007) and XMM and Chandra for the X-Rays (Hasinger et al. 2007, Elvis et al. 2009).

We have also made use of spectroscopic redshifts and data from the zCOSMOS project. The zCOSMOS project (Lilly et al. 2007, Lilly et al. 2009) is a very large VLT/VIMOS (Le Fèvre et al., 2003) spectroscopic program to obtain spectra and redshifts for 37500 galaxies using ~ 600hr observing time. The zCOSMOS survey consists of two parts. zCOSMOS-bright, a pure magnitude-limited selection in the I-band $I_{AB} < 22.5$, is a sample of about 20,000 galaxies. This selection yields redshifts in the range $0.1 < z < 1.2$ covering the whole 1.7 deg^2 COSMOS ACS f eld. A medium resolution grism ($R \approx 600$) was used with a slit width of 1 arcsec, to achieve a velocity accuracy of $\sim 100 km/s$ and enable redshifts to be measured with a high success rate using one hour integrations. The spectral ranges of the observations are typically 5550 – 9650Å to follow the strong spectral features around 4000Å to as high redshifts as possible. The second part, zCOSMOS-deep, is a survey of approximately 10,000 spectra of $B_{AB} < 25.25$ galaxies selected through color-selection criteria to have $1.4 < z < 3.0$, within the central 1deg^2 region of the COSMOS f eld. Measurement of secure redshifts in this redshift range down to $B_{AB} \sim 25$ requires 4–5 hr of integration with the $R \sim 200$ LR-Blue grism, which gives a spectral range from 3600 to 6800 Å. Compared to zCOSMOS-bright, this setup extends the survey through the relatively unexplored 'redshift desert' to $z \sim 3$.

The COSMOS survey is the perfect wide area sample to look for rare and clustered objects such as the old and massive ETGs with much improved statistics. Its

Table 5.1: Effective wavelength, width, systematic offset (s_f) in magnitude of the adopted photometric bands.

Filter	Telescope	Effective λ	FWHM	s_f
u^*	CFHT	3911.0	538.0	-0.054
B_J	Subaru	4439.6	806.7	0.242
g_+	Subaru	4728.3	1162.9	-0.024
V_J	Subaru	5448.9	934.8	0.094
r_+	Subaru	6231.8	1348.8	-0.003
i_+	Subaru	7629.1	1489.4	-0.019
i^*	CFHT	7628.9	1460.0	0.007
z_+	Subaru	9021.6	955.3	0.037
J	UKIRT	12444.1	1558.0	-0.124
K	CFHT	21480.2	3250.0	0.051

multiwavelength and spectroscopic coverage are also fundamental to properly study the SFR properties of the galaxy sample.

5.1.1 Optical and Ultraviolet

The optical catalogue (Capak et al., 2007) is an i^+-band ($i < 26.5$ mag) selected catalog in the area of the Subaru survey (2 deg^2) and includes photometry in 9 bands (u^*, B_J, g^+, V_J, r^+, i^+, z^+, J, K_s). All magnitudes are in the AB system and are aperture magnitudes. The total magnitudes are computed using the aperture corrections tabulated in the multi-wavelength catalog for each source. In addition, for each band a systematic offset, s_f, which is tabulated in Table 5.1, is added to the magnitude.

$$m_{\mathrm{AB,tot}} = m_{\mathrm{AB,aper}} + \text{apert. corr.} + \mathrm{s_f} \tag{5.1}$$

This systematic offset is usually small, of the order of few percent in almost all bands, with the exception of the B_J band (which has known calibration problems) where the offset is about 0.2 with an error of about ±0.05 mag. For a complete description of the observations, data reduction and photometry in the catalog refer to Capak et al. (2007).

5.1.2 Near Infrared

The K_s-selected catalog from McCracken et al. (2010) contains galaxies detected at K_s and additional data from B_J, i^+, z^+ and J bands. The catalog is complete down to $K_s \sim 23.0$ mag.

The following corrections were applied to the catalog, as explained in McCracken et al. (2010):

$$i^+_{\rm tot} = i^+ - 0.1375 \tag{5.2}$$

$$K_{\rm tot} = K' - 0.1568 \tag{5.3}$$

$$B_{\rm tot} = B_J - 0.1093 \tag{5.4}$$

For the z^+, as explained in McCracken et al. (2010), the corrections are more involved. As noted in Capak et al. (2007) the Subaru z-band images were taken over several nights with variable seeing. To mitigate the effects of seeing variation on the stacked image Point Spread Function (PSF), individual exposures were smoothed to the same (worst) full width at half maximum (FWHM) with a Gaussian before image combination. This works well at faint magnitudes, where many exposures were taken, so the non-Gaussian wings of the PSF average out. However, at bright magnitudes ($z^+ \sim 20$) the majority of longer exposures are saturated, so the non-Gaussian wings of the PSF in the few remaining exposures can bias aperture photometry. To correct for this non-linear effect a magnitude dependent aperture correction must be applied in the transition magnitudes between $19 < z < 20$. After f rst applying the correction to total magnitude,

$$z^+{}_{\rm tot} = z^+ - 0.1093 \tag{5.5}$$

we need to apply a further correction:
for $z^+ < 19.0$: $z^+_{\rm tot} = z^+_{\rm tot} - 0.023$,
for $z^+ > 20.0$: $z^+_{\rm tot} = z^+_{\rm tot} + 0.1$
and for $19 < z^+ < 20$: $z^+_{\rm tot} = z^+_{\rm tot} + (z^+_{\rm tot} - 19.0) \times 0.077 + 0.023$.

5.1.3 Mid-Infrared

The COSMOS IRAC catalogue (Sanders et al., 2007) includes Spitzer photometry in the 4 IRAC channels (3.6, 4.5, 5.8, 8.0 μm) for sources that have a measured flux in IRAC Channel 1 above 1 μJy (23.9 mag) in the COSMOS field. IRAC fluxes (computed using an aperture radius of 1.9 arcsec) are in μJy and we converted them to total fluxes dividing it by the wavelength dependent correction factors: 0.765, 0.740, 0.625, 0.580 for 3.6 μm, 4.5 μm, 5.8 μm, and 8.0 μm, respectively. The detections at MIPS 24 μm come from the catalog from Le Floc'h et al. (2009), composed by sources detected above 0.15 mJy (18.5 mag).

Fluxes are converted into magnitudes in the AB system as:

$$m_{\rm AB} = -2.5\log(\mathrm{Flux}[\mu\mathrm{Jy}]) + 23.9 \tag{5.6}$$

5.2 The Multi-wavelength Catalog

To study the evolution of high redshift quiescent galaxies, we built a multi-wavelength IRAC 3.6 μm selected catalog in the COSMOS field by associating the IRAC sources with the optical and 24 μm/MIPS counterparts through the likelihood ratio method (see Sect. 5.2.1). For sources undetected at 5σ in the optical i^+-band selected catalog we have performed a nearest match with the K_s-selected catalog.

We considered sources with $\mathrm{mag}_{3.6\mu m} < 22.0$. The IRAC catalog is 95% complete at 22.0 mag (5.75 μJy). The final catalog consists of 78649 sources with $mag_{3.6\mu m} <$ 22.0: 95% (74742) of them with an optical counterpart, 4.5% (3554) with no optical counterpart but a K_s-band counterpart and 0.5% (353) with only IRAC detection. Besides, 14% (11352) of the IRAC sample is also detected in the MIPS band.

5.2.1 The Likelihood Ratio Technique

For the optical/MIPS identification of the IRAC sources, we used the likelihood ratio technique described by Sutherland & Saunders (1992). Here we recall the most important issues.

For a given optical/MIPS candidate with magnitude m and positional offset r from the IRAC source position, we calculate the probability p that the true source lies in an infinitesimal box $r \pm dr/2$, and in a magnitude interval $m \pm dm/2$, where p is

given by:

$$p = q(m)\, dm \times 2\pi\, r\ f(r)\, dr, \tag{5.7}$$

where *f(r)* is the probability distribution function of the positional errors of the IRAC sources, assumed to be equal in the two coordinates, with

$$2\pi \int_0^{+\infty} f(r)\, r\, dr = 1 \tag{5.8}$$

and *q(m)* is the expected probability distribution, as a function of magnitude, of the true optical/MIPS counterparts.

The likelihood ratio *LR* is def ned as the ratio between the probability that the source is the correct identif cation and the corresponding probability for a background, unrelated object:

$$LR = \frac{q(m) f(r)}{n(m)}, \tag{5.9}$$

where $n(m)$ is the surface density of background objects with magnitude m.

A self-consistent formula has been developed (Sutherland & Saunders, 1992) for the reliability of each individual object, which takes into account the presence or absence of other optical/MIPS candidates for the same IRAC source. The reliability Rel_j for the object j being the correct identif cation is:

$$Rel_j = \frac{(LR)_j}{\Sigma_i (LR)_i + (1 - Q)} \tag{5.10}$$

where the sum is over the set of all candidates for this particular source and Q is the probability that the optical/MIPS counterpart of the source is brighter than the magnitude limit of the optical/MIPS catalog ($Q = \int^{m_{lim}} q(m)\, dm$).

We have f rst counted all objects in the optical/MIPS catalog within a f xed radius around each source (*total(m)*). This distribution has then been background subtracted to construct the distribution function of *real (m)* identif cations:

$$real(m) = [total(m) - n(m) \times N_{IRAC} \times \pi \times radius^2] \tag{5.11}$$

We have then normalized it in order to obtain the expected probability distribution

$$q(m) = \frac{real(m)}{\Sigma_i real(m)_i} \times Q \tag{5.12}$$

where Σ_i is the sum over all the magnitude bins of the distribution, *i.e.* is the total number of objects in the $real(m)$ distribution.

In order to maximize the statistical signif cance of the over density due to the presence of the optical/MIPS counterparts, the radius adopted is the minimum size which assures that most of the possible counterparts are included within such radius.

As probability distribution of positional errors we adopted a Gaussian distribution with standard deviation, σ:

$$f(r) = \frac{1}{2\pi\sigma^2} exp\left(\frac{-r^2}{2\sigma^2}\right) \tag{5.13}$$

Having determined the values of *q(m)*, *f(r)* and *n(m)*, we computed the *LR* value for all the optical/MIPS sources within a distance of 3 arcsec from the IRAC position for each IRAC source. Once that the *LR* values have been computed for all the optical/MIPS candidates, one has to choose the best threshold value for *LR* ($L_{\rm th}$) to discriminate between spurious and real identif cations. The $L_{\rm th}$ value is chosen in order to maximize both the completeness (avoid missing real identif cations) and the reliability (keep spurious identif cations as low as possible) of the associations.

5.2.2 Results

- *IRAC + Optical*

  We considered sources in the optical catalog with f ux in the i^+-band $> 5\sigma$, and eliminated the masked areas and the stars from both catalogs. We performed a match through the likelihood ratio method (Sect. 5.2.1) considering a maximum radius of 3 arcsec (in order to maximize the over-density around the IRAC position) and a dispersion of σ = 1" for the distribution of the positional errors. The distribution of the *background*, the *total* and the *real* counts is shown in Fig. 5.1.

  The majority (96%) of the associations have a separation $\leq$ 1 arcsec, with the median separation being $\sim$ 0.34 arcsec. For a non negligible fraction of the associations with a separation $>$ 1 arcsec, the photometric redshifts we obtained (see Sec. 5.3.3) was not in agreement with the spectroscopic one, meaning a probable spurious IRAC-optical association. Therefore, we have

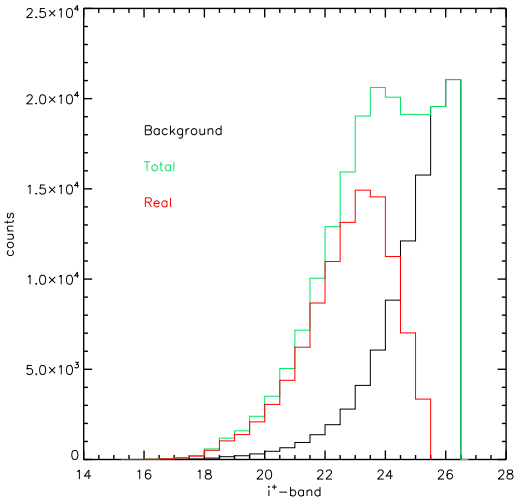

Figure 5.1: Magnitude distribution of the background (black line), total (green line) and real counts (red line) in the i^+-band.

considered as reliable only matches within a separation of 1 arcsec, which is a standard separation used in literature when cross-correlating optical and IRAC catalogs. To reduce contamination from AGNs we have also eliminated the IRAC sources with an optical counterpart associated to an X-ray detection with the XMM-Newton satellite (Cappelluti et al. 2009, 1.5% of the IRAC sample). Finally, we obtained a reliable optical counterpart for 74742 IRAC sources (95%). We will refer to these sources as the 'optical sub-sample' hereafter.

- *IRAC+24 μm*

  We found 11352 IRAC sources (14%) with a reliable MIPS counterpart detected at 5σ. The likelihood ratio method, as described above, has been used.

- *IRAC+K_s*

  For the sources without an optical counterpart we have performed a match with the K_s-selected catalog. In this case, we used the nearest neighbor technique with a maximum separation of 1 arcsec. The similar wavelengths of the K_s and IRAC1 bands allows to perform this match with a low probability of misidentif cation. 90% (3554 sources over 3907) of the IRAC sources with no optical counterpart, have a K_s counterpart ('K_s sub-sample' hereafter). As already mentioned, the K_s-band catalog from McCracken et al. (2010)

Table 5.2: Number of IRAC sources detected in the optical, K_s and MIPS band in our f nal multi-wavelength catalog.

	N (% of the whole sample)	MIPS detection
IRAC sample (all)	78649	11352
Opt. sub-sample	74742 (95%)	10779
K_s sub-sample	3554 (4.5%)	523
IRAC sub-sample	353 (0.5%)	50

contains also information in additional bands (B_J, i^+, z^+ and J). The median magnitude in the i^+-band of these sources is $i^+ \sim 26$, *i.e*. these sources are optically very faint, consistent with them being not in the 'optical sub-sample'.

Finally, we have 353 sources for which we did not f nd neither an i^+-band counterpart, nor a K_s counterpart and for which we have only the IRAC bands information ('IRAC sub-sample' hereafter) and, eventually, the 24 μm (50 sources). The results of the cross-correlation and the f nal numbers of our catalog are summarized in Table 5.2.

5.3 SED f tting: Photometric Redshifts

Due to the huge number of galaxies considered in our sample ($\sim$ 80000 galaxies) we are constrained to study their main properties, (*i.e*., redshift, masses, star formation rates...) on the basis of the SED-f tting technique. We f rst derive accurate photometric redshifts and then we study in more detail the properties of a high redshift sub-sample ($1.4 < z < 3.0$).

5.3.1 The SED-f tting Technique

The SED-f tting procedure to obtain photometric redshifts is one of the most widely used technique. This technique is based on the f t of the overall shape of the photometric data points and on the detection of strong spectral properties. The observed photometric SEDs are compared to those obtained from a set of reference templates, using the same photometric system. The photometric redshift of a given object corresponds to the redshift that better reproduces the shape of the observed data, in general through a standard χ^2 minimization procedure:

$$\chi^2 = \sum_{i=1}^{n_{filters}} \left[\frac{F_{obs,i} - A \times F_{temp,i}}{\sigma_i} \right]^2 \quad (5.14)$$

where $F_{obs,i}$ and σ_i are the monochromatic observed flux and its error in the band i, $F_{temp,i}$ is the monochromatic template flux and A is the normalization constant. This method is widely used in large photometric surveys, where only a few sources have a spectroscopic redshift, and many SED-fitting tools have been recently developed (*e.g.*, *Hyperz*, Bolzonella et al. 2000; *Le Phare*, Arnouts et al. 2001, Ilbert et al. 2006). A crucial test is the comparison between the photometric and the spectroscopic redshifts for the subsample of sources with spectroscopic information (See Sect.5.3.3). The major advantages of the SED fitting technique are its simplicity and the fact that it does not require any spectroscopic sample. The major disadvantage is the dependence of the result with different sets of spectral templates, IMF or extinction curves. The degeneracy of the best-fitting parameters is another important problem, as the shape of an object can be well reproduce both with an extincted template at low redshift or with a bluer template at higher redshift. Analyzing secondary solutions in the χ^2 minimization helps to better understand conflictive galaxies, although this is very time-consuming for large statistical studies.

Template SEDs

As stated before the choice of the set of templates to perform the SED fitting has an important effect in the redshift obtained. There are two main types of spectral templates: observed SEDs (*e.g.* Coleman et al. (1980) (CWW), Polletta et al. 2007) or spectral synthesis models (*e.g.* Bruzual & Charlot 2003, Maraston 2005).

In this work we used the COSMOS SED library provided by Ilbert et al. (2009), which contains a set of templates composed of ellipticals and spirals from the Polletta et al. (2007) library and also includes blue galaxies from the Bruzual & Charlot (2003) population synthesis models. We also added 6 simple stellar population (SSP) models of different ages (0.05, 0.5, 1.0, 1.5, 2.0 and 3.0 Gyr) from Maraston (2005) to account for passively evolving galaxies at high redshifts. The final library is composed of 7 ellipticals, 12 spirals, 12 starbursts and 6 SSP templates. Some representative templates of the library are shown in Fig. 5.2. We chose this set of templates as it is the one that maximizes the accuracy of the derived

photometric redshifts (z_p) when compared with the available spectroscopic redshifts (z_s) (see Section 5.3.3).

5.3.2 Method

As already mentioned, the only eff cient way to estimate the redshifts of the galaxies for the whole sample, given the large number of sources considered, is to determine their photometric redshifts through a detailed SED-f tting procedure.

Photometric redshifts were derived using the *Le Phare* code (Arnouts et al. 2001, Ilbert et al. 2006), which computes photometric redshifts based on a simple χ^2 template-f tting procedure. We used the COSMOS SED library provided by Ilbert et al. (2009), explained in Sect. 5.3.1. We f tted our data from the U to the 24μm band and we allowed 3 different extinction laws (Calzetti et al. 2000, Calzetti modif ed and Prevot et al. 1984) to be applied to each template. We used 9 different values of $E(B-V)$: 0, 0.05, 0.1, 0.15, 0.2, 0.25, 0.3, 0.4 and 0.5.

We set an upper limit (5σ) to each band when there is no detection, as shown in Table 5.3. This 5σ limit was chosen following a conservative approach, *i.e.* as the brightest magnitude value of the sources in the catalog detected with $S/N = 5$ (magnitude error = 0.2) for each band. The choice of this limit is plotted in Fig. 5.3 for the B-band.

The χ^2 minimization procedure is highly affected by the adopted photometric errors (see Ilbert et al. 2009 for a detailed discussion of the issue). We increased the f ux error by 6, 5 and 8% for the optical, IRAC and MIPS bands respectively.

5.3.3 Photometric Redshift Accuracy

We were able to test the quality of our derived photometric redshifts for the IRAC sources with i^+-band detection by comparing them with a large sample of spectroscopic redshifts. In particular, we made use of 8176 sources with derived spectroscopic redshift at a very high conf dence level (99.8%, f ags 3.1, 3.5, 4.1, 4.5) from the zCOSMOS faint and bright surveys (Lilly et al. 2007, 2009). We estimated the redshift accuracy as $\sigma_{\Delta z/(1+z_s)}$ (where $\Delta z = zp - zs$ is the difference between the photometric and the spectroscopic redshifts) using the normalized median absolute deviation def ned as $1.48\langle|z_p - z_s|/(1+z_s)\rangle$. We also def ned the percentage of catastrophic errors, η, as the objects with $|z_p - z_s|/(1+z_s) > 0.15$. We obtained an

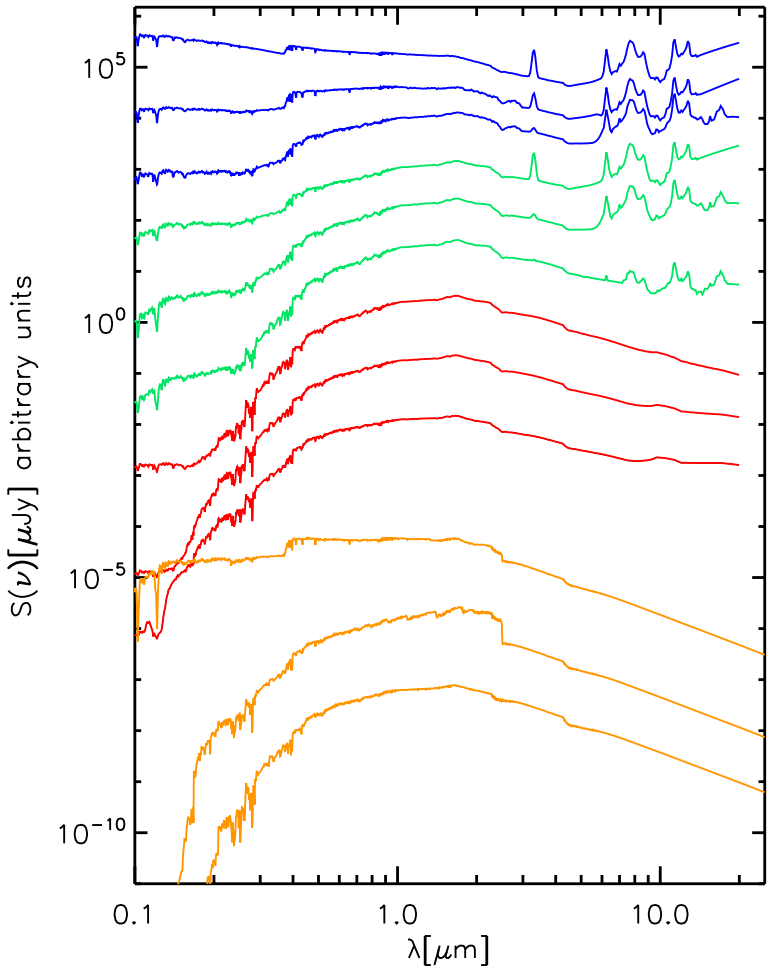

Figure 5.2: Representative templates of the SED library used. Orange: simple stellar population models of 0.05, 1.0 and 3.0 Gyr (Maraston, 2005). Red: elliptical (Polletta et al., 2007). Green: spirals (Polletta et al., 2007). Blue: blue galaxies (Bruzual & Charlot, 2003).

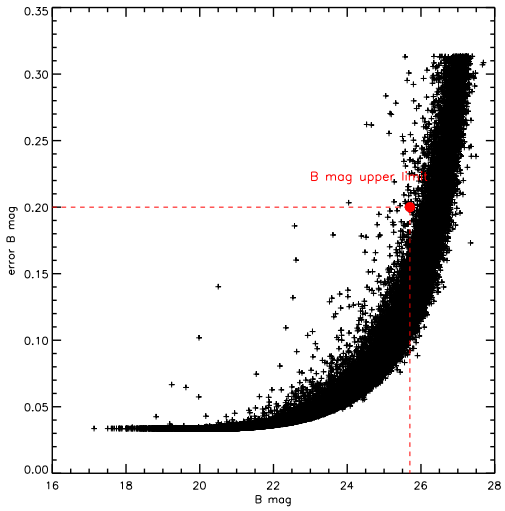

Figure 5.3: Magnitude error vs magnitude for the sources of our sample in the B-band. The red point is the 5σ limit, chosen as the brightest magnitude value of the sources in the catalog detected with S/N=5 (mag error = 0.2).

accuracy of $\sigma_{\Delta z/(1+z_s)} = 0.06$ and a percentage of catastrophic failures of $\eta = 3.3\%$ as can be seen in Fig. 5.4. As a comparison, Ilbert et al. (2009) using the bright ($i^+ < 22.5$ mag) sample with 30 bands and narrow f lters obtained $\sigma = 0.007$ and $< 1\%$ of catastrophic errors for their derived photometric redshifts, while the average value of σ obtained by Pérez-González et al. (2008) using an IRAC selected catalog with data from the UV to the MIR is 0.055. Given the fact that we use 14 broad bands, we f nd our result comparable to those in literature.

We also tested the reliability of our z_p for the faintest sources, with $mag_{3.6\mu m} > 21.0$ and $i^+ > 22.5$, as shown in Figs. 5.5 and 5.6 respectively. The value of σ for the faint i^+-band sources ($\sigma = 0.057$) is comparable to the value of σ for the whole sample, while the number of catastrophic errors increases ($\eta = 12\%$). For the faint IRAC1 sample both σ and η are smaller than for the whole sample ($\sigma = 0.037$, $\eta = 1.9\%$). This may surprise the reader, but it must be noticed that the values for the whole spectroscopic sample are highly affected by a signif cant dispersion on low redshift sources ($z_s \sim 0.3 - 0.5$, see Fig. 5.4), which are present in a smaller fraction in the faint IRAC sample.

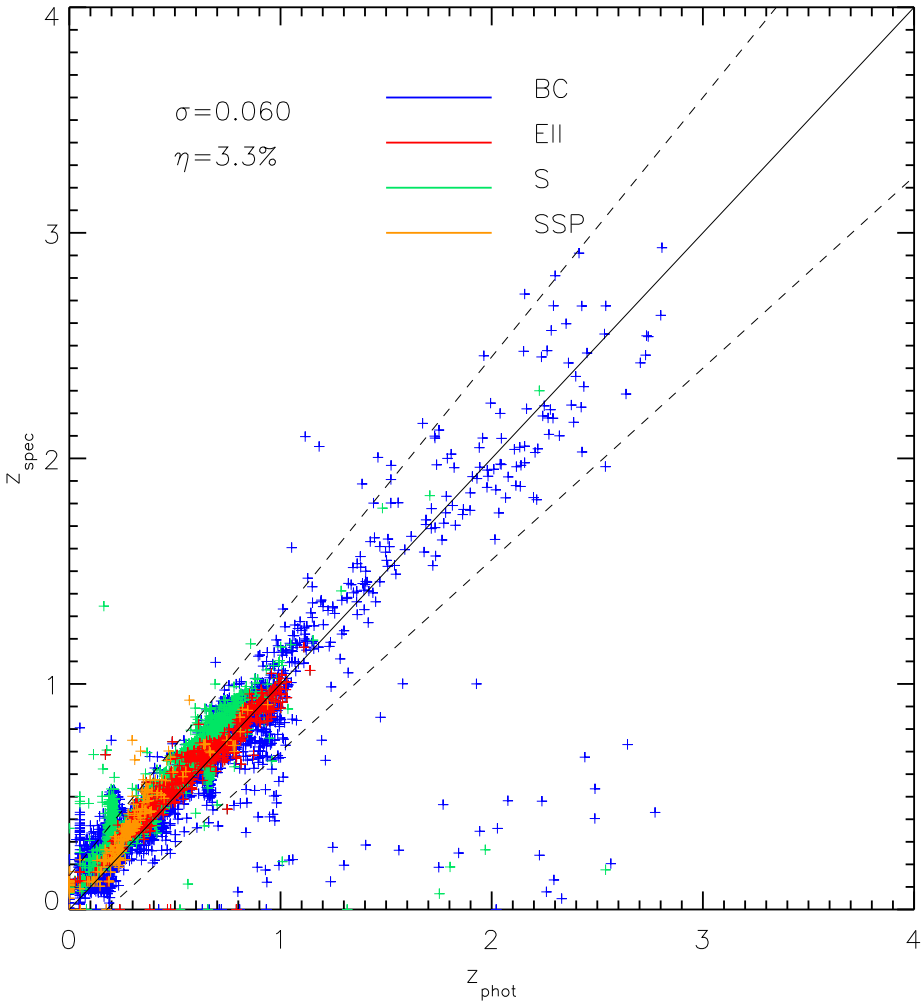

Figure 5.4: Comparison between z_p and z_s for the 8176 sources with optical and IRAC detection of the zCOSMOS sample. The value of σ and η are shown in the plot. The different colors represent sources f tted by different SED templates as explained in Fig. 5.2. Dashed lines represent $|z_p - z_s|/(1+z_s) = 0.15$, *i.e.* sources out of that region are considered as catastrophic errors.

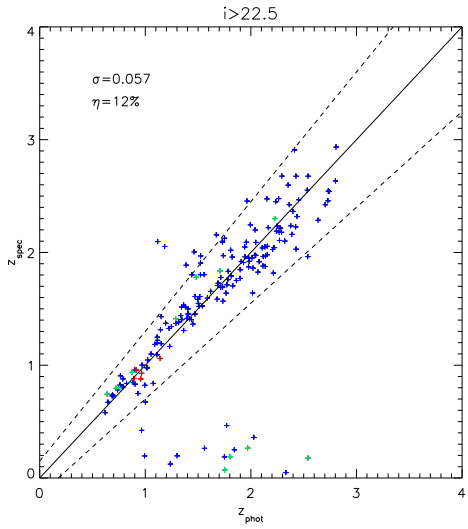

Figure 5.5: Comparison between z_p and z_s for 183 sources with i^+-band > 22.5. Colors and dashed lines as in Fig. 5.4.

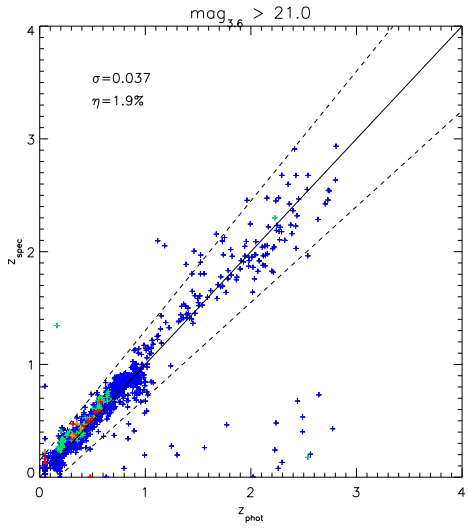

Figure 5.6: Comparison between z_p and z_s for 2381 sources with $mag_{3.6\mu m}$ > 21.0. Colors and dashed lines as in Fig. 5.4.

Table 5.3: 5σ limit adopted for each band.

band	optical sub-sample	K_s sub-sample
u^*	25.3	-
b_J	25.7	27.0
g^+	25.5	-
V_J	25.5	-
r^+	25.6	-
i^+	25.1	26.2
z^+	24.5	25.0
J	22.0	22.0
K	22.0	-
*IRAC*1	-	-
*IRAC*2	23.3	-
*IRAC*3	21.2	-
*IRAC*4	21.0	-
MIPS	18.5	-

Photometric Redshift Accuracy for the IRAC Sources with no I Band Counterparts

For the sources with no i^+-band counterpart it is not possible to directly compare the photometric redshifts with spectroscopic redshifts, since no z_s are available for these sources. To test the quality of the derived photometric redshifts we have made use of the 1σ dispersion of the z_p distribution for each galaxy, given as an output of the *Le Phare* code. The 1σ uncertainty of the z_p is estimated as half the difference between $z_{p,sup}$ and $z_{p,inf}$, where $z_{p,sup}$ and $z_{p,inf}$ are the z_p value for $\Delta\chi^2 = 1$ in the redshift probability distribution.

The mean error on the z_p for the whole sample is $\sigma_z = 0.17$, which corresponds to $\sigma_{\Delta z/(1+z_s)} \sim 0.057$ at $z \sim 2$, meaning that the 1σ dispersion of the z_p distribution is consistent with the $\sigma_{\Delta z/(1+z_s)}$ derived from the z_p and z_s comparison. The redshift uncertainties derived from *Le Phare* have been used in the Montecarlo simulations (see Section 6.1.3) to derive the Galaxy Stellar Mass Function uncertainties.

In Figs. 5.7, 5.8 and 5.9 we show some examples of SED fitting for sources fitted by different templates (elliptical (Ell), simple stellar populations (SSP), spirals (S) and blue galaxies or starbursts (SB)) for sources from the optical, K_s and IRAC sub-samples.

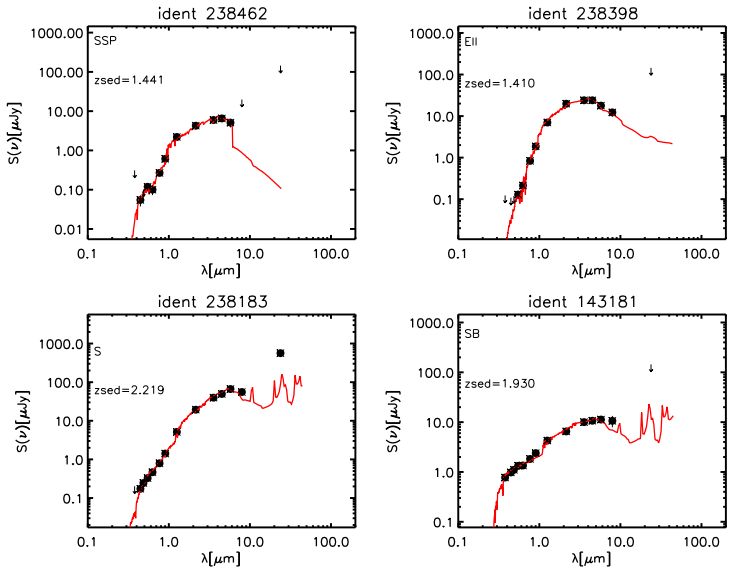

Figure 5.7: Example of SED-f tting for 4 sources from the optical sub-sample. The observed SED of each source (black f lled circles) is shown with the corresponding best-f t solution (red solid line), as well as the derived z_p and best template model. Arrows represent upper limits (5σ) when no detection is found in that band.

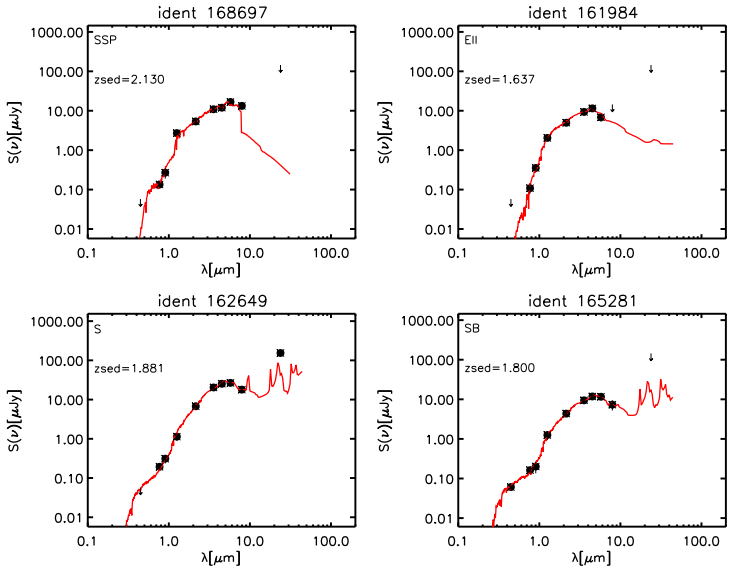

Figure 5.8: Example of SED-f tting for 4 sources from the K_s sub-sample, *i.e.* sources not present in the i^+-band catalogue (Ilbert et al. 2010) but with a K_s counterpart (McCracken et al. 2010).

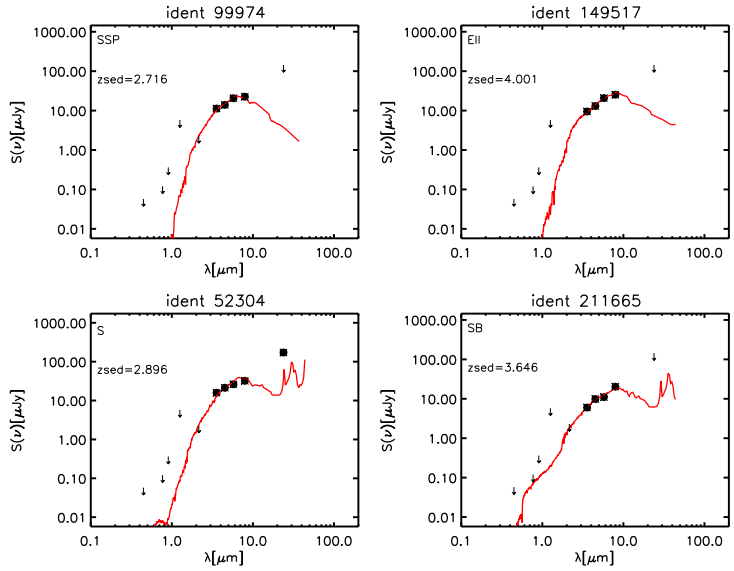

Figure 5.9: Example of SED-fitting for 4 sources from the IRAC sub-sample, *i.e.* sources only detected in the IRAC bands.

5.3.4 Redshift Distribution

Fig. 5.10 shows the redshift distribution for each sub-sample, highlighting the contribution from different classes of best-fitting templates. Templates have been divided in 3 classes: elliptical/old SSP (older than 1 Gyr), blue/young SSP (younger than 1 Gyr) and spirals. It can be observed that these redshift distributions are not smooth, but show some peaks at given redshifts, e.g., at $z \sim 1.0$, 2.0 for the K_s sub-sample or a very prominent peak at z ~ 4.0 for the IRAC sub-sample. However, the peak at $z \sim 4$ in the IRAC sub-sample is not used since we limit our analysis to $z < 3.0$. It is also interesting to notice the small number of sources involved in this peak (< 0.2% of the sample). This kind of features in the redshift distribution are presumably not real, but due to the determination of the redshifts through a SED fitting procedure. Spiky redshift distributions have also been reported in literature, by Pérez-González et al. (2008) and Franx et al. (2008) among others. The number of sources in each subsample with a reliable z_p is shown in Table 5.4, as well as the number of sources for each sub-sample fitted with each class of template. The number of high redshift ($z \gtrsim 1.4$ and $z \gtrsim 2.5$) sources for each sub-sample is also shown.

It is clear how differently the three sub-samples behave, with 88% and 91% of the K_s and the IRAC sub-samples respectively found at high redshift ($z \geq 1.4$),

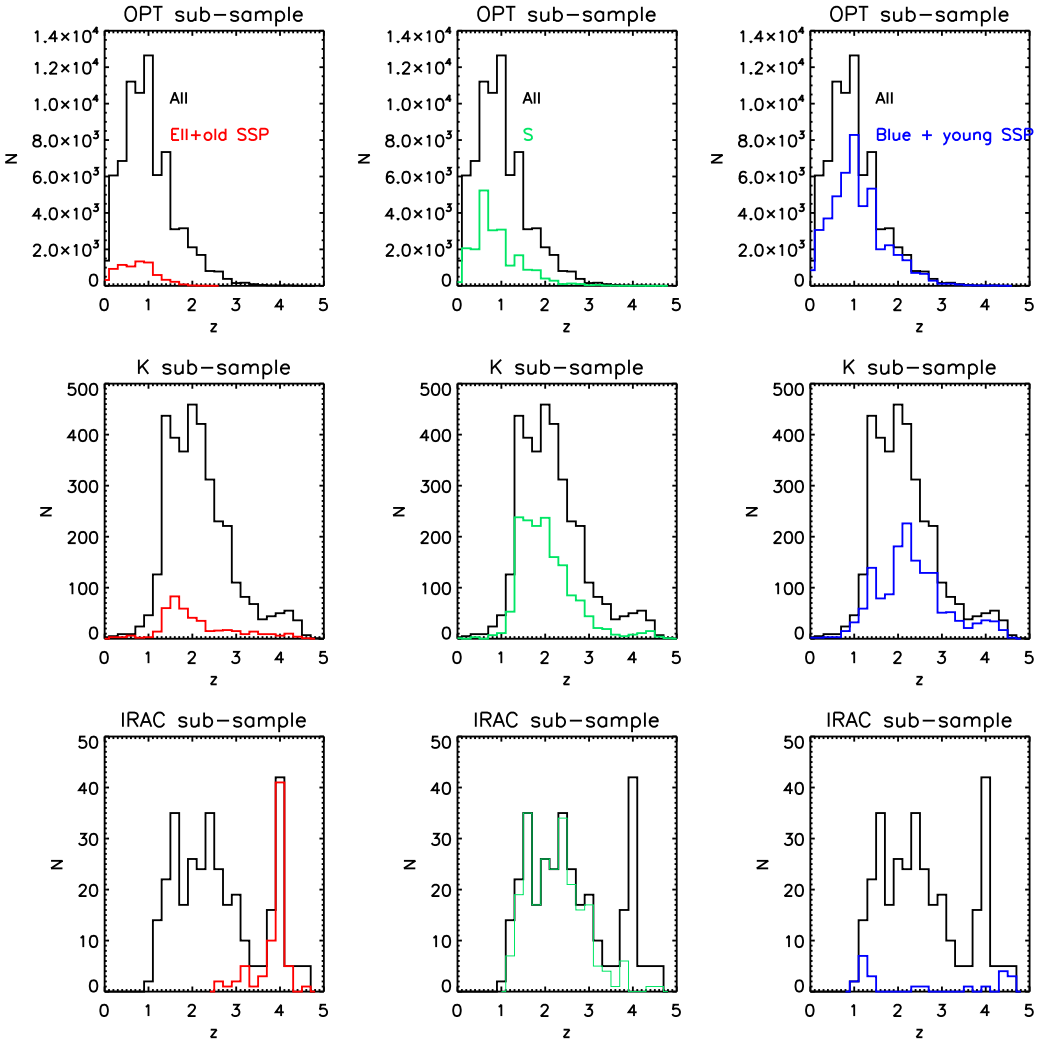

Figure 5.10: Redshift distribution for the different sub-samples. In the 3 upper panels we show the redshift distribution of the optical sub-sample (black line), as well as the redshift distribution of the sources f tted by an elliptical/old SSP template (red line), a spiral template (green line) or a blue/young SSP template (blue line). The same is plotted for the K_s and the IRAC sub-samples in the middle and bottom panels, respectively.

Table 5.4: Percentages of best fit templates and high redshift sources ($z \geq 1.4$ and $z \geq 2.5$) for the different sub-samples.

	Opt. sub-sample	K_s sub-sample	IRAC sub-sample
All	74742	3554	353
Ell/old SSP	10%	12%	22%
S	28%	45%	71%
Blue/young SSP	62%	43%	7%
$z \geq 1.4$	21%	88%	91%
$z \geq 2.5$	2.3%	27%	47%

in comparison to 21% of the optical sub-sample. For very high redshift sources ($z \gtrsim 2.5$) the differences are even more significant, since only 2.3 % of the optical sub-sample is found at those redshifts, while this percentage is 27% and 47% for the K_s and IRAC sub-samples, respectively. Also the relative fractions of best-fitting templates are very different. On the one hand, 10% of the optical sub-sample is fitted by an elliptical/old SSP model, while for the IRAC sub-sample the fraction is double (22%). On the other hand, only 7% of the IRAC sub-sample is fitted by a blue/young SSP model, while these templates represent 62% of the solutions for the optical sub-sample. These percentages are indicative of the importance of an IRAC selected sample to study the properties of high redshift galaxies whose SED is reproduced by quiescent populations.

5.4 SED-fitting: Galaxy Stellar Masses and Star Formation Rates

5.4.1 Stellar Population Synthesis Models

As already explained in Chapter 2 stellar population synthesis models are tools for interpreting the integrated light (colors, line indices, and mass-to-light ratios) from the observed galaxies. Specifically, the purpose is to determine what mix of stars give rise to the observations using the knowledge of stellar evolution. The stellar population synthesis models are used to determine ages, element abundances, stellar masses, star formation rates, etc., of those stellar populations that are not resolvable in single stars, like galaxies and extra-galactic globular clusters. The

simplest models used are the Single Simple Stellar Populations SSP. In these, all the stars are formed at the same time, with distribution in mass given by the chosen IMF, and with identical chemical composition. SSPs can be compared directly with globular cluster (GC) data, since these are the simplest stellar populations in nature, allowing us to calibrate the SSPs with those GCs for which ages and element abundances are independently known (Renzini & Fusi Pecci, 1988). More complex stellar systems which are made up by various stellar generations are modeled by convolving SSPs with the adopted star formation history (SFH) (*e.g.*Tinsley 1972, Barbaro & Poggianti 1997, Bruzual & Charlot 2003). More advanced models take evolutionary processes into account, *i.e*. enrichment of the interstellar medium, differential loss of various element by galactic winds, time-dependent IMF, etc.

Using a similar procedure to that used for determining the photometric redshift, the main fundamental parameters of galaxies are obtained by f tting the observed data to a set of stellar populations synthesis models f xing the redshift z of the galaxy to the value derived through the photometric redshift f tting procedure (see Sect. 5.3). The adopted models are generated with well-known properties (ages, metallicities, etc) so the resulting best-f tting SED contains all the important information about the stellar population of that particular galaxy.

5.4.2 Maraston 2005 Models

We derived the stellar masses of the galaxy sample making use of the stellar population synthesis models from Maraston (2005), which adopt the fuel consumption theorem.

There are two different techniques adopted to compute SSP models: 'isochrone synthesis' and 'fuel consumption based' algorithms, which differ according to the integration variable adopted in the post-Main Sequence phase.

For the 'isochrone synthesis' (*e.g.*Chiosi et al. 1988, Charlot & Bruzual 1991) the integrated variable is the contribution to the f ux in the various pass-bands of all mass-bins along one isochrone, after assuming an IMF. However, the isochrones are usually computed up to the end of the Early Asymptotic Giant Branch phase (EAGB) while later stellar phases (like the Thermally-Pulsing Asymptotic Giant Branch, TP-AGB) are often neglected or added following individual recipes.

Instead, in the 'fuel consumption' approach (Renzini & Voli 1981, Buzzoni 1989,

Maraston 1998) the integration variable in Post Main Sequence phase is the so-called *fuel*, *i.e*. the amount of hydrogen and/or helium that is consumed via nuclear burning during a given post Main Sequence phase. Two main advantages are obtained when using this approach. First, the fuel is a very stable integration parameter and it is directly proportional to the contribution to the total luminosity of the various phases. This is fundamental in luminous but very brief evolutionary stages, such us the red giant branch (RGB). Second, it does not introduce the uncertainties related to the theoretical modeling of several relevant stellar phases, for which complete stellar tracks are not available due to mass losses (*e.g*.blue horizontal branch (BHB), TP-AGB, etc). The fuel consumption provides useful analytical relations that link the Main Sequence to the post Main Sequence evolution, by means of which one can include into the synthesis the energy contributions of these uncertain phases. The 'isochrone synthesis' technique is the most commonly used in the literature, while the models by Buzzoni (1989) and Maraston (1998, 2005) adopt the fuel consumption theorem.

5.4.3 Method

To study the evolution of the galaxy stellar mass function of sources at high redshift we have selected the sources with $1.4 < z < 3.0$. When available, we have made use of z_s (654 sources, $\sim$ 3.4% of the sample), while for the galaxies without spectral information we adopted the photometric redshift value z_p obtained through the SED-f tting procedure.

The galaxy stellar masses and other important physical parameters (such as SFRs, ages, extinctions, etc) have been derived by means of the *Lephare* code by f tting our data (up to 5.8μm) with a set of SED models from Maraston (2005) with star formation histories exponentially declining with time as $SFR \propto e^{-t/\tau}$, with τ being the duration of the burst. We used 9 different values of τ (0.1, 0.3, 1.0, 2.0, 3.0, 5.0, 10.0, 15.0 and 30.0 Gyr) and 221 steps in age. The assumed metallicity is solar and the IMF is from Chabrier (2003). Dust extinction was applied using the Calzetti et al. (2000) extinction law, with a maximum E(B-V) value of 0.5. We imposed to the derived age of the galaxies to be less than the age of the Universe at the galaxy redshift and greater than 10^8 years (the latter requirement avoids having galaxies with extremely high specif c star formation rates).

We decided to use the Maraston (2005) models as they include a better treatment

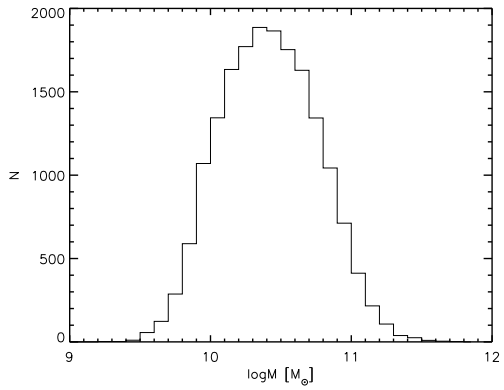

Figure 5.11: Distribution of the stellar masses obtained for our high redshift sample of galaxies using the Maraston (2005) models.

of the thermally pulsing asymptotic giant branch (TP-AGB) phase, which has a high impact on modeling the SED templates at ages in the range $0.3 \lesssim t \lesssim 2$ Gyr, where the fuel consumption in this phase is maximum, specially for the near-IR part. Although some authors (Kriek et al., 2010) have recently claimed that the Maraston (2005) models do not properly reproduce the observed data in a sample of post-starburst galaxies, *i.e*. at the time when TP-AGB stars are thought to be most dominant, we have instead found good f ts for our SEDs. Pozzetti et al. (2010) measured an average systematic shift of 0.14 dex between the stellar masses computed with the Bruzual & Charlot (2003) models and the Maraston (2005). We have taken this difference into account when comparing our results with those obtained with the Bruzual & Charlot (2003) models.

In Fig. 5.11 we show the distribution of the logarithm of the stellar masses that we obtain when performing a SED-f tting to our high redshift ($1.4 \leq z \leq 3.0$) sample using the Maraston (2005) models.

5.4.4 Stellar Masses Uncertainties

Stellar masses values depend on a number of different assumptions in the SED-f tting procedure, like, for example, the IMF, the extinction laws, the metallicity, the star formation histories or the choice of the SED template libraries. Tests on simulated catalogs considering the effect on stellar mass estimates of different choices of reddening law, SFHs, metallicities and SED libraries show a typical dispersion of the order of $\sigma(logM) \sim 0.20$ (see Bolzonella et al. 2009), showing

that the stellar mass is a rather stable parameter in the SED-fitting procedure.

As for the z_p, we estimated the 1σ stellar mass uncertainty for each galaxy as half the difference between M_{sup} and M_{inf}, where M_{sup} and M_{inf} are the mass values obtained for $\Delta\chi^2 = 1$ in the probability mass distribution. The mean error on the stellar mass, as estimated from the 1σ dispersion of the mass distribution for each source (given as an output of the *Le Phare* code), is 0.16 dex, consistent with the uncertainties mentioned above.

5.5 Galaxy Classification

5.5.1 Method

Galaxies with different stellar populations have different properties and evolve in very different ways. In this work we aim to classify galaxies on the basis of their specific star formation activity, *i.e.* the number of stars formed at a given time per unit mass and to study the characteristic evolution of the quiescent and star-forming galaxies. We considered 3 different populations on the basis of the ratio between the SFR and the mass of each galaxy, derived through the SED-fitting procedure:

1. Actively star-forming galaxies: those for which $log(SSFR[\mathrm{Gyr}^{-1}]) > -0.5$
2. Intermediate galaxies: those for which $-2 < log(SSFR[\mathrm{Gyr}^{-1}]) < -0.5$.
3. Quiescent galaxies: those for which $log(SSFR[\mathrm{Gyr}^{-1}]) < -2$.

   We found 84 sources ($\sim$ 0.5 % of the high-z sample) with $log(SSFR[\mathrm{Gyr}^{-1}]) < -2$ and detected in the 24 μm band. As the emission at 24 μm usually arises from dust heated by star-formation activity, we included these sources in the intermediate population.

The limits on the SSFR values have been defined from the distribution of the SSFR values (Fig. 5.12 for the optical sub-sample) and we have verified that they are consistent with the best-fitting template classification obtained when deriving the photometric redshifts, *i.e.* using the COSMOS SED templates. Most of the sources with very low SSFR are fitted by an elliptical or old SSP template, while those with the highest activity are generally fitted by a young SSP or a blue template, as should be expected on the basis of their colors. Considering the whole sample, we have

z	all	quiescent	intermediate	star-forming	MIPS
1.4-1.6	5142	515	1325	3302	261
1.6-2.0	6303	512	1445	4346	1286
2.0-2.5	4693	287	914	3492	1178
2.5-3.0	1794	77	415	1302	272

Table 5.5: Number of galaxies with $1.4 \leq z \leq 3.0$ in different redshift bins and classif ed according to the SSFR value.

carefully studied the cases where star-forming sources are f tted by an elliptical or old SSP template, as well as quiescent sources f tted by a blue or a young SSP template. We found only 26 sources ($\lesssim 0.1\%$ of the high redshift sample) f tted by an elliptical or old SSP template with high star-forming activity. On the other hand, more than 94% of the 639 sources (3.5% of the high redshift sample) f tted by a blue template with low SSFR are not detected in the U-band, which is a critical band to determine the star formation activity of a galaxy.

We have derived mean SSFR errors making use of the 1σ dispersion of the SSFR distribution for the whole sample, obtaining a mean SSFR error of 0.38 dex for the whole sample. In Table 5.5 we report the number of galaxies classif ed as star-forming, intermediate and quiescent, as well as the MIPS detected sources, in each redshift bin for sources with $1.4 \leq z \leq 3.0$.

5.5.2 Comparison with BzK

The *BzK* criterion was f rst introduced by Daddi et al. (2004) and it was calibrated using the complete spectroscopic redshift database of the K20 survey (Cimatti et al., 2002). The *BzK* criterion eff ciently separates the star-forming and the passively evolving galaxies at $z \gtrsim 1.4$ based on a simple color-color criterion. Star-forming galaxies at $1.4 \leq z \leq 2.5$ are supposed to occupy the region def ned by the following colors:

$$BzK \equiv (z - K) - (B - z) \geq -0.2, \tag{5.15}$$

Instead, the passively evolving galaxies lie in the region def ned by:

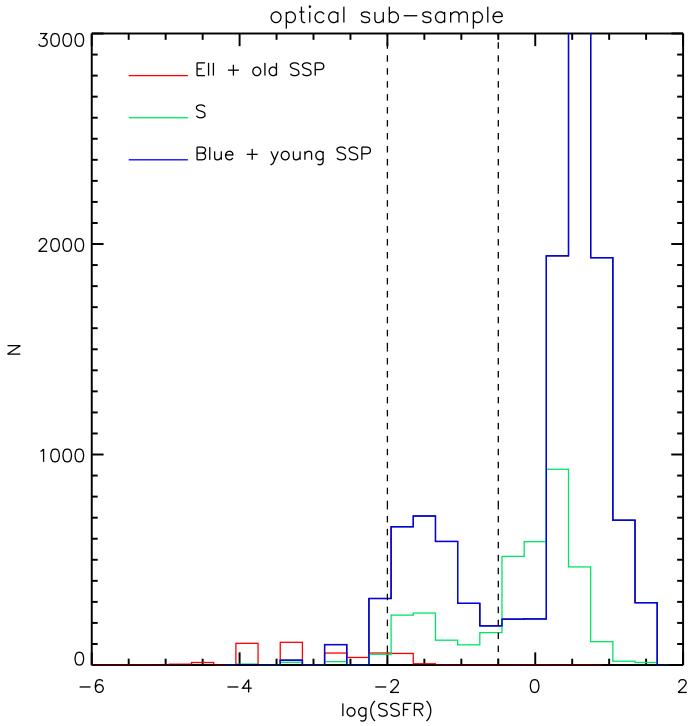

Figure 5.12: SSFR distribution for the optical sub-sample of sources with $z \geq 1.4$. The colors represent the different classes derived from the SED f tting templates. Dashed vertical lines represent the limits considered in SSFR to divide sources as actively star-forming, intermediate or quiescent.

$$BzK \equiv (z - K) - (B - z) < -0.2 \cap z - K > 2.5 \quad (5.16)$$

To further test our classif cation method, we plotted our galaxies in the *BzK* diagram (Fig. 5.13), where the star-forming galaxies are represented in blue, the intermediate in green and the quiescent in red. Fig. 5.13 shows that galaxies for which low activity is derived roughly occupy the passive region in the *BzK* diagram, while for the star-forming galaxies, their colors are consistent with the *BzK* star-forming selection. Only 3 sources def ned as star-forming fall in the passive region of the *BzK* diagram.

5.5.3 High Redshift Quiescent Galaxies

In this Section we summarize the properties of the high redshift quiescent galaxies (also known as ETGs in literature) by analyzing the physical parameters obtained through the SED-f tting procedure.

We found 1391 quiescent galaxies at $z \leq 1.4 < 3.0$. They are old and massive galaxies ($\langle M \rangle \sim 10^{10.65} M_{\odot}$): more than 56% of them have $M \geq 10^{10.6} M_{\odot}$ and $\sim$ 12% have $M \geq 10^{11.0} M_{\odot}$. They have weakly star-forming stellar populations, with ages ranging from 1 to 4.25 Gyr. Some of them are so old to reach the limit allowed by the age of the Universe at their redshift, meaning very high formation redshifts. They have *e-folding* time scales $\tau \sim 0.1 - 0.3$ Gyr, *i.e.* they should have formed in a very intense and brief starburst. They are characterized by very low dust extinction (E(B-V) $\sim 0 - 0.15$), implying that their red optical colors are due to evolved stellar populations and not to dust extinction. These characteristics are in agreement with previous results (e.g., Cimatti 2009, Kriek et al. 2008).

In Fig. 5.14 we show the SED and report the main physical parameters of 6 different high redshift quiescent galaxies. We show examples from the optical, K_s and IRAC sub-samples. We underline the importance of the upper limits in the optical and K_s bands for the IRAC sub-sample to constrain the SED model.

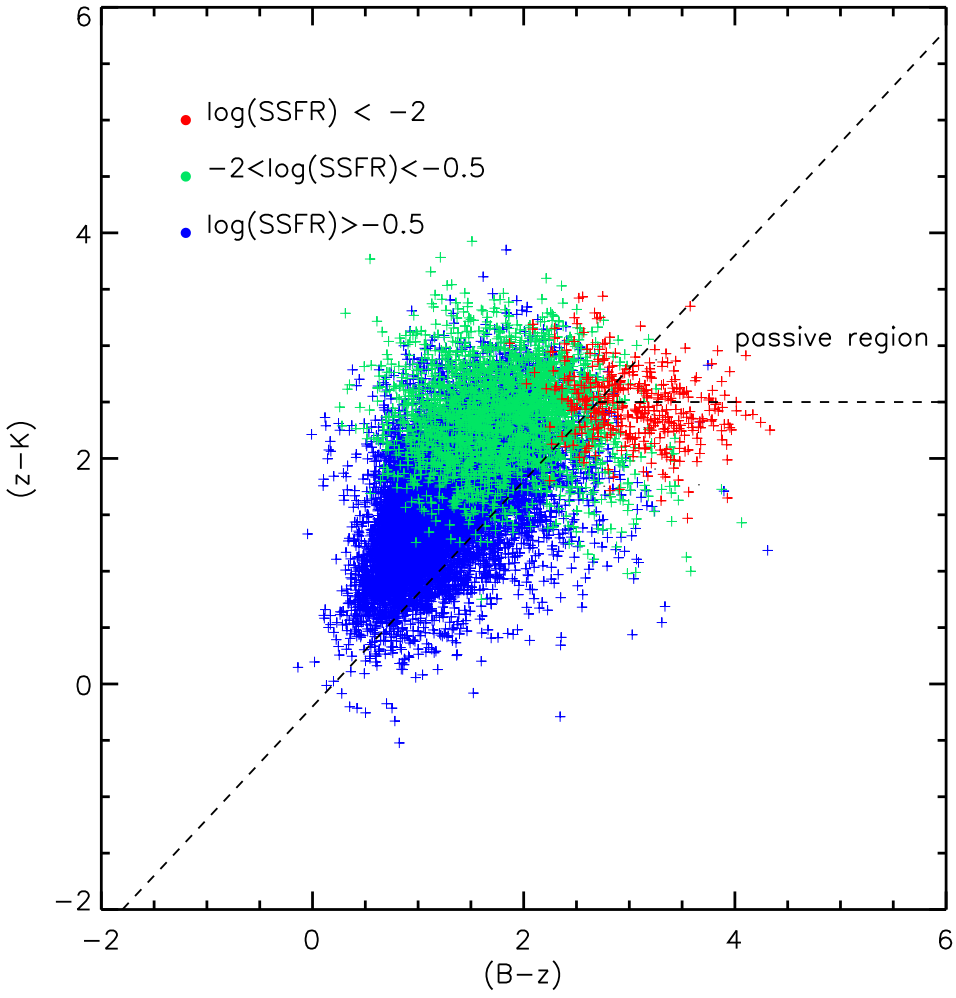

Figure 5.13: *BzK* diagram (Daddi et al., 2004) for optically detected sources with $1.4 \leq z \leq 2.5$ (the dashed lines show the different regions of the *BzK* diagram). The colors represent the different galaxy classes derived from the SSFR criteria used in this work (red: quiescent, green: intermediate, blue: star-forming).

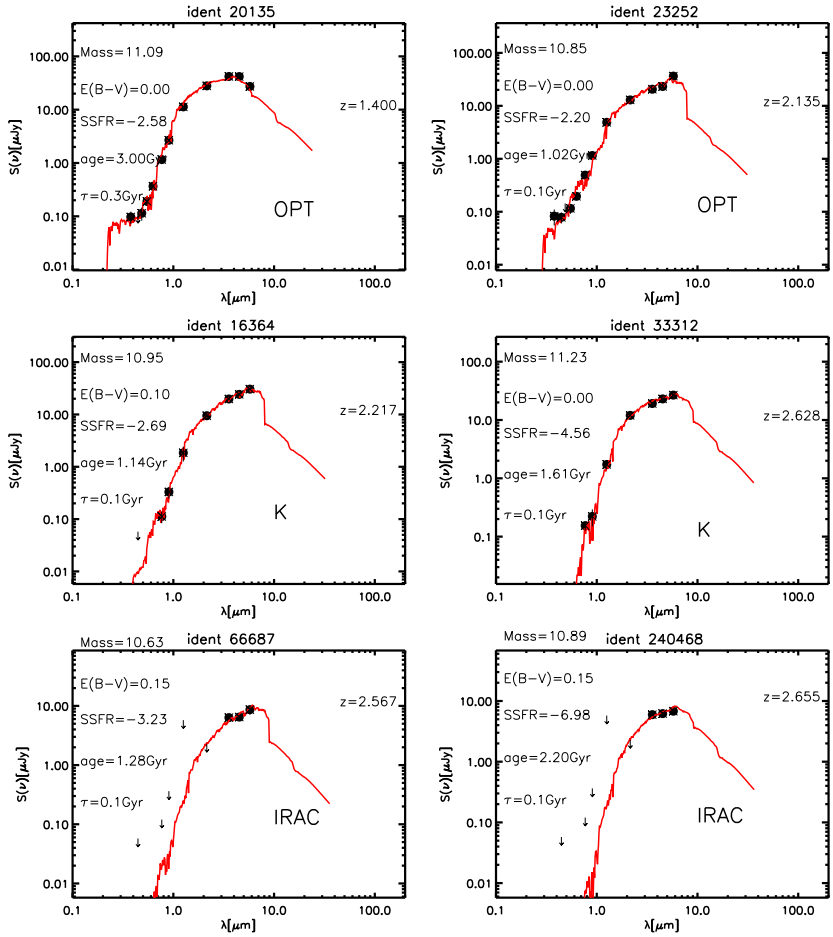

Figure 5.14: SED-f tting of some high redshift quiescent galaxies. The observed SED of each source (black f lled circles) is shown with the corresponding best-f tting model (red solid line) from the Maraston (2005) library. The main physical parameters derived through the SED-f tting process (mass, extinction, SSFR, age, τ, z) are also reported. The OPT, K_s and IRAC labels indicate the sub-sample at which each source belongs.

CHAPTER 6

The Evolution of the Galaxy Stellar Mass Function

In the previous chapter we have determined the main galaxy properties needed to study the evolution of galaxies with different star-formation activity. In this chapter we explain how we derived the Galaxy Stellar Mass Function (GSMF) of our high redshift sample to study the different evolution of the galaxies depending on their SSFR, as well as how we derived the stellar mass density of the different galaxy classes. Finally, we compared our results with theoretical models to put some constrains on the existence of high redshift quiescent galaxies.

6.1 The Galaxy Stellar Mass Function

The Galaxy Stellar Mass Function represents the number of galaxies observed with masses in the range $[M, M + dm]$ per unit volume. As the Luminosity Function (LF) it is a fundamental tool when studying galaxy evolution, as it accounts for the change in the properties of the observed galaxies at different epochs of the history of the universe. The GSMF is easier to interpret than the LF as it directly contains information about how does the number of galaxies of a given mass change with time. However, it is less straight forward to derivate than the LF, as the observed luminosities have to be converted into stellar masses, with the corresponding uncertainties.

The GSMF is usually expressed in the form of a Schechter (1976) function:

$$\phi(M)dM = \phi^* \left(\frac{M}{M^*}\right)^{\alpha} exp\left(\frac{-M}{M^*}\right) d\left(\frac{M}{M^*}\right) \quad (6.1)$$

There are three unknown parameters in the expression: the normalization ϕ^*, the faint end slope α and the characteristic mass M^*, which is representative of the knee of the function , *i.e.* separates the exponential part of the function, dominant at high masses, and the power law part, more important in the low mass range. These parameters are supposed to change with cosmic time and their evolution gives some hints on how does the mass of the galaxies changes during the history of the universe. There is also a dependence of these parameters on the galaxies properties, such us morphology or star-formation activity, which is the parameter analyzed in this work.

We studied the evolution of the high redshift sample by deriving their mass function in four different redshift bins: 1.4-1.6,1.6-2.0, 2.0-2.5 and 2.5-3.0. At $z > 3.0$ the uncertainties become dominant so we decided to limit our analysis to $z \leq 3.0$. The mass function of the quiescent, the star forming and the intermediate galaxies are also estimated to compare the evolution of the different populations. We used the classical non-parametric $1/V_{max}$ formalism (Schmidt, 1968) and we fitted the obtained data with a Schechter function (Schechter, 1976) in the four redshift bins. The galaxy stellar mass function GSMF is computed only in the non-masked regions with a total covered area of 1.73 deg^2.

6.1.1 The $1/V_{max}$ Method

There are several methods to calculate the GSMF. The most commonly used are the $1/V_{max}$, the C^- and the STY, all of them presenting some advantages and inconveniences. In this work we used the so-called *classical method*, first published by Schmidt (1968). Its main advantage is its simplicity and the fact that it is a non parametric estimator, *i.e.* it does not assume the shape of the GSMF. The main disadvantages are its sensitivity to density fluctuations and the loss of information on where in the mass bin a galaxy is located. However one can overcome this problems by reducing the mass bin dM and by using large surveys like the COSMOS survey, which substantially reduces density fluctuations due to the cosmic variance because of its large size.

The GSMF can be computed through the $1/V_{max}$ formalism. After dividing the

sample into redshift bins, the GSMF for each mass bin centered in M_j is:

$$\phi(M_j)dM_j = \sum_{|M_i - M < dm/2|} \frac{1}{V_{max,i}} = \sum_{|M_i - M < dm/2|} \frac{1}{V_{zmax,i} - V_{zmin,i}} \tag{6.2}$$

where the i index represents all the sources with a mass value entering the mass bin j considered. In each redshift bin, the co-moving volume available to each source i is def ned as $V_{max,i} = V_{zmax,i} - V_{zmin,i}$. The $z_{max,i}$ value corresponds to the maximum redshift at which a source would still be included in the sample, given the limiting 3.6 μm f ux, while $zmin, i$ is the lower limit of the considered redshift bin. In any case, $zmax, i$ should be smaller than the maximum redshift of the bin considered. $V_{zmax,i}$ and $V_{zmin,i}$ can be computed as

$$V_{z_{max,i}} = \int_0^{min(z_2, z_{\max})} area(z, M) \times \frac{dV(z)}{dz} dz \tag{6.3}$$

$$V_{z_{min,i}} = \int_0^{z_1} area(z, M) \times \frac{dV(z)}{dz} dz \tag{6.4}$$

$$\tag{6.5}$$

$[z_1, z_2]$ are the limits in each redshift bin and the area(z, M) is the area where a source is visible, which depends on the absolute magnitude of the source and the redshift considered.

The absolute magnitude $\mathcal{M}$ as a function of the observed magnitude m, the redshift z, the luminosity distance D_L and the k-correction $k(z)$ is:

$$\mathcal{M} = m - 5logD_L(z) - 25 - k(z) \tag{6.6}$$

If we impose the observed magnitude m to be the magnitude limit of the survey ($m_{lim} = 22.0mag$ for the IRAC1 band in this work) and we solve the equation we obtain the z_{max} value for each source needed to compute the GSMF.

$$\mathcal{M} = m_{lim} - 5logD_L(z_{max}) - 25 - k(z_{max}) \tag{6.7}$$

D_L and K-correction

In eq. 6.6 we have introduced two important functions: the luminosity distance D_L and the k-correction $k(z)$.

As explained in Hogg (1999) the luminosity distance $D_{\rm L}$ is defined by the relationship between bolometric (*i.e.*, integrated over all frequencies) flux S and bolometric luminosity L:

$$D_{\rm L} \equiv \sqrt{\frac{L}{4\pi S}} \tag{6.8}$$

D_L can also be written as:

$$D_L = (1+z)D_M \tag{6.9}$$

For a flat universe ($\Omega_k = 0$) $D_M = D_C$. The co-moving distance D_C can be expressed as

$$D_{\rm C} = D_{\rm H} \int_0^z \frac{dz'}{E(z')} \tag{6.10}$$

where $D_{\rm H}$ is the Hubble distance

$$D_{\rm H} \equiv \frac{c}{H_0} = 3000\,h^{-1}\ {\rm Mpc} = 9.26 \times 10^{25}\,h^{-1}\ {\rm m} \tag{6.11}$$

and $E(z)$ is a function defined as

$$E(z) \equiv \sqrt{\Omega_{\rm M}\,(1+z)^3 + \Omega_k\,(1+z)^2 + \Omega_\Lambda} \tag{6.12}$$

The *k*-correction is a correction to convert the observed magnitude of one object at a given redshift to its rest-frame emission. Because of the expansion of the Universe, the observed SED of a galaxy is redshifted with respect to the rest-frame SED. It consists of two terms, the first one accounting for the difference between the observed flux and the flux of the galaxy at rest, while the second accounts for the different energy associated to the photons moving from the observed to the rest-frame system. It can be expressed as:

$$k(z) = 2.5log\frac{\int f(\lambda, t_0)R(\lambda)d\lambda}{\int f(\frac{\lambda}{1+z}, t_0)R(\lambda)d\lambda} + 2.5log(1+z) \tag{6.13}$$

Here $f(\lambda, t_0)$ is the best-fitting model SED at a given observed wavelength, while $R(\lambda)$ is the transmission function of the considered filter.

6.1.2 Mass Limit

An important factor to take into account when deriving a GSMF is the mass limit M_{lim}, *i.e.* the minimum mass for which, given the characteristics of the survey, all galaxies are observed. At masses higher than M_{lim} the GSMF is complete, while for lower values galaxies can be missed and the GSMF can only be considered as a lower limit. However, estimating the stellar mass limit for a magnitude limited sample is not straightforward due to the high range of possible mass to light M/L ratios for different galaxy populations and colors. To account for this effect we def ned, at each redshift, a minimum mass, M_{min}, above which the derived GSMF is essentially complete because all types of galaxies are potentially observable above this mass.

Following Pozzetti et al. (2010), we calculated for each galaxy its limiting stellar mass, *i.e.* the mass it would have at its redshift if its observed magnitude were equal to the limiting magnitude of the sample ($mag_{3.6lim} = 22.0$):

$$log(M_{lim}) = log(M) + 0.4(mag_{3.6} - mag_{3.6,lim}) \tag{6.14}$$

The result is a distribution of the limiting stellar masses, which ref ects the distribution of M/L ratio at each redshift for our sample. To avoid using a too stringent limit due to the brightest and reddest galaxies we used the M_{lim} of the 20% faintest galaxies at each redshift. We then def ned the $M_{min}(z)$ as the upper envelope of the M_{lim} distribution below which the 95% of the M_{lim} values at each redshift lies. This M_{min} corresponds to a 95% completeness limit at each redshift.

In Fig.6.1 we plotted the mass distribution of our sample (gray crosses) as well as the M_{lim} of the 20% faintest galaxies at each redshift upt o $z = 3$ (red crosses). The $M_{min}(z)$ for each redshift bin calculated as explained above are shown as yellow circles.

6.1.3 Galaxy Stellar Mass Function Errors

The errors associated to the GSMF are usually derived using Poissonian statistics (see, *e.g.* Zucca et al. 1997):

$$\sigma \simeq \frac{\phi_M}{\sqrt{N}} = \left[\sum_i \frac{1}{V^2_{max}(M_i)} \right]^{1/2} \tag{6.15}$$

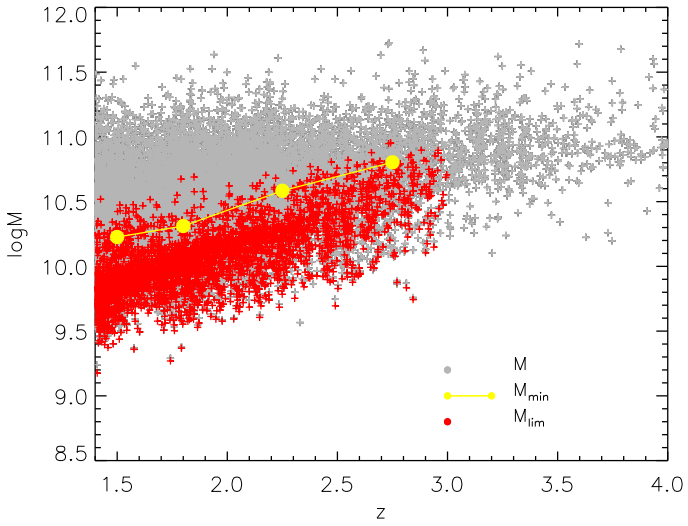

Figure 6.1: Stellar mass as a function of redshift (gray crosses). Red crosses are the M_{lim} of the 20% faintest galaxies at each redshift (up to $z = 3$), while $M_{min}(z)$ are plotted as yellow circles.

However, the Poisson errors in our GSMF are an under-estimate of the real uncertainties, since they do not take into account how the photometric redshifts z_p uncertainties propagate on the GSMF, neither the cosmic variance. We added in quadrature these errors to the Poissonian errors to obtain more realistic uncertainty estimates.

Montecarlo Simulations

We used the Montecarlo simulations to estimate how the uncertainties on z_p inf uence the GSMF computation. Montecarlo simulations consist on randomly sampling the data and repeating the GSMF computation a given number of times. The uncertainty in z_p is especially important for the optically undetected sources, therefore we have to be very careful in the z-bins where these sources dominate (higher redshift).

For the galaxies without spectroscopic redshifts, the z_p represents the best-f tting solution to the observed SED, as explained in Sect. 5.3.1. However, for each solution, together with the best-f tting value, the *LePhare* code supplies also a redshift probability distribution function (PDFz). In order to perform the Montecarlo simulations we created 20 mock catalogs by randomly picking a

Table 6.1: Volume, number density, bias, variance of dark matter and cosmic variance for our sample in each redshift bin as derived using the Somerville formalism and the values obtained from Figs. 6.2 and 6.3.

z bin	V(Mpc^3)	Number density (Mpc^{-3})	b	σ_{DM}	σ_v
1.4-1.6	3.7×10^5	1.4×10^{-2}	1.2	0.15	0.18
1.6-2.0	7.9×10^5	7.9×10^{-3}	1.4	0.10	0.14
2.0-2.5	1.0×10^6	4.5×10^{-3}	1.8	0.08	0.14
2.5-3.0	1.0×10^6	1.7×10^{-3}	2.4	0.07	0.16

redshift within the redshift probability distribution function of each object. With this new redshift values we recalculated the mass and other important physical parameters through the SED-fitting as explained in Sect. 5.4. Then we computed the GSMF for each of the 20 mock catalogs. The 1σ dispersion of the GSMF values at each mass and redshift bin represents the 1σ dispersion to account for the z_p uncertainties in the GSMF computation. We added these values in quadrature to the Poissonian errors.

Cosmic Variance

The cosmic variance is another important source of uncertainty, specially in deep surveys, which usually cover a small area. It accounts for the inhomogeneity of the universe and the large scale structure, *i.e.* the different properties observed when studying different regions of the sky. Obviously, the larger the area studied, the less significant becomes the cosmic variance.

We derived the error associated to cosmic variance for our sample making use of the formalism described in Somerville et al. (2004). Basically, the cosmic variance σ_v for a population is given by

$$\sigma_v = b\sigma_{DM} \tag{6.16}$$

where b is the bias and σ_{DM} is the variance of dark matter. From Fig. 3 of Somerville et al. (2004) (Fig. 6.2 and 6.3 in this work) one can obtain b and σ_{DM} at a given redshift for the characteristic volume and number density of the sample.

Using this method we are able to calculate the cosmic variance σ_v, as shown in Table 6.1.

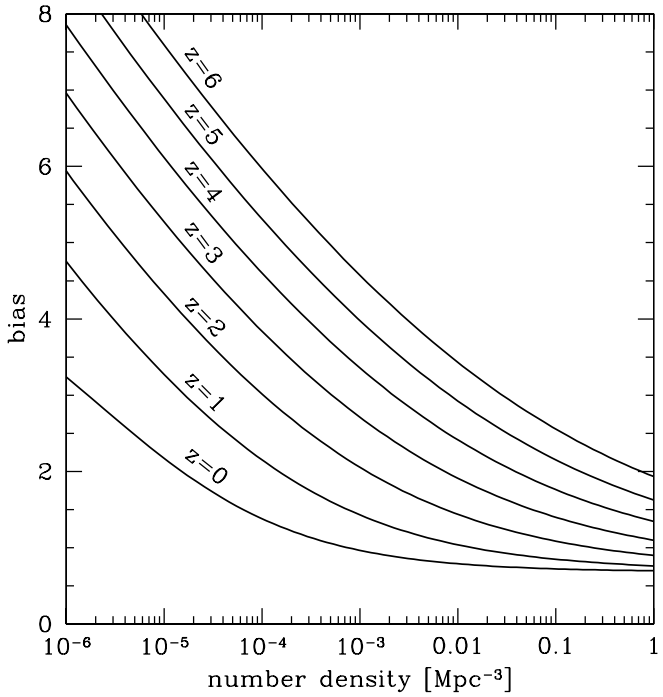

Figure 6.2: Reproduced from Somerville et al. (2004). Bias as a function of comoving number density for dark matter halos at different redshifts.

6.1.4 Comparison of the Total Galaxy Stellar Mass Function with the Literature

In Fig. 6.4 the total (yellow) and the quiescent (red) GSMF (QSMF hereafter) of our IRAC selected sample in 4 different redshift bins (1.4-1.6, 1.6-2.0, 2.0-2.5 and 2.5-3.0) are reported.

We also show for comparison the GSMF derivations from the literature (green asterisks from Fontana et al. 2006, blue triangles from Pérez-González et al. 2008, red diamonds from Marchesini et al. 2009, orange squares from Ilbert et al. 2010). All GSMF's were converted to Chabrier IMF and shifted by −0.14 dex in mass (to account for the difference in the derived mass when using Maraston 2005 or Bruzual & Charlot 2003 models, see Pozzetti et al. 2010). We are in reasonably good agreement with many of the other results. However, a signif cant difference is observed in all redshift bins at high masses with respect to the results of Pérez-González et al. (2008), as they found a number density signif cantly higher than ours. With respect to Marchesini et al. (2009), we f nd less massive galaxies at $z < 2$ and more intermediate mass ($logM \sim 10.5$) galaxies at $2 < z < 2.5$. The

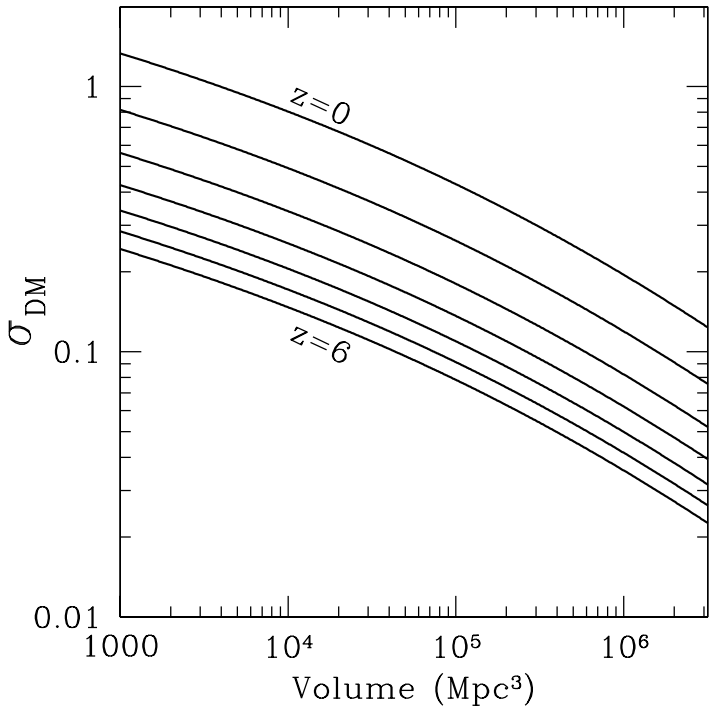

Figure 6.3: Reproduced from Somerville et al. (2004). Variance of dark matter as a function of volume from linear theory at different redshifts.

agreement with Ilbert et al. (2010), whose sample is also IRAC selected in the COSMOS f eld, is very good, with small differences probably arising from different redshift binning, as it may happen also with Fontana et al. (2006). However, we have a slight over-density of intermediate mass galaxies ($M \sim 10^{10.7}$M$_\odot$) at $2.0 < z < 2.5$ when compared with all other results from literature, which may be too big to be explained only by differences in redshift binning.

In comparison with other authors, we are using data from the COSMOS survey, which is the largest studied area (~ 1.7 deg^2) with full multi-wavelength coverage.

6.2 The Evolution of Galaxies with Different Star Formation Rates

In Fig. 6.5 the GSMF of quiescent galaxies obtained in the four studied redshift bins is reported. The shaded areas represent the upper and lower limits, derived as explained in Sect. 6.1.3, while the thick lines are the Schechter f tting to the data.

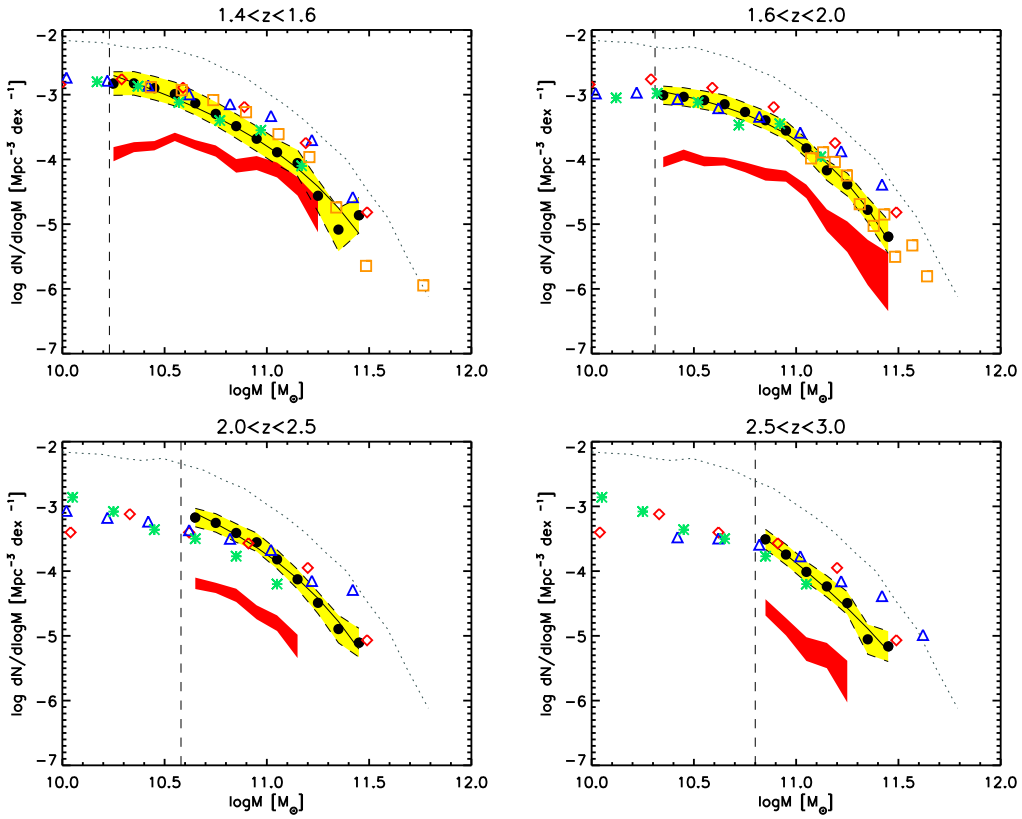

Figure 6.4: Stellar mass function in 4 redshift intervals for the quiescent (red area) and the total (yellow area) sample. Our estimates, at each redshift, for the whole sample are plotted as filled black circles. Data are fitted with a Schechter function (solid lines). The colored areas represent the upper and lower limits of the total and quiescent mass functions as derived from the combination of the Montecarlo simulations, cosmic variance and Poissonian errors. Black dotted line: local MF (Cole et al., 2001). Dashed vertical lines represent the completeness in mass for each redshift bin. GSMFs from other authors are also plotted: green astrerisks from Fontana et al. (2006), blue triangles from Pérez-González et al. (2008), red diamonds from Marchesini et al. (2009), orange squares form Ilbert et al. (2010).

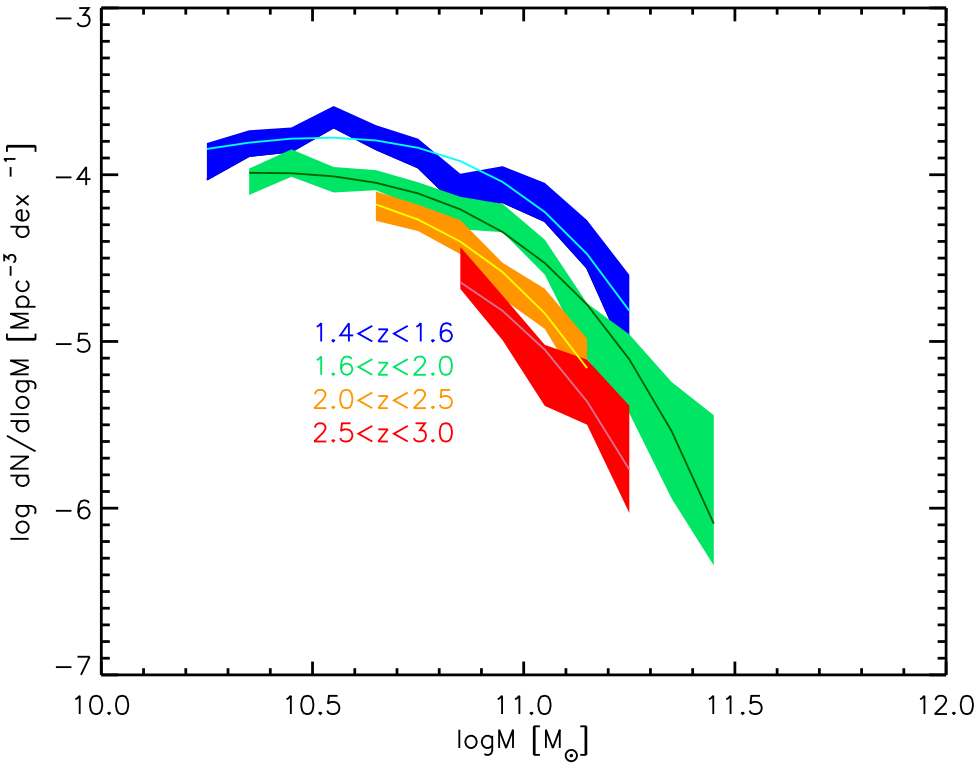

Figure 6.5: Evolution of the QSMF with redshift for different redshift bins. Blue: 1.4 – 1.6; green: 1.6 – 2.0 ; orange: 2.0 – 2.5; red: 2.5 – 3.0. Shaded regions represent the upper and lower limits of the GSMF for each redshift bin (see Sect. 6.1.3), while the thick lines are the Schechter f tting to the data.

A signif cant evolution of the QSMF from $2.5 < z < 3.0$ to $1.4 < z < 1.6$ is observed, increasing ~ 1 dex for galaxies with $logM \sim 11.0$ in the redshift interval studied. The evolution is ~ 0.3 dex in each redshift bin, meaning that the number of quiescent galaxies continuously increases with cosmic time.

In Fig. 6.6 we compare the GSMF derived for quiescent galaxies, with those of the other populations. The red, green and blue areas represent the quiescent, intermediate and actively star-forming populations, respectively. We also show for comparison the results obtained by Ilbert et al. (2010), with purple, dark green and light blue circles representing their quiescent, intermediate and high activity galaxies respectively. The agreement is good for the quiescent population in both redshift bins in common ($1.4 - 1.6$, $1.6 - 2.0$), while the differences for the intermediate and star-forming population can be explained by the different classif cation methods used. While for the quiescent population we used a similar cut in SSFR, for the cut between the intermediate and high activity populations they used $log(SSFR[\mathrm{Gyr}^{-}1]) \sim -0.3$, while we are using a value of -0.5.

The evolution of the star-forming galaxies is quite complex (see Fig. 6.6). They remain almost constant from $2.5 < z < 3.0$ to $2.0 < z < 2.5$, being the dominant population at all masses in those redshift bins. However, their number density decreases when moving to the lowest redshift bins and this decrease depends on the galaxy mass: while for high masses we observe a signif cant decline (~ 0.8 dex for $logM \sim 11.0$), for low masses ($logM \sim 10.5$) the GSMF is almost constant. A decrease of the star-forming population from $1.6 < z < 2.0$ to $1.4 < z < 1.6$ is in agreement with the results of Ilbert et al. (2010) and, as reported in studies at lower redshift (see for example Ilbert et al. 2010, Pozzetti et al. 2010), the number of star-forming galaxies continues to decrease to almost local redshift ($z \sim 0.1$). The intermediate population constantly increases its number at all masses, f rst at high masses (~ 0.2 dex from $2.5 < z < 3.0$ to $1.6 < z < 2.0$ for $logM \sim 11.0$), then at low masses (~ 0.2 dex from $1.6 < z < 2.0$ to $1.4 < z < 1.6$ for $logM \sim 10.5$). This means that they become more abundant than the star-forming population at $logM \gtrsim 10.6$ at $1.4 < z < 1.6$. Finally, as mentioned before, for the quiescent population we f nd an increase of ~ 1dex in the number density from $2.5 < z < 3.0$ to $1.4 < z < 1.6$ for $logM \sim 11.0$. At the lowest redshift bin ($1.4 < z < 1.6$) the quiescent population becomes more important than the active one for masses $logM \gtrsim 10.75$.

Considering all the populations, we f nd that $z \sim 1.5$ is a clear epoch of transition

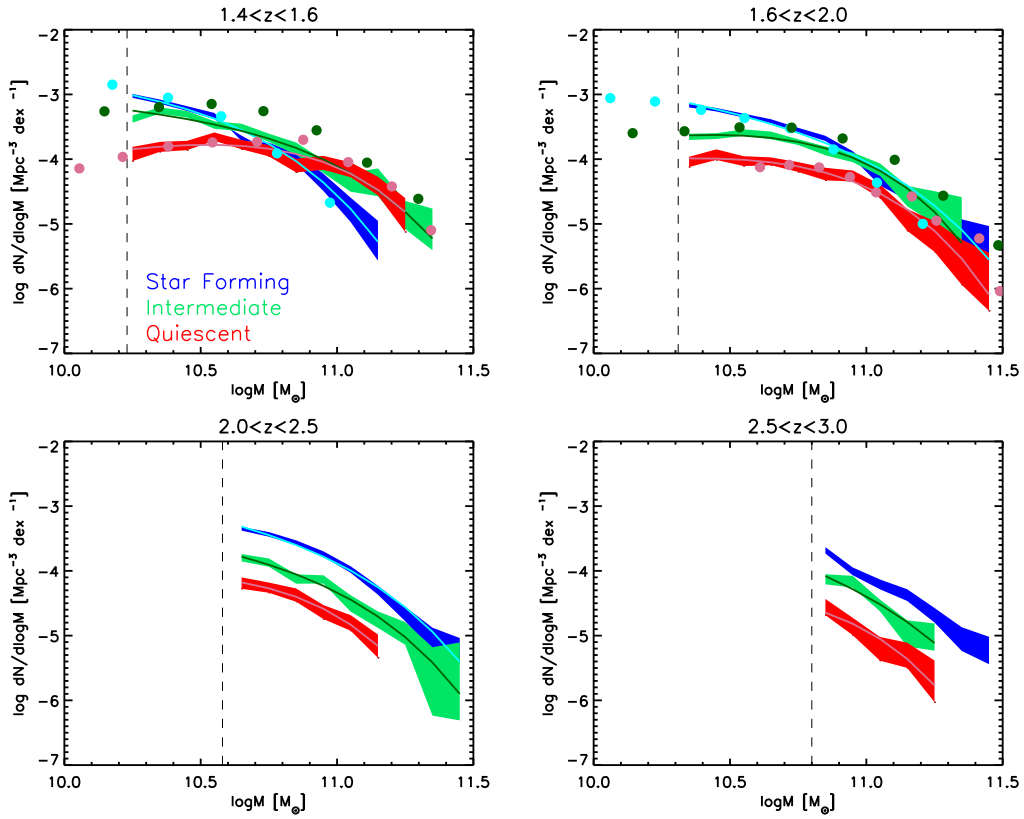

Figure 6.6: Evolution of the GSMF for different activity types galaxies. The colored areas represent the upper and lower limits (see Sect. 6.1.3) while the thick lines are the Schechter f tting to the data. Red: quiescent. Green: intermediate. Blue: actively star-forming. The circles represent the GSMF for quiescent (purple), intermediate (dark green) and high activity galaxies (light blue), as obtained by Ilbert et al. (2010). Also shown are the limits in mass (vertical dashed lines).

of the GSMF: while the GSMF at $z \gtrsim 1.5$ is dominated by the actively star-forming galaxies at all stellar masses, at $z \lesssim 1.5$ the contribution to the total GSMF of the quiescent galaxies is signif cant and both the intermediate and the quiescent population become more important than the star-forming one for $M \geqslant 10^{10.75}\mathrm{M}_{\odot}$.

In Table 6.2 we report the best-f t Schechter parameters for the quiescent sample. In the last redshift bin ($2.5 < z < 3.0$) the Schechter f t failed to converge when leaving all the parameters free. We f xed the faint end slope α to its value at $2.0 < z < 2.5$ to be able to obtain the other Schechter parameters. While, given the large uncertainties, we cannot derive f rm conclusions on the faint end slope α nor on M^*, we detect, as already mentioned, a signif cant increase of ϕ from $2.5 < z < 3.0$ to $1.4 < z < 1.6$.

Table 6.2: Schechter parameters of the QSMF at $1.4 \leq z \leq 3.0$.

Type	z-bin	α	$log(M^*)[M_\odot]$	$\phi[10^{-4}Mpc^{-3}\ dex^{-1}]$
Quiescent	1.4-1.6	-0.08± 0.98	10.57 ±0.25	1.9± 0.5
	1.6-2.0	-0.41± 0.92	10.61 ±0.19	1.0± 0.4
	2.0-2.5	-0.34± 4.83	10.50 ±0.84	0.9± 0.8
	2.5-3.0	-0.34 (Fixed)	10.52 ±0.18	0.5± 0.6

To better understand the behaviour of the different populations we show the fraction of quiescent/star-forming galaxies over the total versus mass for different redshift bins (Fig. 6.7). The fraction of the actively star-forming galaxies decreases from $\sim$ 60% to $\sim$ 20% from $2.5 < z < 3.0$ to $1.4 < z < 1.6$ for $M \gtrsim 10^{11.0}M_\odot$, while that of quiescent galaxies increases from $\sim$ 10% to $\sim$ 50% in the same redshift and mass intervals. The evolution is also mass-dependent, with the most massive galaxies becoming quiescent first, while at $M \lesssim 10^{10.5}M_\odot$ the star-forming population still dominates the sample at all redshifts.

This trend suggests that actively star-forming galaxies, which dominate the sample at high redshifts (mainly at $z \gtrsim 2.0$), may quench their star formation and become less abundant at later time. This quenching of the star formation seems to be mass dependent, with the most massive galaxies quenching their star-formation first, while the less massive galaxies continue to form stars until later times. If the evolution of the star-forming galaxies should be that of becoming intermediate galaxies to finally end their lives as quiescent galaxies, the increase of this latter population at low redshifts could be explained, with the quiescent population being the dominant population at low redshift, as all galaxies may evolve to that type once their star formation has stopped. Therefore, we could be unveling the formation epoch of the very active galaxies and their following evolution from the blue cloud to the red sequence (See Sect. 4.3, Fig. 4.4).

6.2.1 Stellar Mass Density

Once the GSMF is known it is straight forward to derive the stellar mass density by simply integrating over all the masses range:

$$\rho_{SM} = \int M\phi(M)dM \tag{6.17}$$

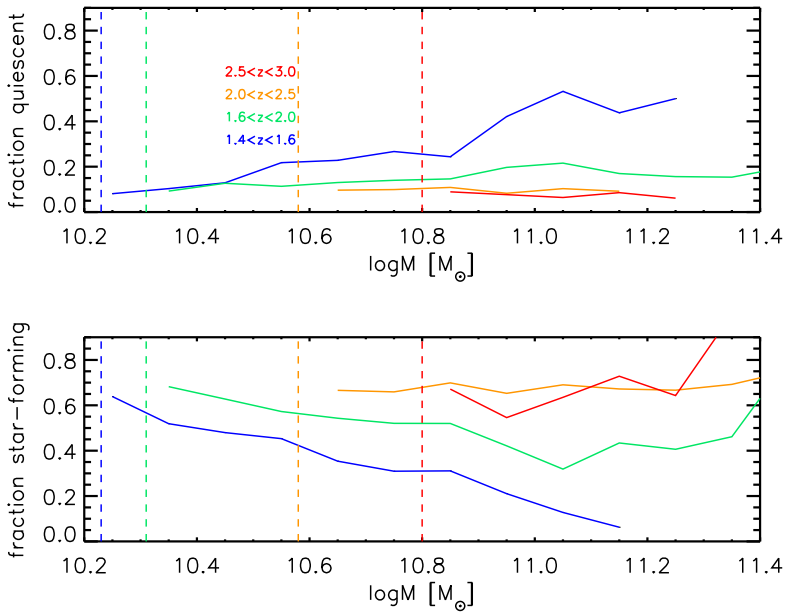

Figure 6.7: Upper panel: Fraction of quiescent galaxies over total for different mass values. Colors represent the different redshift bins as in Fig. 6.5. Lower panel: Fraction of the star-forming population over total versus mass. Colored vertical dashed lines are the mass limits for each redshift bin.

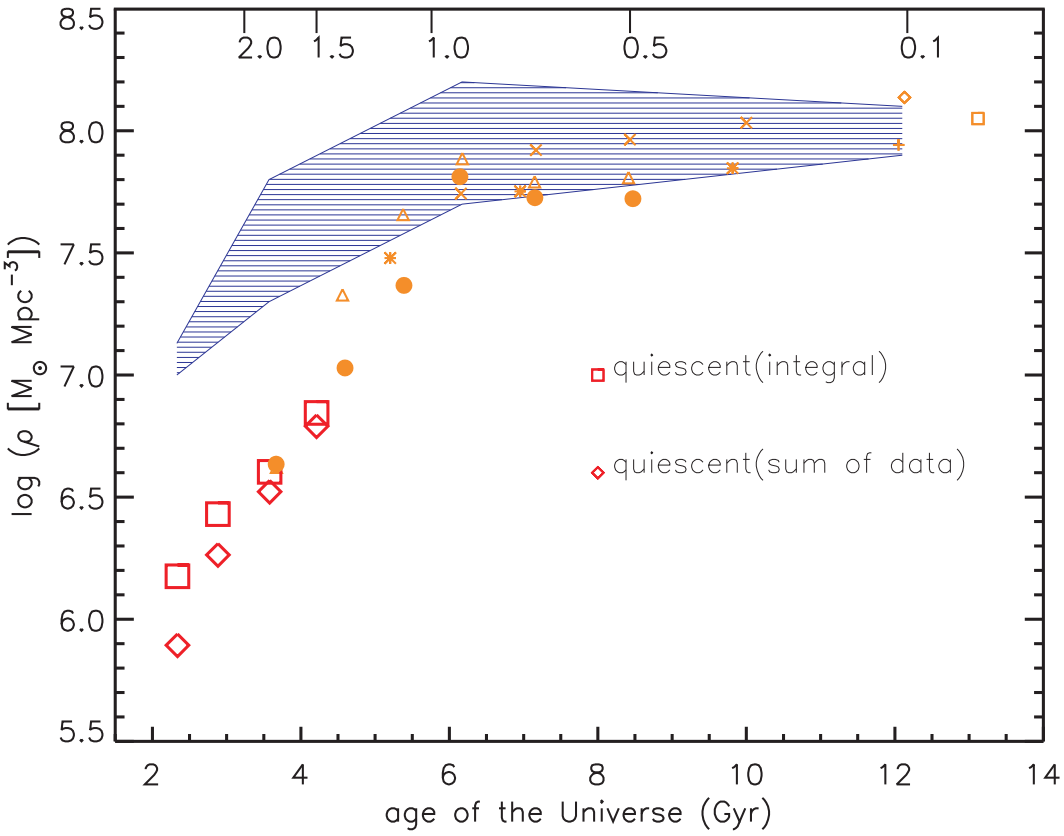

Figure 6.8: Evolution of the stellar mass density of quiescent galaxies. The result from this work are the red symbols. The values represented by the squares have been calculated as the integral of the Schechter function f tting the data, while the diamonds are a mere sum of the data for all masses. Orange symbols are results from literature as explained in the article. We also show for comparison the evolution of the stellar mass density of the star-forming plus the intermediate galaxies (blue shaded area).

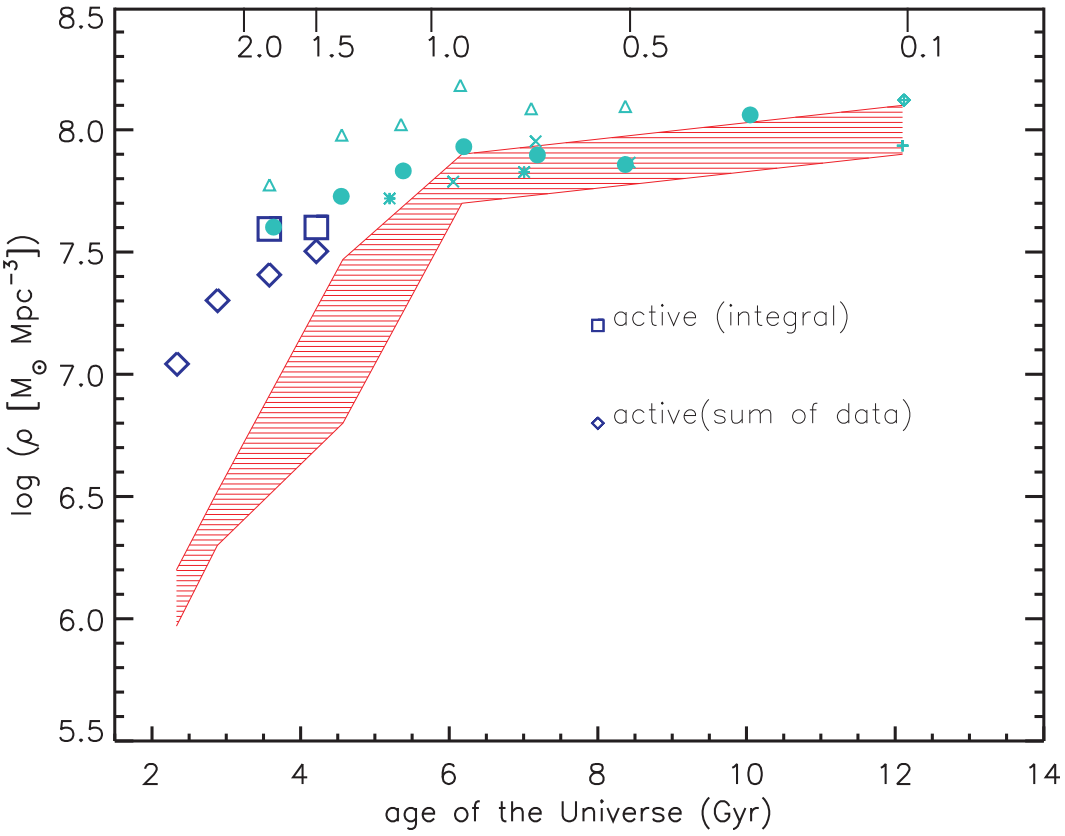

Figure 6.9: Evolution of the stellar mass density of star-forming plus quiescent galaxies. The result from this work are the dark blue symbols. The values represented by the squares have been calculated as the integral of the Schechter function f tting the data, while the diamonds are a mere sum of the data for all masses. Light blue symbols are results from literature as explained in the article. We also show for comparison the evolution of the stellar mass density of the quiescent galaxies (red shaded area).

In Fig. 6.8 and 6.9 we calculated the evolution of the stellar mass density with cosmic time for the quiescent sample (red symbols) and the intermediate plus the star-forming samples (dark blue). The values were obtained in two different ways. The data plotted as squares represent the integral of the Schechter function f tting our data, including the extrapolations to the fainter masses. The diamonds are the sum of the data at all masses. As expected, the latter values are lower (since data are incomplete at low masses) but the two estimates are consistent within ~ 0.18 dex. We do not show the value of the stellar mass density for the intermediate and star-forming galaxies in the redshift bins $2.0 - 2.5$ and $2.5 - 3.0$ derived through the integration of the Schechter parameters, neither the same value at $2.5 < z < 3.0$ for the quiescent galaxies, due to the high uncertainties in the derived parameters given the incompletness at low masses. In the plots we also show a colored area representing the upper and lower limits of the quiescent (red) and star-forming (blue) populations, as well as various results from literature. Orange symbols represent the stellar mass density of the quiescent galaxies as derived by other authors, while light blue symbols stand for the star-forming ones (squares from Kochanek et al. (2001), plus symbols from Bell et al. (2003), diamonds from Driver et al. (2006), asterisks from Franceschini et al. (2006), crosses from Borch et al. (2006), triangles from Arnouts et al. (2007), dots from Ilbert et al. (2010)). We are in very good agreement with Ilbert et al. (2010) in the common redshift bins. We observe that the increase in stellar mass density in the redshift range of interest ($t \sim 2 - 4.5$ Gyr) is very rapid for both populations (~ 0.5 dex for the star-forming plus intermediate populations and ~ 0.9 dex for the quiescent one), then slowing down at lower redshifts. However, this slow down happens earlier in time for the star-forming population ($z \sim 1.2$, $t \sim 5.0$ Gyr) than for the quiescent galaxies, which continue to rapidly assembly mass until later times ($z \sim 1.0$, $t \sim 6.0$ Gyr), reaching the star-forming galaxies mass density at $z < 1.0$.

The existence of a non negligible population ($log\rho[M_\odot\ Mpc^{-3}] \sim 6.0$ at $z \sim 2.7$) of quiescent galaxies with high masses which have already undergone major star formation even at the highest redshifts ($z > 2.5$) is fundamental for our understanding of the galaxy formation processes and crucial for testing theoretical scenarios.

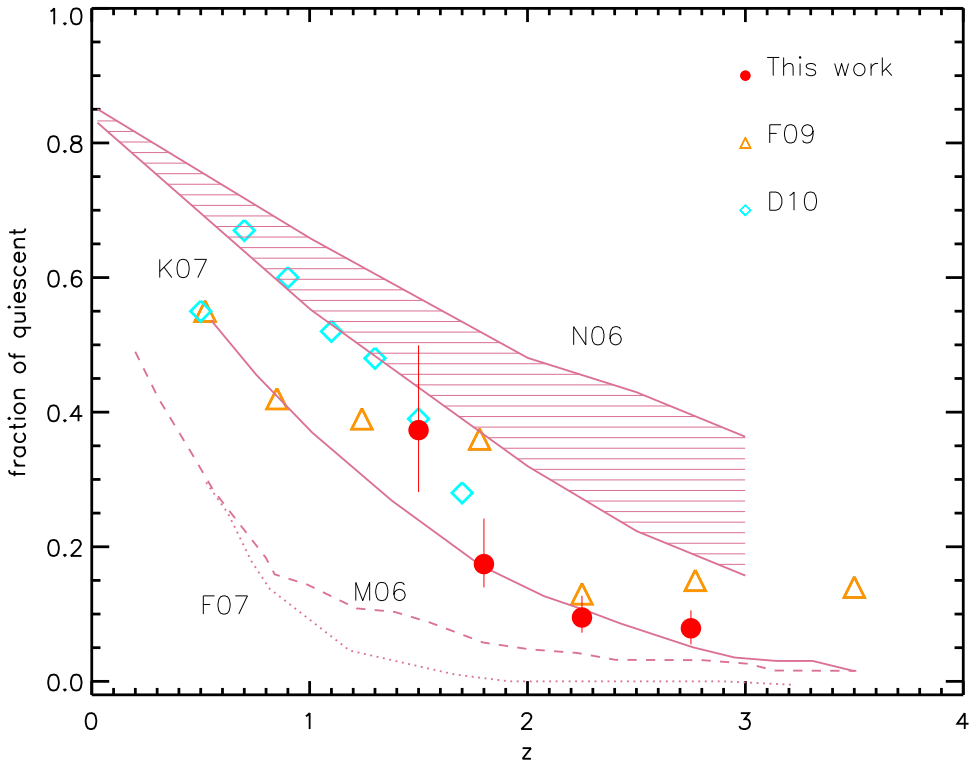

Figure 6.10: Fraction of quiescent galaxies ($log(SSFR[\mathrm{Gyr}^1]) < -2$) with $M \geq 10^{10.85}\mathrm{M}_\odot$ as a function of redshift. Red circles are the results obtained in this work (errors are the combination of the Poisson errors and the Montecarlo simulations), orange triangles are the values from Fontana et al. (2009) and light blue diamonds from Damen et al. (2010). Lines refer to the predictions of theoretical models as decribed in the legend: Menci et al. (2006) (M06), Nagamine et al. (2006) (N06), Kitzbichler & White (2007) (K07) and Fontanot et al. (2007) (F07).

6.2.2 Comparison with Theoretical Models

Fig. 6.10 shows the evolution of the fraction of quiescent galaxies with redshift for sources with $M \geq 10^{10.85}\mathrm{M}_{\odot}$ (red circles). The errors are a combination of the Montecarlo simulations and Poissonian errors. For comparison, we also plotted the values obtained by Fontana et al. (2009, orange triangles) and from Damen et al. (2010, light blue diamonds), as well as the predictions of theoretical models (Menci et al. 2006, M06 hereafter; Nagamine et al. 2006, N06; Kitzbichler & White 2007, K07; Fontanot et al. 2007, F07). We observe a good agreement between the fraction of quiescent galaxies derived in this work and those from Fontana et al. (2009). The values of Damen et al. (2010) are also consistent with our results, although Damen et al. (2010) sources are selected with $M > 10^{11.0}\mathrm{M}_{\odot}$ and are def ned as quiescent when $SSFR < 1/(3t_H)$. The fraction of massive quiescent galaxies increases from $\sim$ 8% to $\sim$ 35% from $2.5 < z < 3.0$ to $1.4 < z < 1.6$, with the main evolution occuring between $1.6 < z < 2.0$ and $1.4 < z < 1.6$ (where the fraction increases from $\sim$ 18% to $\sim$ 35%). This conf rms the expected cosmological increase in number density of massive quiescent galaxies with cosmic time. All the theoretical models agree in predicting a gradual increase with time in the fraction of galaxies with low SFR, although large discrepancies between data and theoretical models are observed. It is beyond the scope of this thesis to give a detailed explanation of the differences between models, but we will discuss some generalities. Some models underpredict the fraction of quiescent galaxies at all redshifts, such as the purely semi-analytical models (M06, F07), and in particular predict virtually no such objects at $z > 2$, in contrast to what is observed. This lack of massive galaxies at high redshift for the model of F07 has already been noticed by Fontanot et al. (2007), who admitted that the downsizing trend of the galaxies is not fully reproduced yet in these models, and suggested that some kind of feedback mechanism could help to reproduce the data. A slightly higher fraction of quiescent massive galaxies is predicted by M06, as they include AGN feedback mechanism, due to the growth of supermassive black holes and the AGN triggered by interactions in the host galaxies. This AGN feedback enhances the fraction of galaxies populating the red branch of the color distribution and is particularly effective at high z. However, it is not effective enough to reproduce the observed data at $z < 2.0$. The purely hydro-dynamical model by Nagamine et al. (2006), represented with a shaded area for three different timescales τ of the star-formation rate (ranging from 2×10^7 yrs to 2×10^8 yrs), appears to overpredict the fraction

of high mass quiescent galaxies. The disagreement in the stellar mass density at $z > 1$ between these models and the observations has already been commented by Nagamine et al. (2006). The semi-analytical rendition of the Millennium N-body dark matter simulation by Kitzbichler & White (2007) is the only one which agrees with our observed data, being able to reproduce both the normalization and the shape of the increase in the fraction of quiescent massive galaxies with decreasing redshift. This model introduces radio mode feedback from the central galaxies of groups and clusters, which seems to be fundamental for the predictions to be consistent with the observations.

Finally, the non negligible fraction of quiescent galaxies at $z > 1.8$ implies that these galaxies assembled most of their stellar mass either during an active star-burst phase or through important merging processes at higher redshifts. These star formation episodes must be quenched either by eff cient feedback mechanism and/or by the stochastic nature of the hierarchical merging process.

CHAPTER 7

Comparison of Star Formation Rate Estimates

We have already discussed the importance of the SFR and we have seen how galaxies with different SSFR behave and evolve in very different manners. It is then of extreme importance to have an accurate way to measure the SFR. One of the most commonly used quantities to derive the SFR is the Far-IR emitted radiation (see Sect. 3.3.4). However, as already mentioned, the calibration of the far-IR light as star formation rate proxy is based on a theoretical relation obtained for a very particular conditions and, strictly speaking, could only be applied to young starbursts. However, it is often used in literature to derive the SFR of any kind of galaxies. We though that the advent of the Herschel Space Telescope, which samples the critical far-IR part of the galaxy spectra, could be an excellent opportunity to empirically test Eq. 7.3 without uncertainties associated to the extrapolation of the IR peak. The most problematic issue, however, is to have a statistically signif cant sample of galaxies with accurate measures of SFR. As we show in Sect. 3.3, all methods to derive the SFR have associated disadvantages and uncertainties. We therefore, had to limit our test to the comparison between the SFR derived from the IR emitted light and the SFR derived from the Hα emission line corrected for extinction (Eq. 3.2). We compared these two SFR indicators for different intrinsic properties of galaxies (redshift, mass, SSFR, metallicity and morphological type).

7.1 Data Analysis

7.1.1 The Herschel Space Observatory

The advent of the ESA Herschel Space Observatory, a far-infrared telescope observing at wavelengths that had never previously been explored to such depths and resolutions, allow us to better resolve the IR peak of the SED of star-forming galaxies and therefore to have a more accurate measure of the SFR from the Infrared Luminosity (L_{IR}) emission.

The Herschel Space Observatory is the largest infrared space observatory launched up to date. Equipped with a 3.5 meter diameter Cassegrain ref ecting telescope, the largest single mirror ever built for a space telescope, and instruments cooled to close to absolute zero, it collects long-wavelength radiation from some of the coldest and most distant objects in the Universe. It observes across the far infrared and sub-millimeter wavelengths (55 - 672 μm), providing data that had been unobtainable before. Lunched in 14 May 2009 and after a roughly 50-day journey from Earth, Herschel entered its operational orbit around the second Lagrange point of the Sun-Earth system (L2), for a nominal mission lifetime of three years.

The Herschel main objectives are to study the formation of galaxies in the early Universe and their subsequent evolution, to investigate the creation of stars and their interaction with the interstellar medium, to observe the chemical composition of the atmospheres and surfaces of comets, planets and satellites or to examine the molecular chemistry of the Universe.

It has three scientif c instruments on board:

- HIFI (Heterodyne Instrument for the Far Infrared), a very high resolution heterodyne spectrometer.
- PACS (Photodetector Array Camera and Spectrometer) - an imaging photometer and medium resolution grating spectrometer.
- SPIRE (Spectral and Photometric Imaging Receiver) - an imaging photometer and an imaging Fourier transform spectrometer.

The interest in observing at far IR wavelengths comes from the fact that large parts of the Universe are too cold to radiate in the visible wavelength range or at shorter wavelengths. To study these cool objects, observations must be performed in the

infrared spectrum or at even longer (sub-millimeter) wavelengths. Besides, many objects of great astronomical interest are concealed within or behind clouds of gas and dust. For example, in the early stages of their formation, stars and planets are surrounded by the gas and dust clouds from which they are being created. Galactic cores and most of the remnants of the early Universe are also hidden from view by dust clouds. The dust particles in these clouds are efficient at scattering or absorbing radiation emitted by these objects. Infrared radiation, instead, is less affected by these clouds - the longer the wavelength, the thicker the dust cloud that it can penetrate- and an important part of the absorbed light is re-emitted at the IR wavelengths.

Pacs Evolutionary Probe

In this thesis we made use of the data in the far-IR from the Herschel PACS Evolutionary Probe (PEP, Lutz et al. 2011) survey. PEP is a Herschel guaranteed time key program survey of the extragalactic sky, aimed to study the rest-frame far-infrared emission of galaxies up to redshift ~ 4, as a function of environment. Making use of the PACS instrument, the PEP survey includes six among the most widely studied blank fields across the sky, two high-redshift galaxy clusters and ten lensing clusters. It includes observation in the COSMOS field, which is the field studied in this work.

The goals of the PEP program are to resolve the Cosmic Infrared Background and determine the nature of its constituents, to determine the cosmic evolution of dusty star formation and of the infrared luminosity function, to try to elucidate the relation of far-infrared emission and environment, and to determine clustering properties. It is also crucial to investigate the contribution of AGN and to calculate the infrared emission and energetics of the different galaxy populations.

In this context, the new PEP Herschel data at long IR wavelengths are fundamental to accurately study the relation between the IR luminosity emitted by star forming galaxies and their star formation rate.

7.1.2 Herschel Selected Sample

We studied the SFR derived from the L_{IR} emission making use of the recent Herschel data in the COSMOS field. The Herschel data includes PACS data from

the PEP survey. We used the PACS blind catalog v2.1 (containing 7313 sources) down to $3\sigma \sim 5$ and 10.2 mJy at 100 and 160 μm, respectively. This catalog was associated using the likelihood ratio technique (see Sect 5.2.1) to the deep 24 μm catalog from Le Floch et al. (private communication) reaching S_{lim}(24 μm)=80 μJy and to the multi-band 3.6 μm selected catalog from Ilbert et al. (2010) to S_{lim}(3.6 μm)= 1 μJy. The 3.6 μm catalog includes *NUV*, u^*, B_J, g^+, V_J,r^+, i^+, z^+, J,K_s, *3.6, 4.5, 5.8, 8.0* and *24 μm* data from GALEX, Subaru, IRAC and Spitzer legacy surveys, respectively. We also needed the spectroscopic information to accurately measure the SFR from the Hα emission line. We have 1654 sources (~ 23 % of PEP catalog) with spectroscopic information from the zCOSMOS 20k spectroscopic survey (see Sect. 5.1), 717 of them with z < 0.46. This cut in redshift is necessary to properly observe the Hα emission line (6562.8 Å) in the optical spectra. We did not consider sources with no accurate redshifts (f ag z ≤ 2.1, Lilly et al. 2009, ~ 5%), neither sources with S/N < 3 in the Hα f ux (~ 25%).

7.1.3 Active Galactic Nuclei Detection

To avoid AGN contamination we have cleaned our sample from possible AGN candidates. We used three methods of AGN detection (X-ray emission, Diagnostic Diagrams, and SED-f tting) to eliminate the sources which were classif ed as AGN by at least one of these methods. We identif ed 47 AGN candidates (~ 6% of the sample) and excluded them from our f nal sample. The f nal sample consists of 474 PEP detected Hα-emitting galaxies with $0.06 < z < 0.46$. We explain in detail the three methods used to identify AGNs.

X-ray Emitting Sources

X-ray luminosity can be produce in starbursts due to X-ray binaries, but it is more frequently due to AGN activity. To ensure a sample with no AGNs we eliminated sources with X-ray emission detected with XXM-Newton (Hasinger et al., 2007) and Chandra (Elvis et al., 2009) Telescopes.

Diagnostic Diagrams

Optical AGNs can be broadly classif ed into two categories, type-1 or type-2 AGN, depending on their emitted optical spectra. According to the standard unif ed model,

when the central black hole and its associated continuum and broad emission-line regions are directly observed, they are classif ed as type-1 AGNs. These objects are easily recognizable from their spectra, characterized by a power-law continuum emission and broad permitted emission lines ($\gtrsim$ 1000 kms^{-1}) and they have been recognized and excluded originally from the zCOSMOS galaxy sample. Type-2 AGNs, instead, are supposed to be obscured by a dusty circumnuclear medium. They have narrow permitted and forbidden lines ($\lesssim$ 1000 kms^{-1}), arising from the gas clouds in the narrow line region, and their continuum is very similar to that of normal star forming galaxies. To distinguish type-2 AGNs from normal star-forming galaxies, the ionizing source must be determined. This is usually done by using diagnostic diagrams based on the intensity ratios of pairs of strong emission lines. BPT (Baldwin, Phillips & Terlevich) diagrams, f rst proposed by Baldwin et al. (1981) and then ref ned by Veilleux & Osterbrock (1987) are based on [OIII] λ5007Å, [OI] λ6300Å, [NII] λ6583Å, [SII] λ6717Å, Hα λ6563Å and Hβ λ4861Å emission lines. For sources with $z < 0.46$ it s possible to use the standard BPT diagram based in the plane [OIII]/Hβ vs [NII]/Hα and [OIII]/Hβ vs [SII]/Hα. The exact limit between the star-forming galaxies and AGNs is subject to considerable uncertainty. However, an analytic expression is adopted for the limiting curves from Bongiorno et al. (2010) between AGNs and starburst region:

$$log\left(\frac{[OIII]}{H\beta}\right) = \frac{0.61}{log([NII]/H\alpha) - 0.47} + 1.19 \tag{7.1}$$

$$log\left(\frac{[OIII]}{H\beta}\right) = \frac{0.72}{log([S\,II]/H\alpha) - 0.47} + 1.45 \tag{7.2}$$

Starburst are located below these lines, while type-2 AGNs are above. There is an intermediate region, separated by a demarcation line def ned by Kauffmann et al. (2003), were composite objects are located. A further distinction in the AGN region can be made by separating the sample into Seyfert-2 galaxies and low ionization nuclear emission regions (LINERs, [OIII]/Hβ < 3.0; Heckman 1980).

In Fig. 7.1 and 7.2 we report the BPT diagrams from Bongiorno et al. (2010). Using a S/N criteria (S/N(OIII) > 5 and S/N(other)> 2.5 for the other lines involved in the diagrams) they classif ed 128 sources as type-2 AGNs, of which 31 are Sey-2 and 97 LINERs. It is still unclear whether all LINERs are AGNs. However we eliminated from our sample both the Sey-2 and the sources classif ed as LINERs to ensure a clean sample of normal star-forming galaxies.

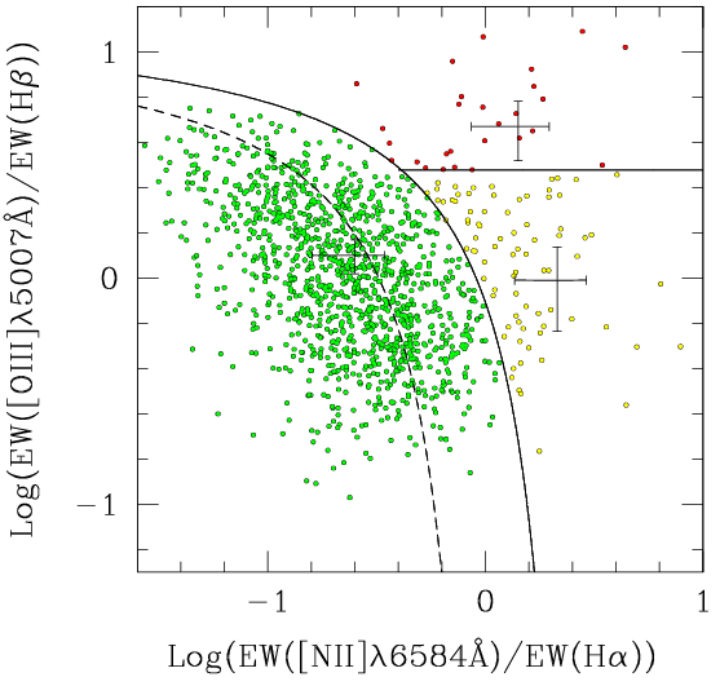

Figure 7.1: Reproduced from Bongiorno et al. (2010). log([OIII]/Hβ) vs log([NII]/Hα). The solid lines are the separation between SFGs and AGNs and between Sey-2 and LINERs. The dashed line shows the separation between composite objects. Red circles correspond to objects classif ed as Sey-2, yellow squares are objects classif ed as LINERs and green triangles are normal Star-forming galaxies.

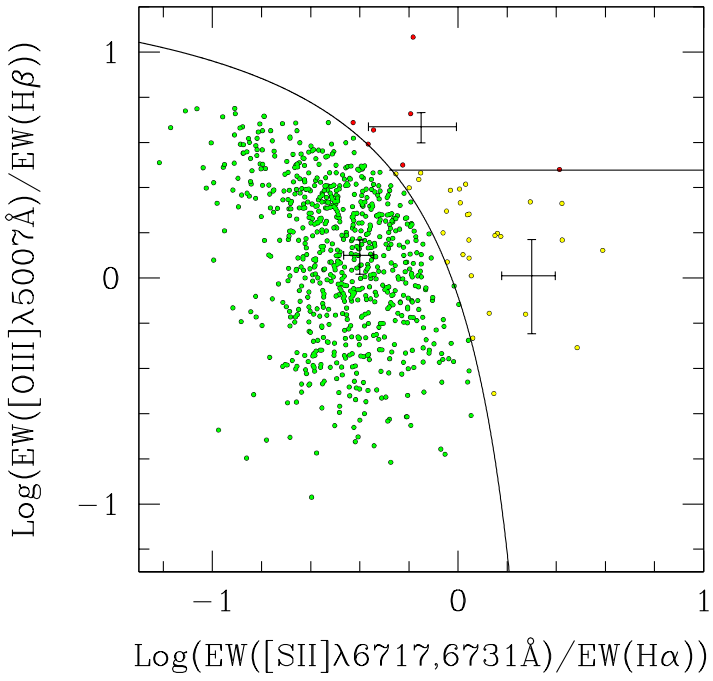

Figure 7.2: Reproduced from Bongiorno et al. (2010). log([OIII]/Hβ) vs log([SII]/Hα). Lines and colors as in Fig. 7.1.

SED-f tting

The methods explained before to detect AGNs are limited by the depth of the surveys. For example, there are many sources which do not satisfy the S/N criteria applied to the BPT diagrams. On the other hand, the XMM data are not as deep as the Chandra ones, which in turn do not cover the whole COSMOS area. To avoid missing AGNs that could not be detected by the previous methods we performed a SED-f tting to our multi-wavelength data from NUV to FIR using Polletta et al. (2007) templates as reference spectra. These empirical templates contain observed SEDs from galaxies with very different properties, from elliptical and normal spiral galaxies, to starburst, composite, Seyfert1, Seyfert2 and quasars (QSO) (See Fig. 7.3). We included also the modif ed templates by Gruppioni et al. (2010), which include a higher IR bump to better reproduced the observed PEP f uxes in many FIR selected galaxies. These modif ed templates were created with the arrival of new far-IR data from Herschel. Gruppioni et al. (2010) noted that in ∼10–12% of cases the observed SEDs were very well reproduced by the templates over the entire UV/optical/NIR/IRAC range, while they were systematically underestimated

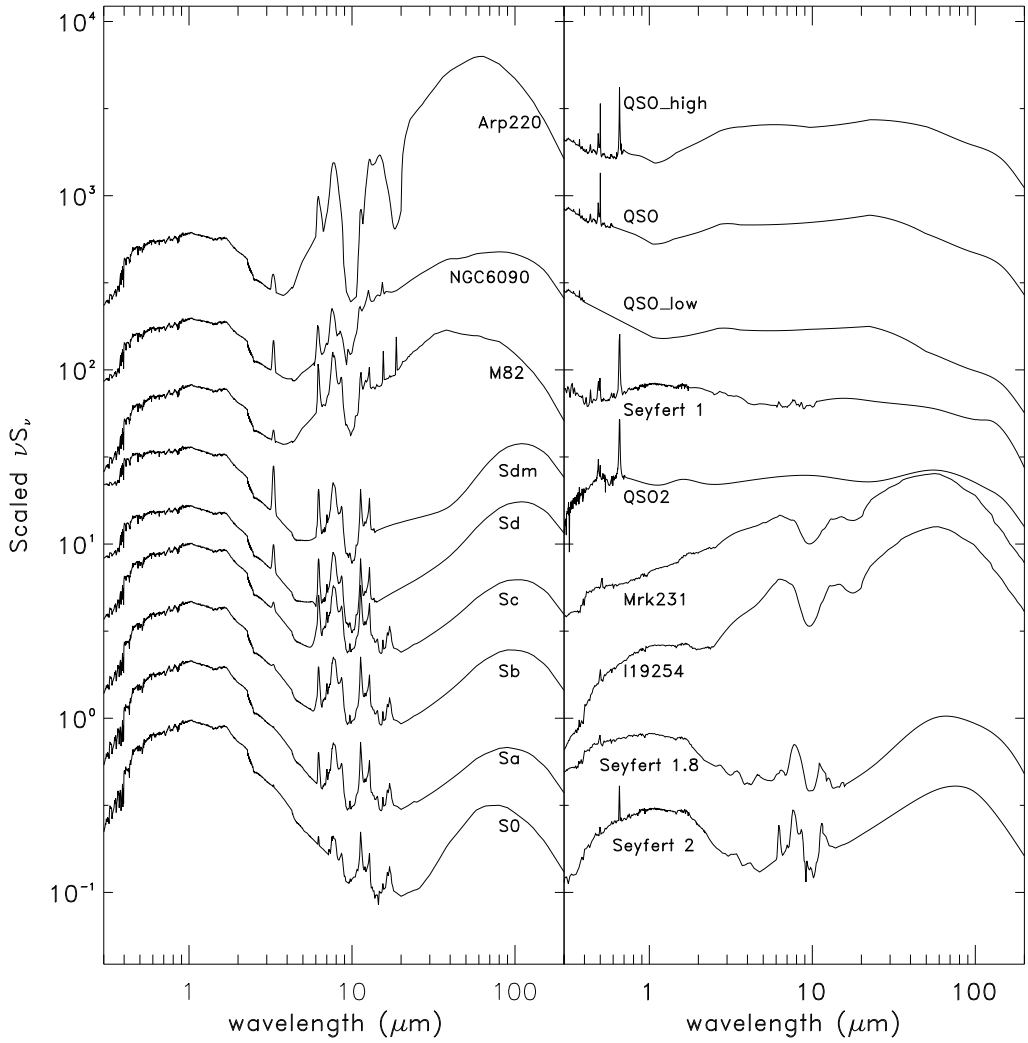

Figure 7.3: Example of template SEDs from Polletta et al. (2007) reproduced from Gruppioni et al. (2008).

in the MIPS/PACS range. In these cases, the PEP 100 and 160-μm flux densities were always higher by up to a factor of ~ 4 than the template at the same λ's. The authors constructed new templates with a rest-frame 0.1–15 μm spectrum similar to that of Polletta et al. (2007), but with a higher FIR bump, by averaging together (in λ-bins) the observed rest-frame SEDs (normalized to the K_s band) exhibiting an excess in the FIR and fitted by the same template. They also included to the library three new SB templates obtained by interpolating between the Sdm and the SB SED NGC6090 to fill the large gap existing in the library between spirals and SBs.

With this new complete template library we performed a SED-fitting to our sources. We carefully inspected the resulting SED fittings and we eliminated those

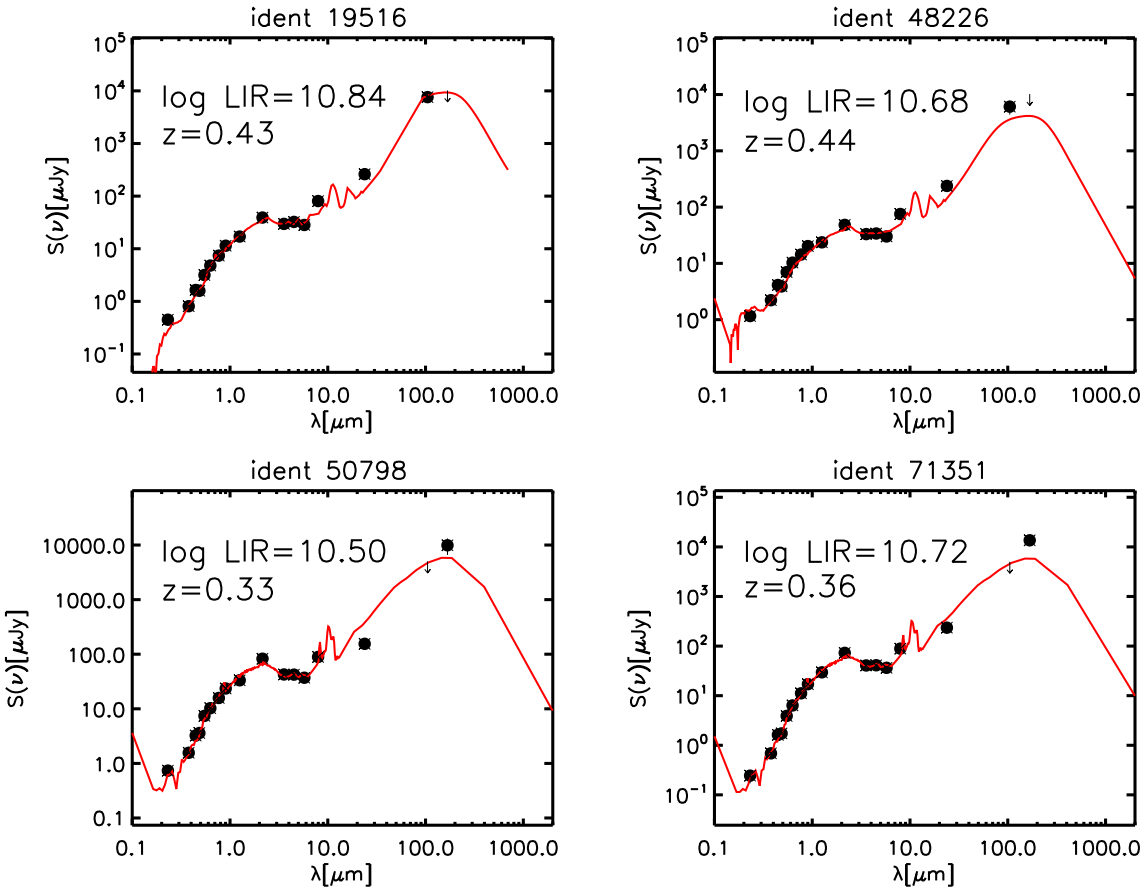

Figure 7.4: Example of sources with SED typical of a Seyfert galaxies. Black circles are the observed data while the red line is the best-f tting SED. Arrows represent the upper limits when the source is not detected in a particular band. Also shown in the plot are the redshift and the logL_{IR} of the sources.

sources with a typical Seyfert or QSO SED. In Fig. 7.4 we show 4 galaxies of our sample with best-f tting SED of Seyfert-2/Seyfert-1.8 galaxies. Although the Seyfert templates are dominated by star formation activity in the FIR, we choose to eliminate them from the sample to avoid any AGN contamination in our L_{IR} calculation.

7.1.4 Stellar Masses

The galaxy stellar masses were derived as explained in Sect. 5.4 (see also Ilbert et al. 2010). We used the *Lephare* code to f t our multi-wavelength data (from NUV to 5.8 μm) with a set of SED templates from Maraston (2005) with star formation

histories exponentially declining with time as $SFR \propto e^{-t/\tau}$. We used 9 different values of τ (0.1, 0.3, 1.0, 2.0, 3.0, 5.0, 10.0, 15.0 and 30.0 Gyr) with 221 steps in age. The metallicity assumed is solar. Dust extinction was applied using the Calzetti et al. (2000) extinction law. For this sample we allow a maximum E(B-V) value of 1.4. This value was chosen as the highest E(B-V) that the code was able to handle, given the large grid of parameters used in the SED-f tting. We imposed to the derived age of the galaxies to be less than the age of the Universe at that redshift and greater than 10^8 years. The latter requirement avoids having best f t SEDs with unrealistically high specif c star formation rates. As already stated (see Sect. 5.4.2), the Maraston (2005) models include an accurate treatment of the thermally pulsing asymptotic giant branch (TP-AGB) phase, which has a high impact on modeling the templates at ages in the range $0.3 \lesssim t \lesssim 2$ Gyr, where the fuel consumption in this phase is maximum, especially for the near-IR part of the spectrum.

7.2 Star Formation Rate Derivation

Our aim is to compare the SFR derived form the L_{IR} emission using Eq. 7.3 from Kennicutt (1998b) (K98 relation hereafter) with the SFR derived from the Hα emission line. In the next sections we explain how we calculated the SFR using both methods.

7.2.1 Star Formation Rate from the Infrared Luminosity

The SFR is a measure of the number of stars formed per unit time in a galaxy. A great part of the light emitted by young stars, which mostly reside within or behind clouds of gas and dust, is absorbed by dust and then re-emitted at longer wavelengths. Therefore, the SFR can be derived from the IR emission of the galaxies. One of the most commonly used method to derive SFR from the IR emission is to apply K98 relation, which links the SFR to the IR luminosity (L_{IR}) in the following way (already introduced in Sect. 3.3.4):

$$SFR(M_{\odot}yr^{-1}) = 4.5 \times 10^{-44} L_{IR}(ergs^{-1}) \tag{7.3}$$

However, this is a theoretical relation based on the starburst synthesis models of Leitherer & Heckman (1995b) obtained for a continuous burst, solar abundances

and a Salpeter (1955) IMF, assuming that young stars dominate the radiation f eld throughout the UV-visible and that the FIR luminosity measures the bolometric luminosity of the starburst. This physical situation holds in dense circumnuclear starbursts that power many IR-luminous galaxies. In the disk of normal galaxies or early type galaxies, the situation is much more complex as dust heating from the radiation f eld of older stars may be very important. Strictly speaking, as remarked by K98, the relation above applies only to starburst with ages less than 10^8 years while, for other cases, it would be probably better to rely on an empirical calibration of SFR/L_{IR}. We tested how well this simple SFR indicator worked for our sample by comparing it with the SFR derived from Hα.

To derive the L_{IR} value of each source we performed a SED-f tting using the *Le Phare* code (Arnouts et al. 2001 Ilbert et al. 2006), which separately f ts the stellar part of the spectrum with a stellar library and the IR part (at $\lambda > 7\mu$m) with IR libraries. To perform the SED-f tting we used 4 different infrared libraries (Dale et al. 2001, Chary & Elbaz 2001 and Lagache cold and Lagache SB from Lagache et al. 2004). In Fig. 7.5 and Fig. 7.6 we show the templates of two of the IR libraries used, the Chary & Elbaz (2001) and the Dale et al. (2001). We set the choice of the IR library as a free parameter, *i.e.* for each source, the code is allowed to try with all the possible templates from the 4 libraries and then chooses the best f tting template from all of them. This helps producing more accurate f tting to the data than choosing only one IR library.

For the far-IR data, the catalog errors are usually underestimated, thus producing very large χ^2 values. In the case of good f ts, the χ distributions should be consistent with a $\sigma \simeq 1$ Gaussian centered around 0. To enlarge the photometric errors of a reasonable quantity we run *Le Phare* on all the sources, obtaining a f rst "estimate" of the best-f tting SED. We then computed the distributions of the $(S_{object} - S_{template})_{band}/(\sigma_{object})_{band}$ values in each of the considered photometric band (where S_{object} and σ_{object} are the f ux density and the relative error of the source, and $S_{template}$ the f ux of the template in the considered band), iteratively increasing the photometric errors until we obtained a Gaussian distribution with $\sigma \simeq 1$. To clarify the process we show in Fig. 7.7 the χ distribution from 8 to 160 μm before enlarging the errors (black line) and after performing the iterative process (red line). The f nal distributions are well f tted by a Gaussian distribution with median and σ values also shown in the plot (blue line).

To perform the SED-f tting we f xed the redshift to the spectroscopic redshift (z_s) of

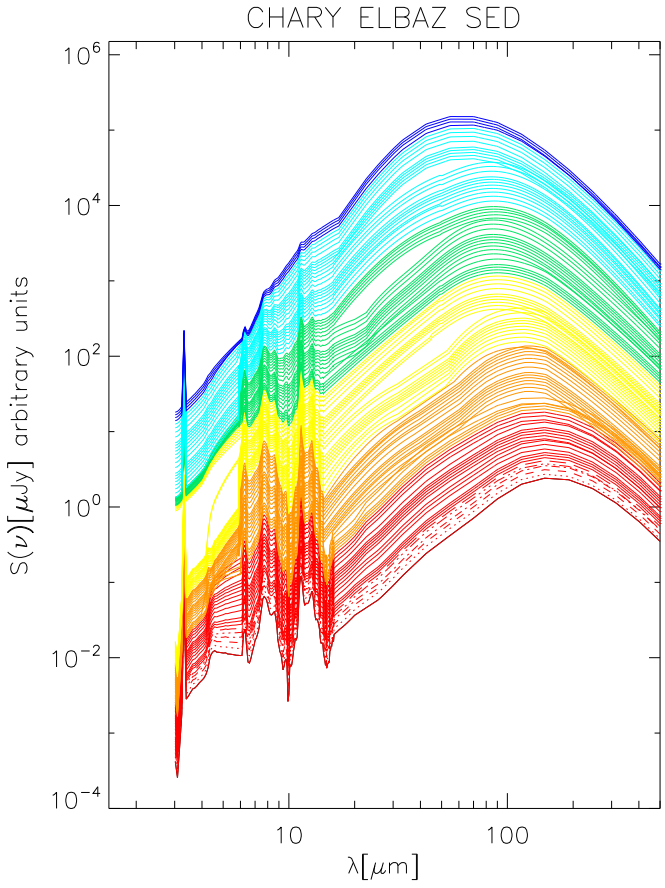

Figure 7.5: Chary & Elbaz (2001) IR template library.

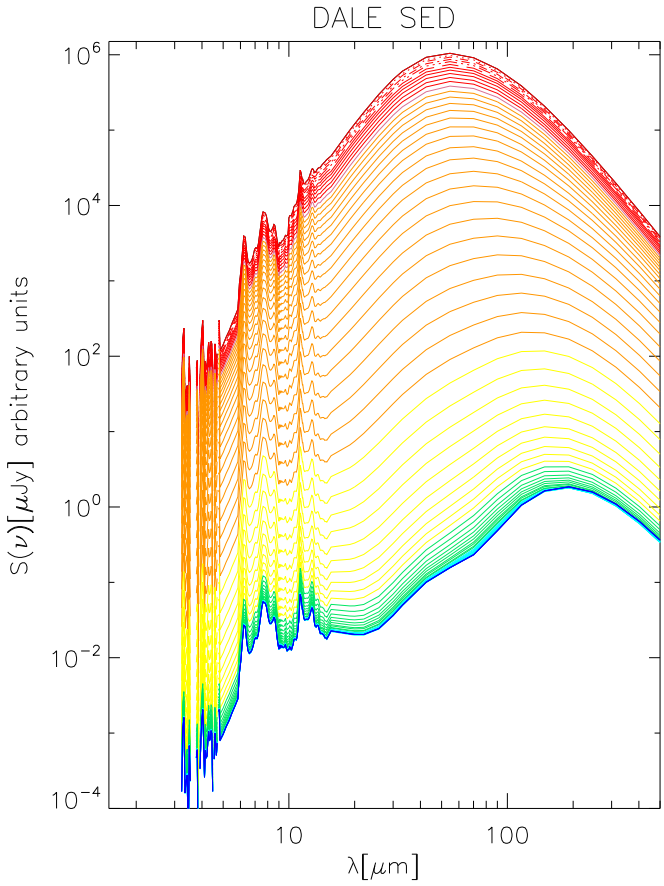

Figure 7.6: Dale et al. (2001) IR template library.

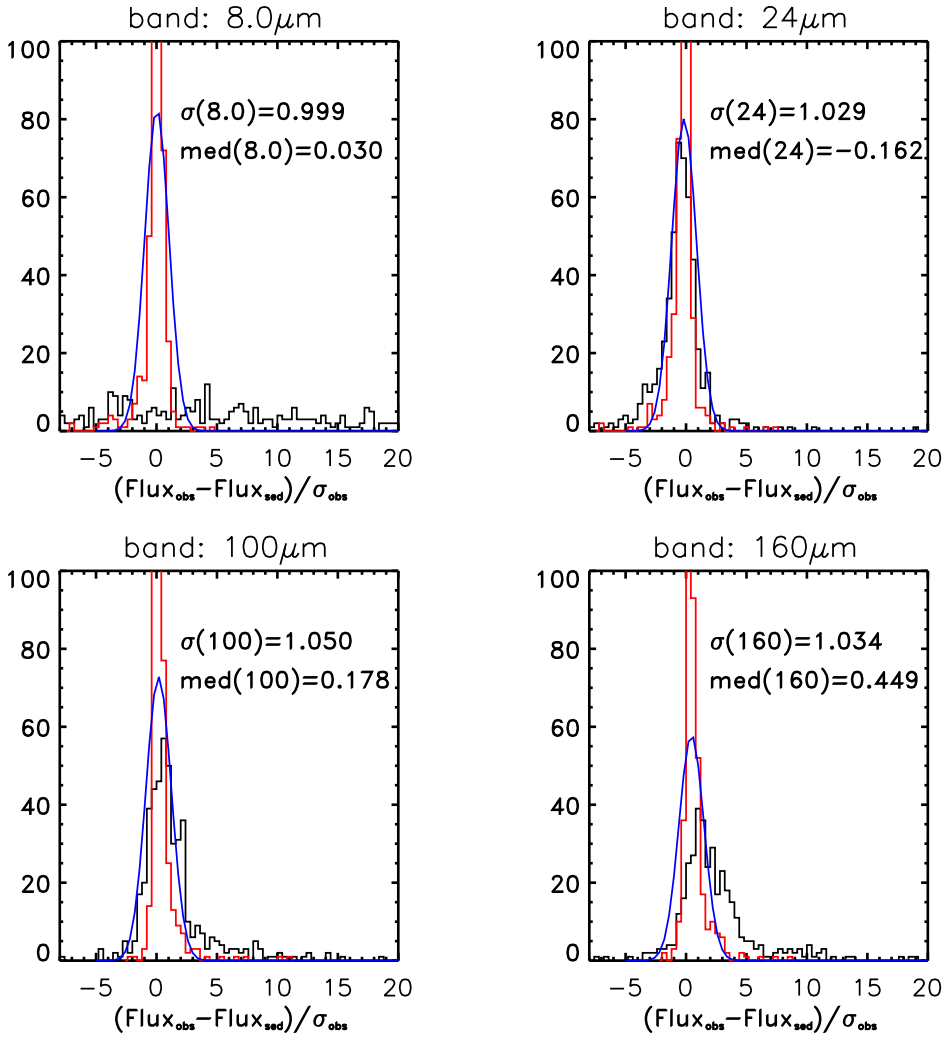

Figure 7.7: χ distribution in the 8, 24, 100 and 160 μm bands. The black line is the χ distribution obtained using original photometric errors. The red line is the distribution obtained after increasing the errors, while the blue line is the Gaussian fit to the new distribution.

each source and made use of the multi-wavelength data with the new photometric errors, including IRAC, Spitzer 24 μm and recent PEP Herschel data at 100 and 160 μm. The inclusion of these new data at large wavelengths, which sample the critical far-infrared peak of nearby galaxies, allows us to derive the L_{IR} without associated uncertainties due to extrapolation of the IR peak (see Elbaz et al. 2010, Nordon et al. 2011). We used the *Le Phare* code, which first performs a template-fitting procedure based on a simple χ^2 minimization; then it integrates the resulting best-fit spectra from 8 up to 1000 μm and directly gives the L_{IR} value as output. We estimate the 1σ uncertainty of the L_{IR} value as half the difference between $L_{IR,sup}$ and $L_{IR,inf}$, where $L_{IR,sup}$ and $L_{IR,inf}$ are the L_{IR} value for $\Delta\chi^2 = 1$. In Fig. 7.8 we show some examples of our SED-fittings. Black circles are the observed data, while the best SED fitting are the blue and the red lines for the stellar and starburst component, respectively.

7.2.2 Star Formation Rate from the Hα Emission Line

In this work we derived the SFR from the Hα emission line luminosity corrected from extinction [SFR(Hα) hereafter]. We used the conversion factor derived by Kennicutt et al. (1994) and Madau et al. (1998) to obtain our SFR from the Hα emission line:

$$SFR(M_{\odot}yr^{-1}) = 7.9 \times 10^{-42} L(H\alpha)(ergs^{-1}) \quad (7.4)$$

Hα emission line fluxes were measured using the automatic routine Platefit developed by Lamareille et al. (2009) to analyze the VLT-VIMOS (Very Large Telescope, VIsible Multi-Object Spectrograph) spectra. After removing a stellar component using Bruzual & Charlot (2003) models, Platefit VIMOS performs a simultaneous Gaussian fit of all emission lines using a Gaussian profile. The slits in the VIMOS masks have a width of 1 arcsec, therefore an aperture correction for slit losses is applied to each source. Each zCOSMOS spectrum is convolved with the ACSI(814) filter and then this derived magnitude is compared with the *I*-band magnitude of the GIM2D (Galaxy IMage 2D, an IRAF package) fits of Sargent et al. (2007). The difference between the two magnitudes gives the aperture correction for each spectrum. This correction assumes that the emission line fluxes and the *I*-band continuum suffer equal slit losses. In Fig. 7.9 we show ACS (10×10 arcsec^2) images of some galaxies from our sample. The spectrograph slits, 1 arcsec width, are also shown in the figure with the same orientation with which the spectra were

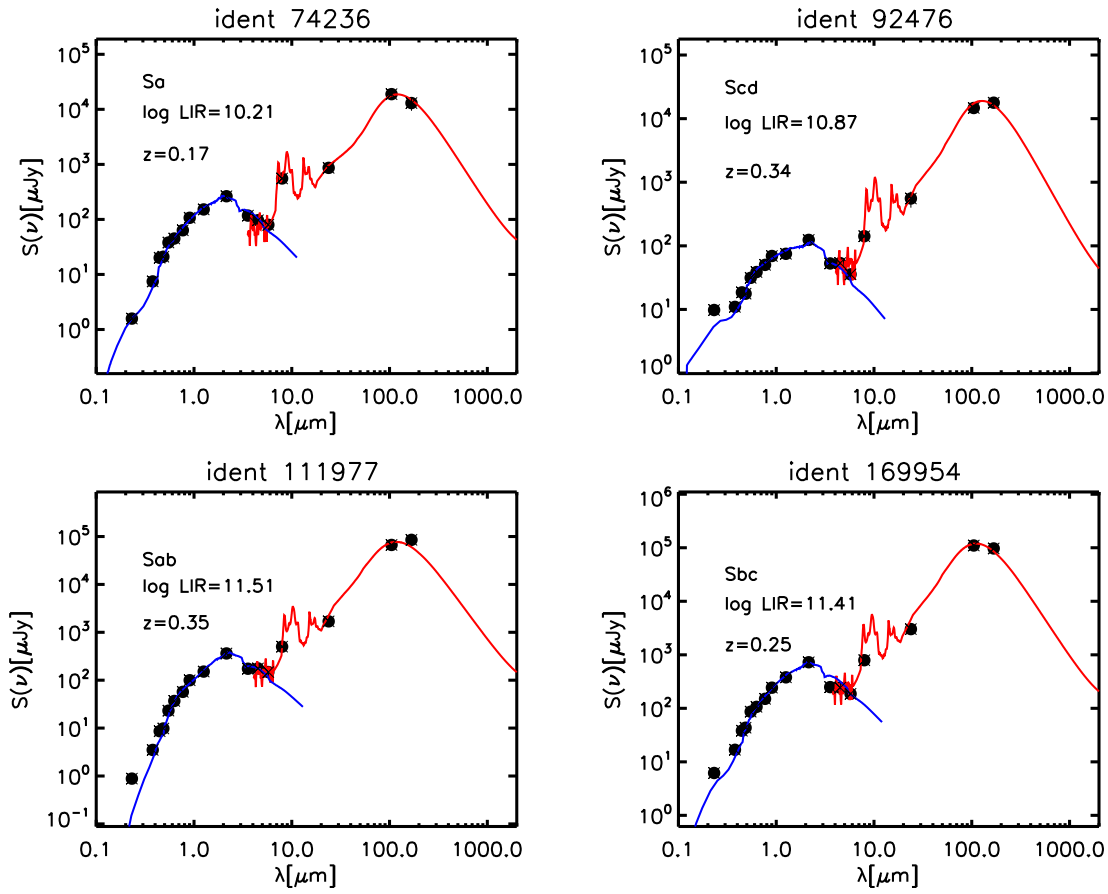

Figure 7.8: Example of SED-fitting for 4 sources. The observed SED of each source (black filled circles) is shown with the corresponding best-fit solution (blues solid line for the stellar part, red solid line for the IR), as well as the morphological type (see Sect. 7.4.5), the z_s and the derived L_{IR}.

taken. This ref ects the fact that, for the more extended galaxies, part of the emitted light from the galaxy does not enter the spectrograph, so we loose information from the most external parts of these galaxies.

Dust Extinction Correction

A major problem when deriving SFR(Hα) is the effect of dust extinction. Star formation normally takes place into dense regions in circumnuclear starburst, so a signif cant fraction of the emitted light from young stars is absorbed by the dust and re-emitted in the IR wavelengths. A method to measure the extinction is to compare the observed ratio of the Hα and Hβ emission lines with the theoretical value ($R_{th} = H\alpha/H\beta = 2.86$).

$$F_{corr}(H\alpha) = F_{obs}(H\alpha) \times 10^{0.4 \times A_\lambda} \tag{7.5}$$

$$A_\lambda = k(\lambda)E(B-V) \tag{7.6}$$

$$E(B-V) = A_V/R_V \tag{7.7}$$

$$\tag{7.8}$$

Following the Calzetti et al. (2000) extinction law, one can derive the A_V value by comparing the observed and the theoretical ratio of the Hα and Hβ emission lines as

$$A_V = 2.5 \times \frac{R_V \times log_{10}(R_{obs}/R_{th})}{(k1-k2)}, where$$

$$\begin{aligned} k1 &= 2.659 \times [-2.156 + (1.509/\lambda_1) - \\ &\quad (0.198/\lambda_2^2) + (0.011/\lambda_1^3)] + R_v \\ k2 &= 2.659 \times [-1.857 + (1.040/\lambda_2)] + R_v \\ \lambda_1 &= 4861.3\text{Å} \\ \lambda_2 &= 6562.8\text{Å} \\ R_v &= 4.05 \end{aligned} \tag{7.9}$$

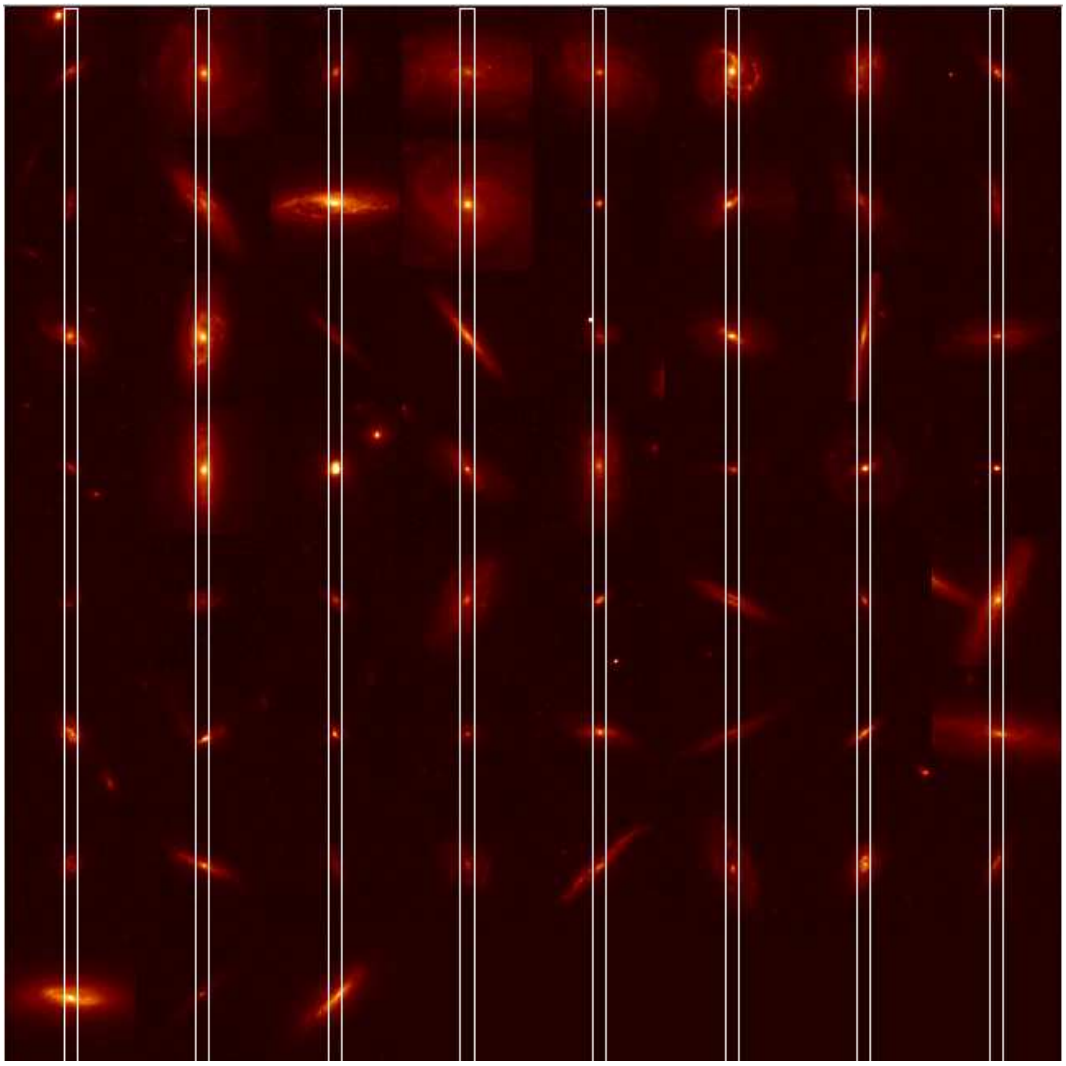

Figure 7.9: ACS (10×10 arcsec^2) images of some galaxies from our sample. The spectrograph slits, 1 arcsec width, are also shown in the f gure with the same orientation with which the spectra were taken.

Table 7.1: Number of sources in each L_{IR} bin.

log L_{IR} ($L_\odot$) < 10.5	10.5 < log L_{IR} ($L_\odot$) < 11.0	log L_{IR} ($L_\odot$) > 11.0
220	196	58

Making use of the spectra of our sources from the 20k survey we can measure the observed ratio between the Hα and Hβ emission lines and obtain the extinction values. However, the quality of the spectra is not high enough to individually measure the Hβ line for the whole sample. As the extinction usually correlates with the L_{IR}, we constructed median spectra for our sources, dividing them in 3 L_{IR} bins (see Table 7.1).

For each median spectrum we measured the Hα and Hβ fluxes using the IRAF software, after subtracting the stellar component making use of extincted Bruzual & Charlot (2003) models. Fig. 7.10 shows the median spectra obtained for the lowest L_{IR} bin (black line) before subtracting the stellar continuum (red line) and once the continuum has been subtracted (blue line). Once the stellar component is subtracted from the observed spectra, the emission lines can be measured without the contamination of the stellar absorption. Fig. 7.11 shows the median spectra of our sources after performing the continuum subtraction, as well as the values of the observed ratio between Hα and Hβ emission lines, A_V and $E(B-V)$. As expected, the extinction increases with L_{IR}, from $E(B-V) = 0.28$ for log $L_{IR} < 10.5$ to $E(B-V) = 0.62$ from log $L_{IR} > 11.0$. We derive the Hα luminosities using the measured spectroscopic redshift z_s of each source, and then we obtain the SFR(Hα) following Eq. 7.4.

As a comparison with respect to the quality of the median spectra we show in Figs. 7.12, 7.13 and 7.14 three typical spectra of three individual galaxies from the different L_{IR} bins (from lower to highest L_{IR}). Note the noise associated to the spectra, which makes it very complicated to accurately measure the emission lines, specially the weak ones, such as Hβ. Therefore we need to construct median spectra to have a more accurate measure of the extinction, even though if it is not measured for every single object.

Once we have derived median dust extinction values for the 3 L_{IR} bins considered, we correct each single galaxy from extinction using the median extinction value which corresponds to the L_{IR} bin to which that particular galaxy belongs. Therefore, in the estimation of the SFR(Hα), now our main source of error is probably the use

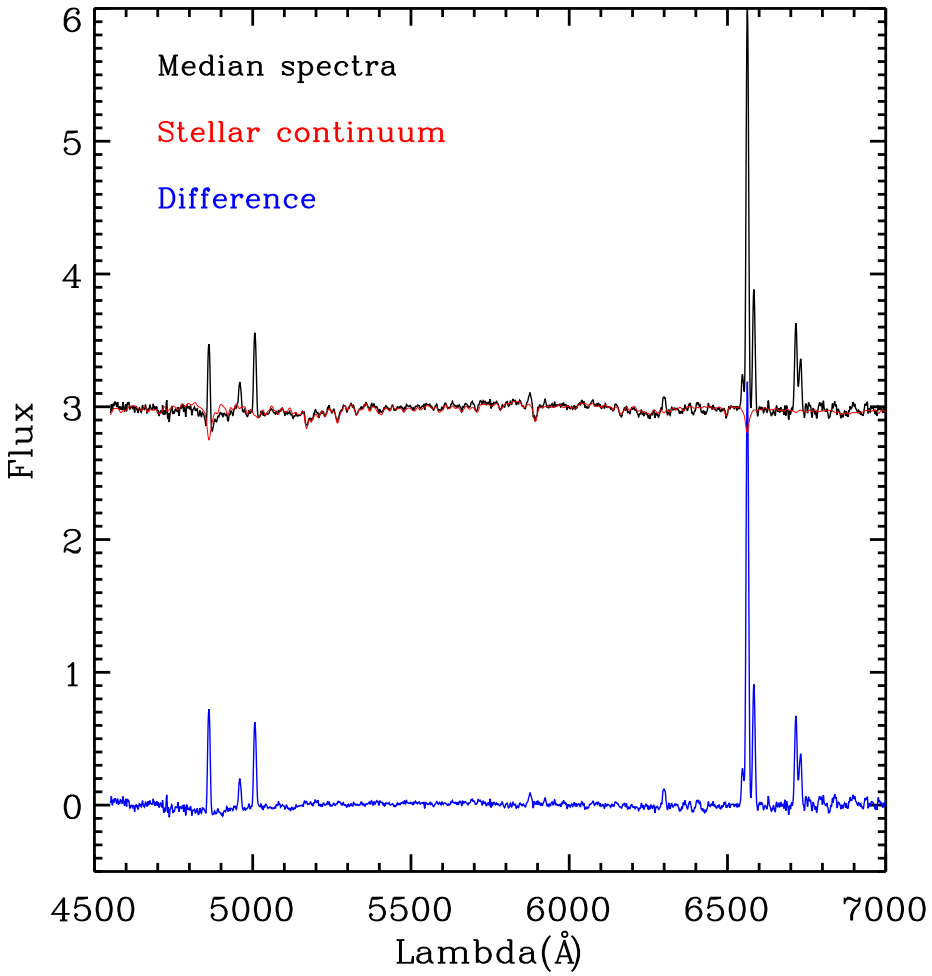

Figure 7.10: Median spectra for the lowest L_{IR} bin (log L_{IR} < 10.5). Black line is the median spectra before subtracting the stellar component (red), while the spectra obtained when removing the stellar continuum is plotted in blue.

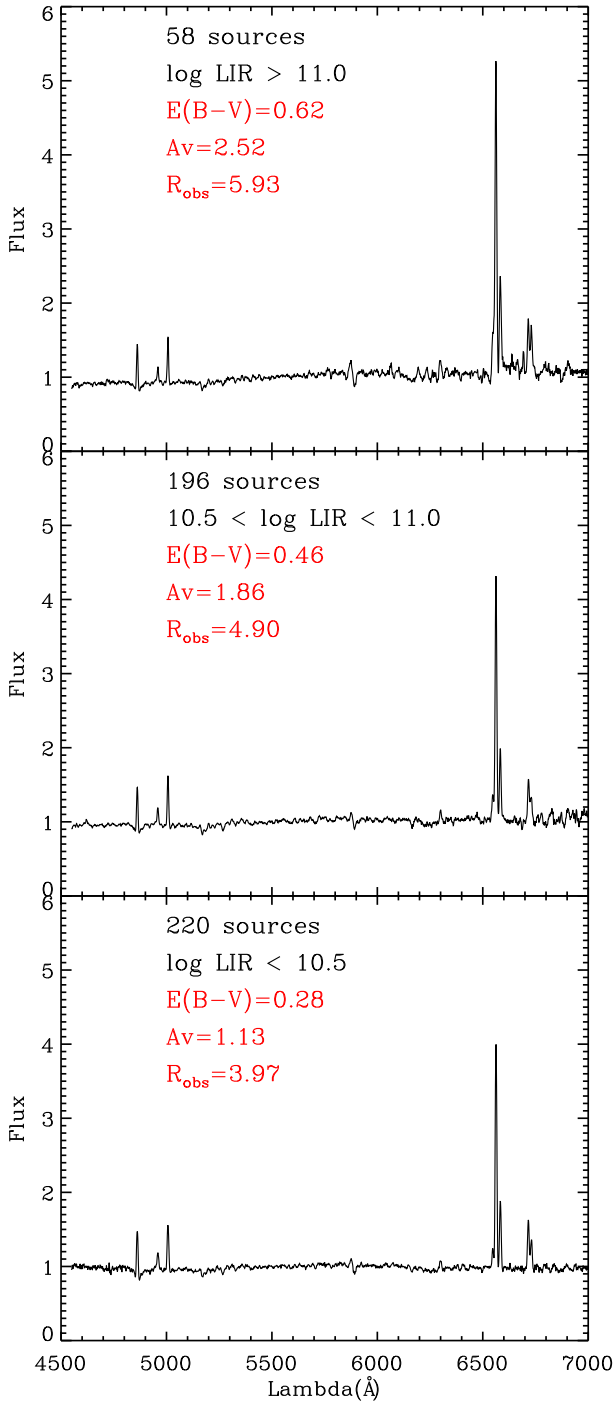

Figure 7.11: Median spectra for 3 L_{IR} bins, with increasing L_{IR} from bottom to top. Also shown the values of R_{obs}, A_v and $E(B-V)$, as well as the number of sources in each L_{IR} bin.

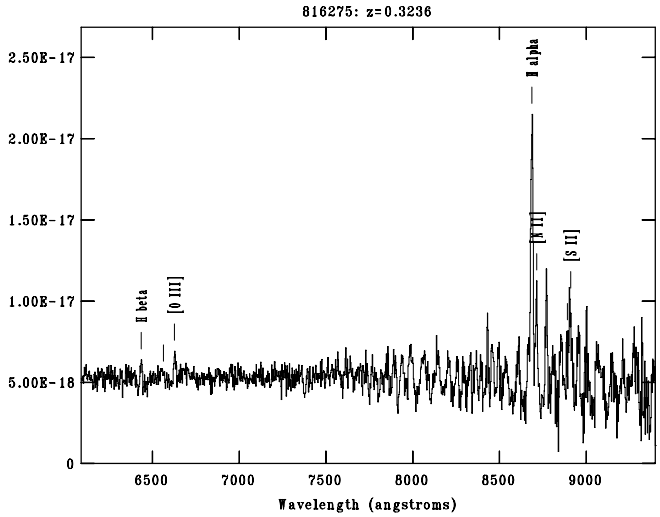

Figure 7.12: Typical spectra of a galaxy with log L_{IR} < 10.5 $L_{\odot}$. The main emission lines are indicated in the plot (Hα, Hβ and the forbidden emission lines, [NII], [OIII] and [SII]). The quality of the spectra does not allow an accurate measure of the Hβ line.

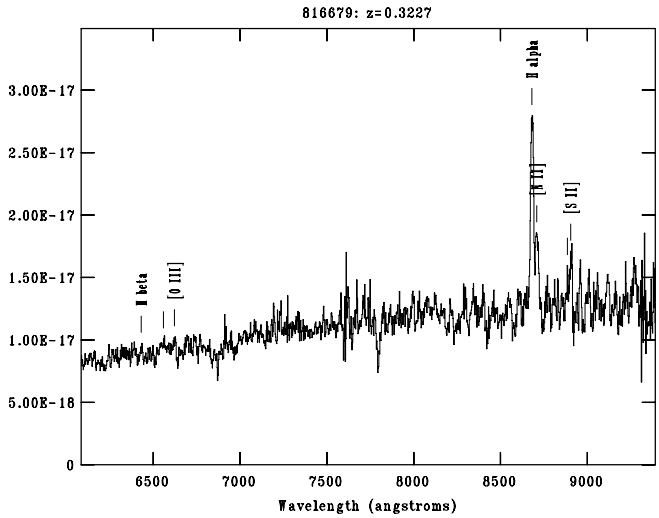

Figure 7.13: Same as in Fig. 7.12 for a galaxy with 10.5 < log L_{IR} ($L_{\odot}$) < 11.0

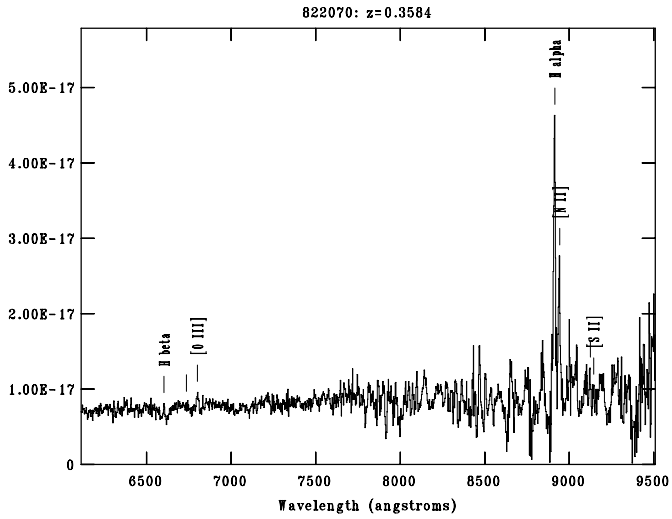

Figure 7.14: Same as in Fig. 7.12 for a galaxy with log $L_{IR} > 11.0\ L_{\odot}$

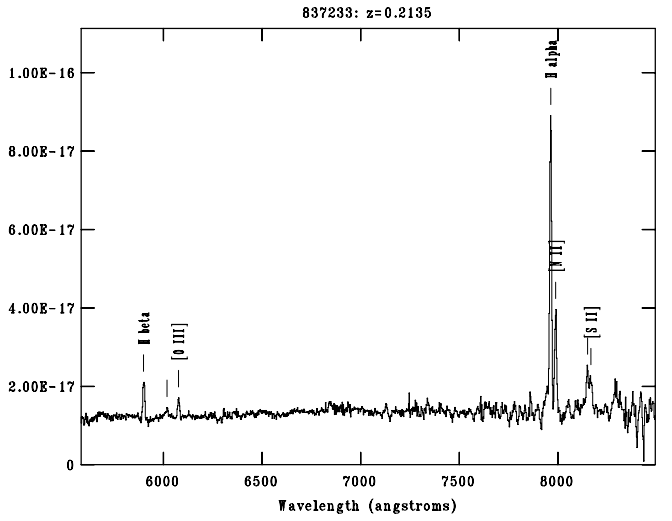

Figure 7.15: Spectra of one of the 31 sources with good quality that allowed to accurately measure the emission spectral lines. The extinction value obtained is $A_V = 3.28$.

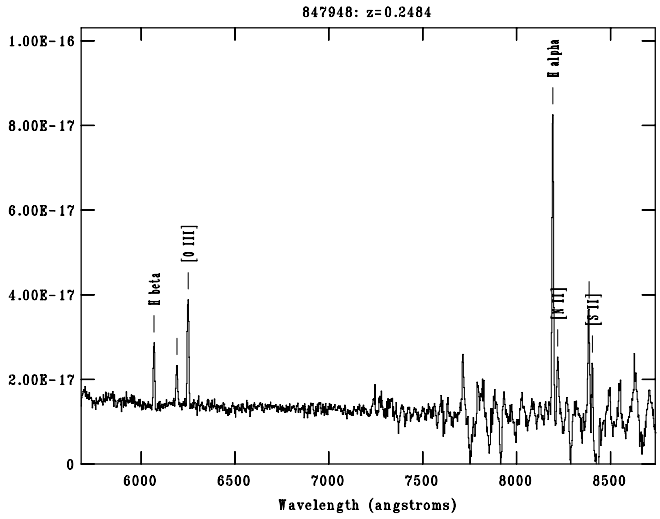

Figure 7.16: Same as in Fig. 7.15 for a galaxy with low extinction (A_V = 0.94).

of an average dust extinction correction. To test the effect of adopting an average $E(B-V)$ value in L_{IR} bins, we visually inspected the spectra of our sources and we selected a small sub-sample of 31 sources with high S/N continuum in both the Hα and Hβ spectral ranges, so that we can rely on the measured value of the Hα/Hβ ratio for each source ($R_{obs,ind}$). We then constructed a median spectrum for these 31 sources and derived the median observed ratio ($R_{obs,med}$) as explained before. We show two examples of these 31 galaxies with high S/N continuum in the emission lines spectral ranges (Figs. 7.15 and 7.16 for a galaxy with high and low extinction values, respectively.). It can be observed the difference between the quality of the emission lines in these spectra selected to test the effect of using median extinction values instead of single values with respect to the noise associated to the emission lines of the typical spectra (Figs. 7.12, 7.13, 7.14).

In Fig. 7.17 we show the difference between the E(B-V) value measured for each of the 31 sources of this control sample and the E(B-V) value of the median spectra for these 31 sources. The dispersion is $\sigma = 0.20$ and there is no signif cant offset ($\langle\Delta(E(B-V)\rangle = 0.04$). This small offset conf rms that, when using median extinctions instead of individually measured extinctions, we are not introducing any systematic bias but only increasing the dispersion of the data. We interpret the value $\sigma = 0.20$ as the E(B-V) uncertainty that we introduce in the SFR(Hα) when using a median extinction instead of an individual extinction for each source. We take into account this dispersion when deriving the SFR(Hα) errors.

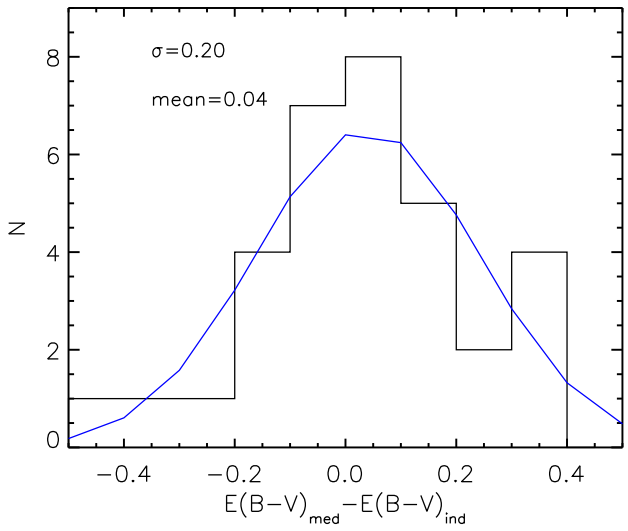

Figure 7.17: Difference between the E(B-V) value derived from the median spectrum and the E(B-V) value measured for each source for a control sample of high S/N sources both in Hα and Hβ emission lines. The $\Delta(E(B-V))$ values are consistent with a Gaussian distribution with $\sigma = 0.20$. We assume this dispersion to be the error in E(B-V) that we introduce when using a median extinction instead of an individual extinction.

Brinchmann 2004 Recipes

In the previous section we have derived our SFR(Hα) by simply multiplying the $L_{H\alpha}$ value by a constant (Eq. 7.4). However, recent works have demonstrated that this constant, commonly known as eff ciency and expressed as $\eta_{H\alpha} = L_{H\alpha}/SFR$ ($\eta^0_{H\alpha} = L_{H\alpha,corr}/SFR$ is the eff ciency between SFR and $L_{H\alpha}$ corrected from dust extinction), does change with some galaxy properties and, in particular, with stellar mass. Following Brinchmann et al. (2004) [B04, hereafter] we also derived our SFR(Hα) by using eff ciency values which depend on the galaxy stellar mass. These eff ciency values were taken from the values derived in B04 (Fig. 7.18 in this work, Fig. 7 in B04). For each source of a given mass, we interpolated the $\eta^0_{H\alpha}$ values from B04 and used the resulting $\eta^0_{H\alpha}$ values to derive the SFR from the Hα luminosity. We will call the SFR derived in this way as SFR(Hα, B04). In any case, when using $\eta^0_{H\alpha}$ values, an extinction correction must be applied to the observed Hα luminosity line. We applied the median extinction values derived in L_{IR} bins as explained above.

To avoid the extinction problem we made use of another result from B04. In Fig. 6 from B04 (Fig. 7.19 in this work) the likelihood distribution of the dust

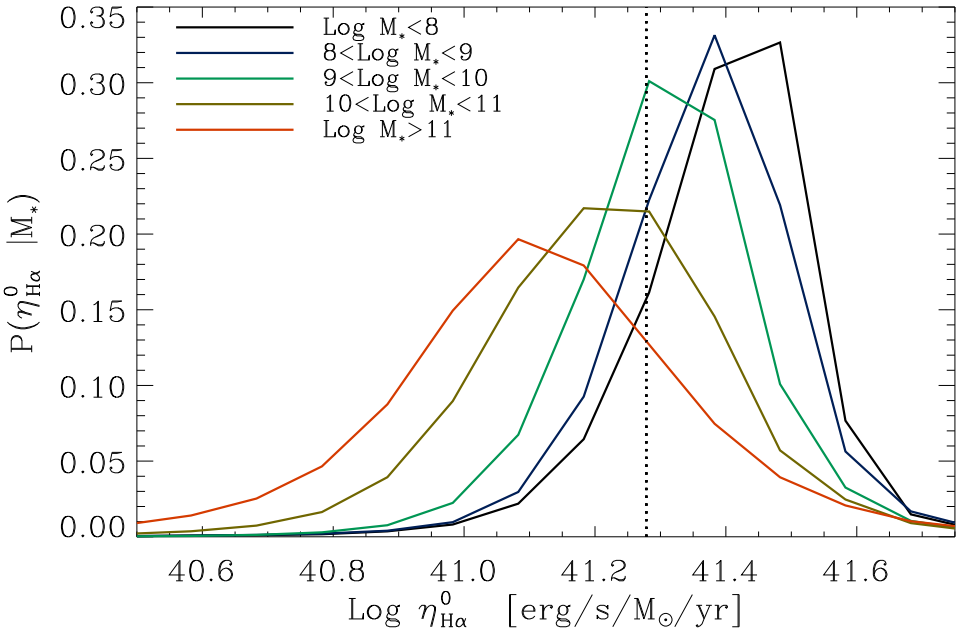

Figure 7.18: The likelihood distribution of the conversion factor between un-extincted Hα luminosity and the SFR for different mass values. Reproduced from B04.

attenuation as a function of the stellar mass is shown. As for the $\eta^0_{H\alpha}$ values, we used the $A_{H\alpha}$ value corresponding to the mass of each galaxy. Then, we corrected our Hα luminosities from extinction using the $A_{H\alpha}$ calculated values and then transformed the luminosity into SFR by using the $\eta^0_{H\alpha}$ derived above for each galaxy. We will call the SFR derived in this way as SFR(Hα, B04, ext).

7.3 Star Formation Rate Comparison

In this section we aim to compare the different values of the SFR from IR or Hα luminosities using the recipes explained in Sects. 7.2.1 and 7.2.2. In Fig. 7.20 we compare SFR(L_{IR}) with SFR(Hα), where SFR(Hα) is obtained from the Hα emission line using the simple linear conversion from Eq. 7.4. The blue line is the one to one relation, while the red line is the best f t to our data. For clarity of the f gure we did not include the errors for each source, but show the median error on SFR(L_{IR}) and SFR(Hα) for each L_{IR} bin. Notice that, while the errors on SFR(Hα) are almost constant in the three L_{IR} bins, the errors on SFR(L_{IR}) are larger for lower L_{IR} values. We have performed a linear f t taking into account both

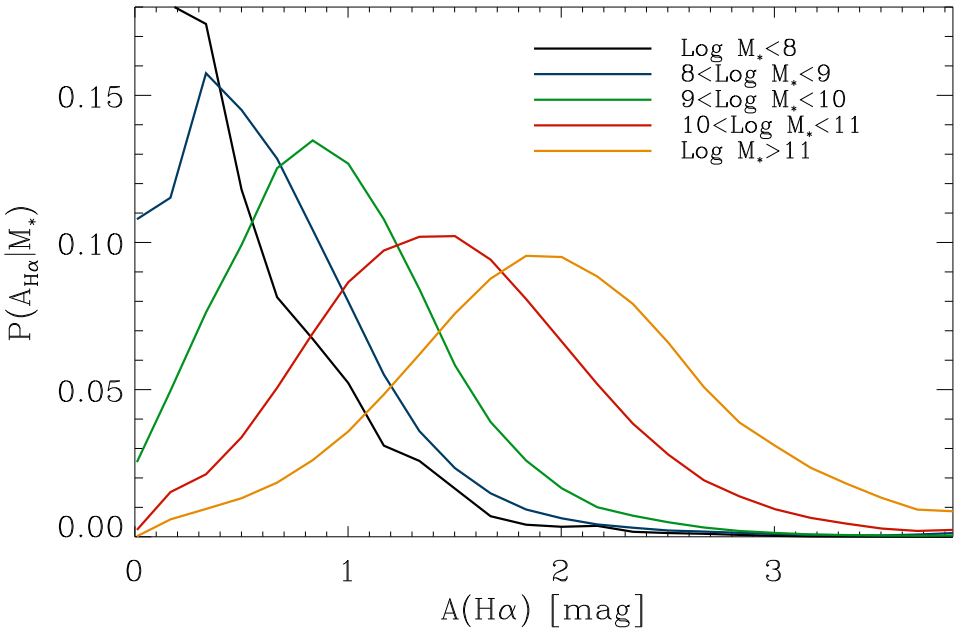

Figure 7.19: The likelihood distribution of the dust attenuation as a function of stellar mass. Reproduced from B04.

the errors in SFR(L_{IR}) and in SFR(Hα), which include the uncertainty introduced when using median extinctions (as explained in Sect. 7.2.2). The slope of our relation is $m = 1.11 \pm 0.04$, consistent at 3σ with the one to one relation ($m = 1.0$). Also the normalizations of the two relations are well consistent with each other. It is interesting to notice the relatively small dispersion of the data ($\sigma = 0.31$), comparable with the uncertainties derived for the SFR(Hα) (with a mean error $\sim$ 0.30). Considering the wide range of SFRs studied (about three orders of magnitude) and the systematic errors that could affect our sample, we conf rm that both SFRs estimates are in a very good agreement, even if they are based on very simple recipes that do not take into account the galaxy intrinsic properties, but are a mere transformation from luminosity to SFR.

In Figs. 7.21 and 7.22 we show an analog to the Fig. 7.20 now showing in the *x* axis the SFR values obtained following the B04 recipes. In Fig. 7.21 the SFR values are SFR(Hα, B04), *i.e.* they are derived using the mass dependent eff ciency, with $L_{H\alpha}$ values corrected from extinction using the median E(B-V) values in each L_{IR} bin. In Fig. 7.21, instead, the SFR values derived from the Hα luminosities are the SFR(Hα, B04, ext), *i.e.* they are derived using both the mass dependent eff ciency

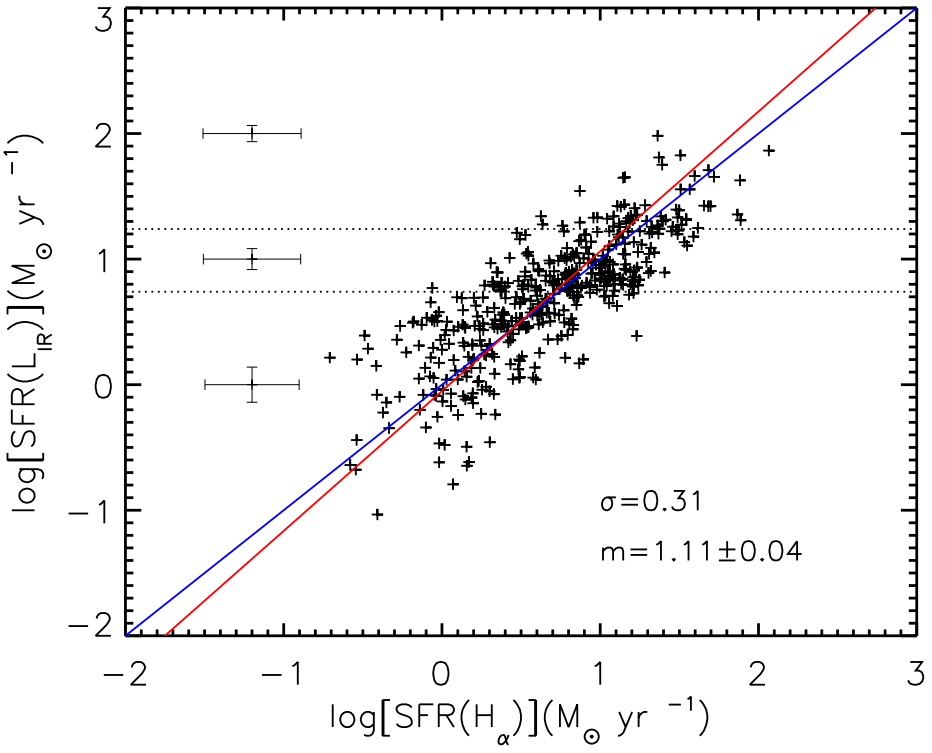

Figure 7.20: SFR(L_{IR}) vs SFR(Hα). The blue line represents the one to one relation, while the red line is the best-fit to our data. Horizontal dotted lines represent the limits of the bins in L_{IR} converted in SFR(L_{IR}). Also shown in the plot the slope of the best fit ($m = 1.11 \pm 0.04$) and the dispersion of the relation ($\sigma = 0.31$). Median errors on SFR(L_{IR}) and SFR(Hα) for each L_{IR} bin are shown in each L_{IR} bin.

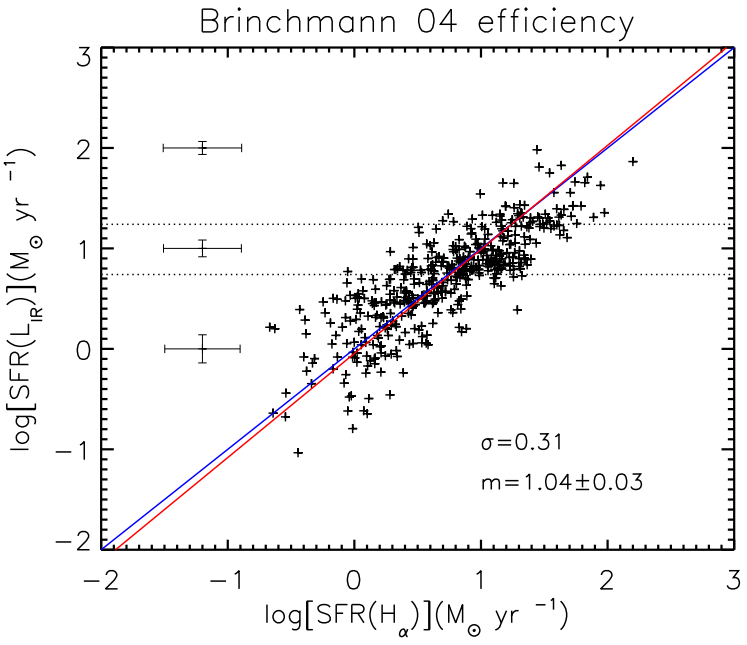

Figure 7.21: SFR(L_{IR}) vs SFR(Hα, B04). Colors as in Fig. 7.20.

and dust attenuation values. In this case, we assume a $\sigma = 0.20$ uncertainty in the dust E(B-V) values, as derived from the shape of the Gaussians of the likelihood distribution of the dust extinction (from Fig. 7.19).

The agreement between the SFR(L_{IR}) and the SFR(Hα, B04) is excellent, with a slope 1.04 ± 0.03, *i.e.* consistent within $\sim 1\sigma$ with the one to one relation. The dispersion value $\sigma = 0.31$ is almost identical to the one we obtain when using the more simple linear conversion (Eq. 7.4), confirming the good agreement between SFR indicators. When including the mass dependent extinction, however, the slope fitting the data increases up to 1.26 ± 0.05, while the dispersion remains very similar to the one obtained for the previous methods ($\sigma = 0.32$). The increment of the slope must be due to the introduction of this mass dependent dust attenuation, meaning that, at high L_{IR}, the mass dependent dust extinction correction is smaller than that derived from the median spectra, and the other way round at low L_{IR}.

We have considered the possible effect of a selection of the sample in the far-IR bands when studying the SFR estimates comparison. For the sources with a detected Hα flux, but not detected in the far-IR, we have derived the SFR from the Hα luminosity and then transformed this into L_{IR} assuming that the K98 relation is correct (inverse of Eq. 7.3). There is a quite robust dependence between L_{IR} and 100 and 160 μm fluxes for a given redshift. Therefore, knowing the redshift and

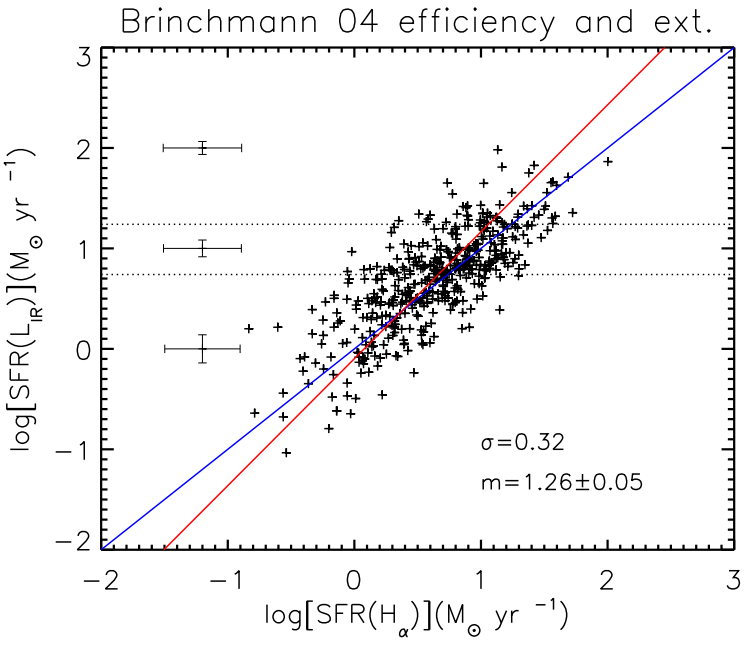

Figure 7.22: SFR(L_{IR}) vs SFR(Hα, B04, ext). Colors as in Fig. 7.20.

the L_{IR}, we have approximately calculated the PEP fluxes that these sources should have if they would follow the K98 relation. 99% of the sources detected in Hα but not detected in the far-IR have estimated PEP fluxes lower than the PEP detection limit, *i.e.* they are consistent with following the K98 relation and being undetected in the far-IR.

We have also studied a possible aperture correction effect. The IR fluxes at 100 and 160 μm from Herschel are integrated fluxes over the whole galaxy due to the large PSF. Instead, as explained in Sect. 7.2.2, the Hα is measured with a slit of 1 arcsec width and then aperture corrected. This correction assumes that the Hα flux is homogeneous in the whole galaxy. However we know that galaxies have internal structures, specially affecting the star forming regions where the Hα emission is observed. Larger galaxies should be more affected by aperture correction as the observed Hα flux is measured in a smaller part of the galaxy, while for small galaxies almost all the light enters into the slit. We have tested the aperture correction effect by comparing the difference between SFR(L_{IR}) and SFR(Hα) with the sizes of the galaxies. We did not see any systematic effect, *i.e.* the Δ(SFR) did not depend on the galaxy sizes. We therefore conclude that the aperture correction does not systematically affect the slope of the SFR(L_{IR})-SFR(Hα) relation.

7.4 Star Formation Rate Dependences

7.4.1 Redshift

We have seen that the SFR estimates from Hα luminosity and L_{IR} agree very well with each other when considering the whole sample of galaxies. In this section we aim to detect if there are intrinsic properties of the galaxies that could affect the SFR(Hα)-SFR(L_{IR}) relation. In Fig. 7.23 (upper panel) we show the SFR(L_{IR}) vs SFR(Hα) for different redshifts, where the color code is explained in the plot. To better appreciate the effect of z, we plot in the lower panel the ratio between SFR(L_{IR}) and SFR(Hα) versus z [$\Delta(SFR)$]. The blue line represents the best fit to the data with a fourth order polynomial, while the red dots are the running mean of the $\Delta(SFR)$ each 20 values of z. There seems to be no strong dependence on the relation with the redshift of each source, but a random scatter around the redshift zero point. We studied the effect of redshift when using B04 recipes. In Fig. 7.24 we plot the same data as in the lower panel of Fig. 7.23 but now the SFRs have been derived using the B04 recipies. In the upper panel we show the SFR(Hα, B04), *i.e.* the SFR derived from the Hα emission line when using different $\eta^0_{H\alpha}$ values and correcting $L_{H\alpha}$ from extinction using the median $E(B-V)$ values obtained from the median spectrum in each L_{IR} bin. In the lower panel we show SFR(Hα, B04, ext.) where, in addition to different efficiency values, we also use the $A_{H\alpha}$ extinctions calculated for different masses. No much difference is observed when deriving the SFR with these three different methods. We conclude that SFR(L_{IR})-SFR(Hα) relation is not significantly affected by the redshift of the galaxies, at least up to $z = 0.46$, which is the maximum considered z of our sample.

Note, however, the slight increase on the SFR(L_{IR})/SFR(Hα, B04, ext.) ratio at high z (lower panel Fig. 7.24) with respect to the ratio obtained for the two other methods [SFR(Hα) and SFR(Hα, B04)]. In a flux limited sample, as it is the case, high L_{IR} values are related to high redshifts. Therefore, the over-estimation of the SFR(L_{IR}) with respect to the SFR(Hα, B04, ext.) at high z is in agreement with the increase of the slope in Fig. 7.22.

7.4.2 Mass

In Fig. 7.25 we show the same as in Fig. 7.23, but now the color code represents different mass bins, where the mass has been derived by means of a SED-fitting

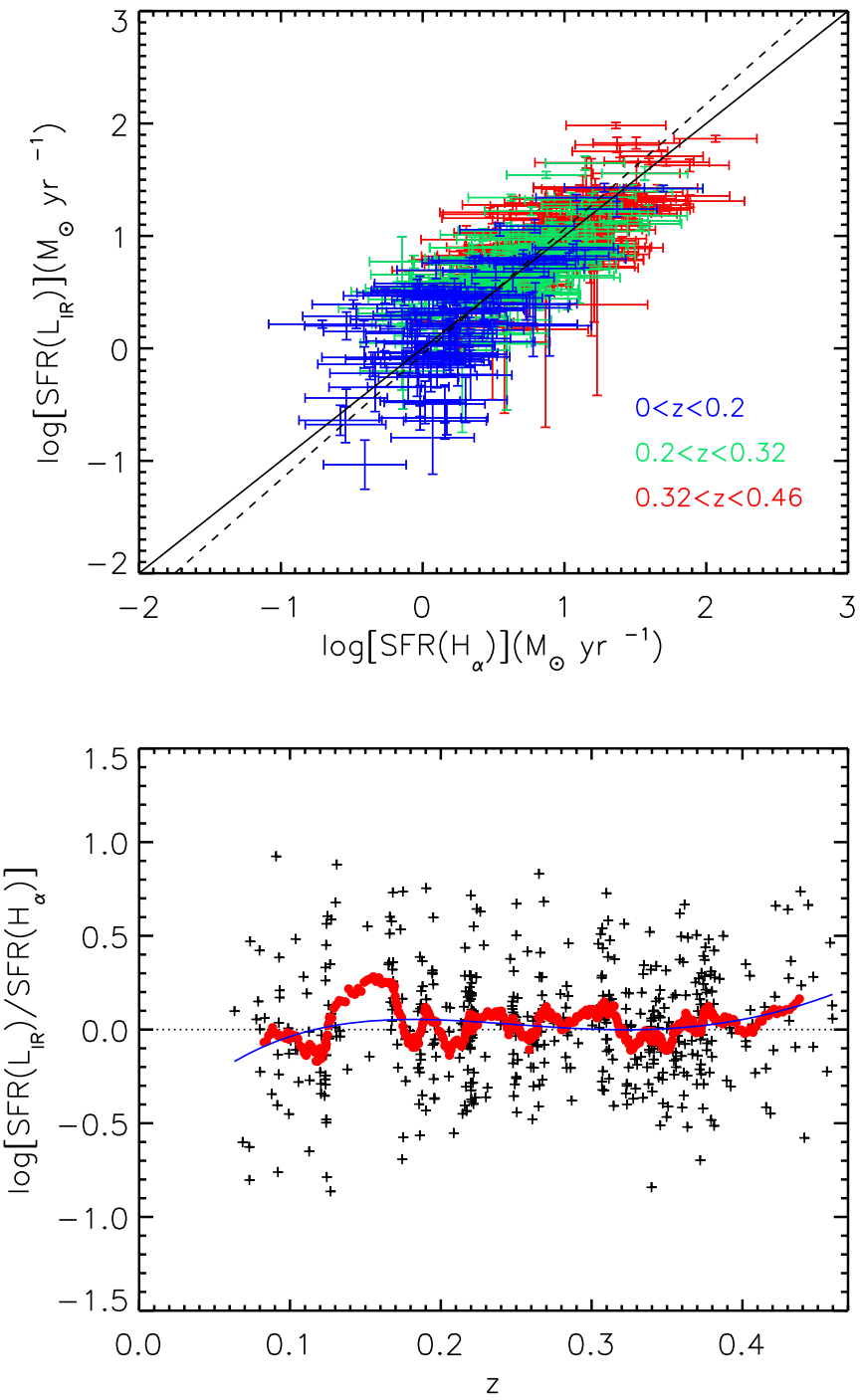

Figure 7.23: Upper panel: SFR(L_{IR}) vs SFR(Hα) for different redshift bins. Dashed and continuous lines represent the best f t to our data and the one to one relation, respectively. Lower panel: log[SFR(L_{IR})/SFR(Hα)](≡ $\Delta(SFR)$) versus z. The blue line is the best f t to our data. Red dots are the running mean of $\Delta(SFR)$.

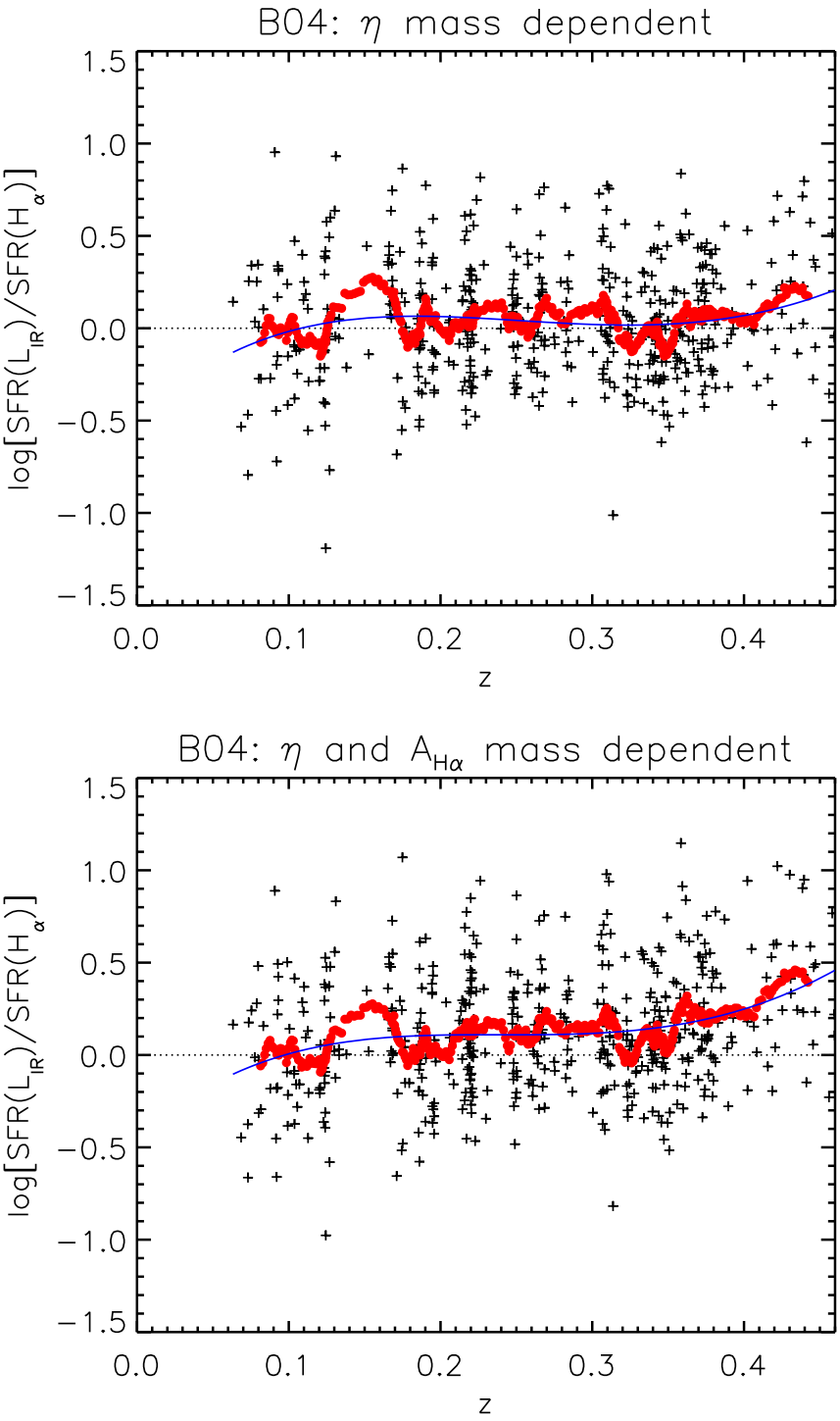

Figure 7.24: Same as in lower panel of Fig. 7.23 for values of SFR(Hα, B04) (upper panel) and SFR(Hα, B04, ext.) (lower panel).

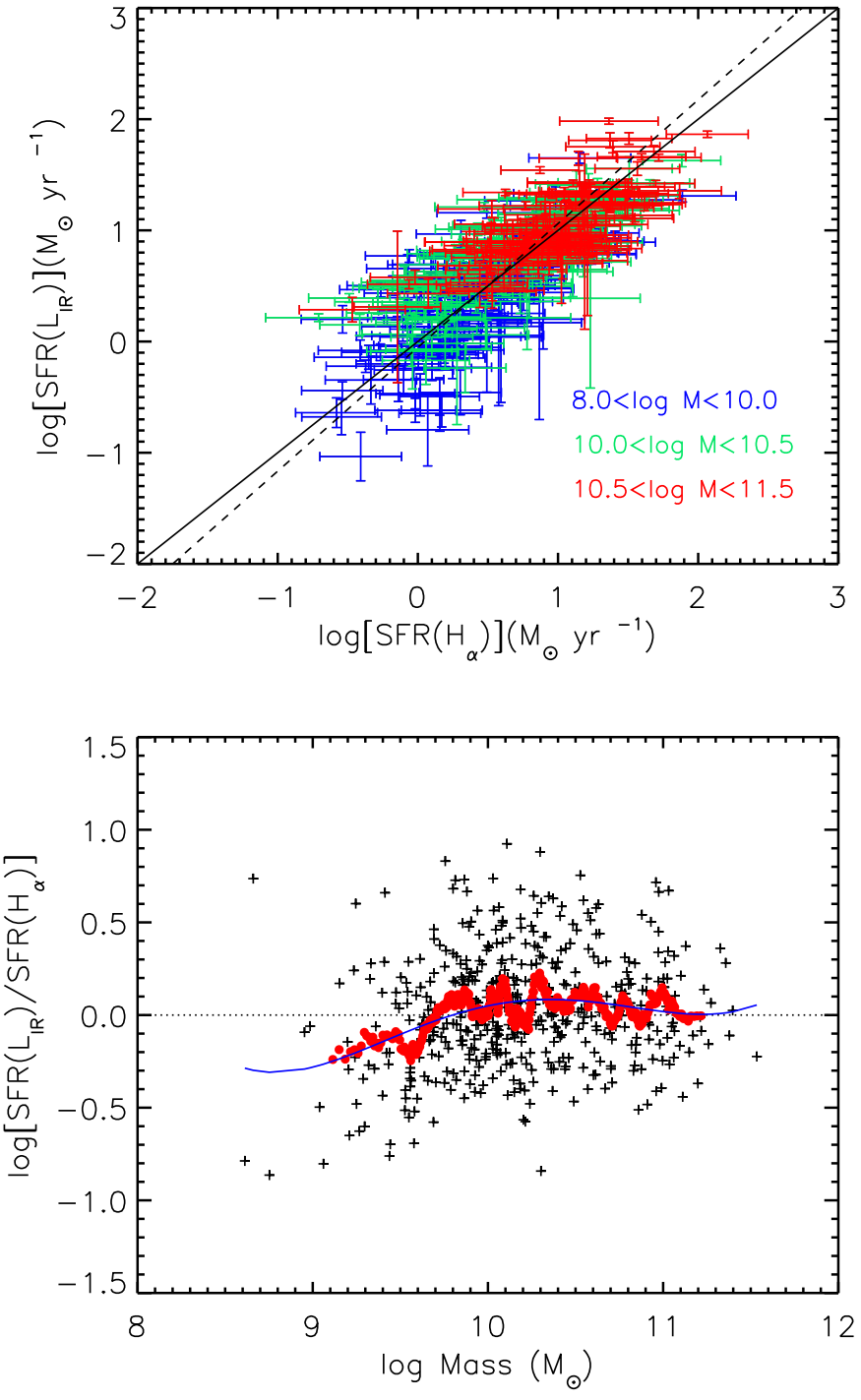

Figure 7.25: Upper panel: Same as in Fig. 7.23 but here colors represent different mass bins. Lower panel: log [SFR(Hα)/log SFR(L_{IR})] versus log (Mass). Blue line and red dots as in Fig. 7.23.

as explained in Sect. 7.1.4. Also shown in the lower panel of this f gure the ratio between SFR(L_{IR}) and SFR(Hα), where the SFR(Hα) is derived using the simple conversion factor from Eq. 7.4, versus the logarithm of the mass. There is a possible trend with mass, in the sense that for low mass sources the SFR(L_{IR}) seems to be under-estimated with respect to the SFR(Hα). We performed the f t to the data including only sources with $logM > 9.3M_{\odot}$, to make sure that the trend that we observe is not due to a few low mass sources, f nding a very similar f t. It is beyond the scope of this work to give a clear explanation of the observed disagreement at low masses. However, we would like to cite as a possible explanation a recent study by Weisz et al. (2011) who, making use Star Formation Histories (SFH) models and observations, state that more massive galaxies are best characterized by nearly constant SFHs than low mass galaxies. Considering that the K98 relation is calibrated using continuous star formation models, we could easily understand why the relation works better for high mass systems.

In Fig. 7.26 we show the difference between both SFR estimates with respect to the stellar mass when using B04 methods to derive SFR. In the upper panel the SFR has been derived using the mass dependent eff ciency value, while in the lower panel we used the mass dependent eff ciency and dust extinction value. It can be seen that, even when using mass-dependent eff ciencies, the disagreement between both SFR indicators at lower masses is still present. When including the extinction values derived from B04, the disagreement at lower masses is slightly reduced, although the SFR(L_{IR}) is generally over-estimated with respect to the SFR(Hα) at higher masses.

7.4.3 Metallicity

It is also interesting to consider the effect of metallicity. Metallicity and mass are correlated by the well known mass-metallicity relation (Tremonti et al., 2004), with more massive galaxies having higher metallicities, at least up to $logM \sim 10$, where the relation f attens. Therefore, the difference between SFR(Hα) and SFR(L_{IR}) could also be due to the different metal content of the galaxies.

To test this effect we made use of the COSMOS metallicity catalog by Nair et al. (in preparation), using the Denicoló et al. (2002) method to estimate metallicity from [NII] and Hα emission lines. In Fig. 7.27 we show the same as in Fig. 7.23, but with respect to metallicity. It can be observed that, for increasing metallicities, the

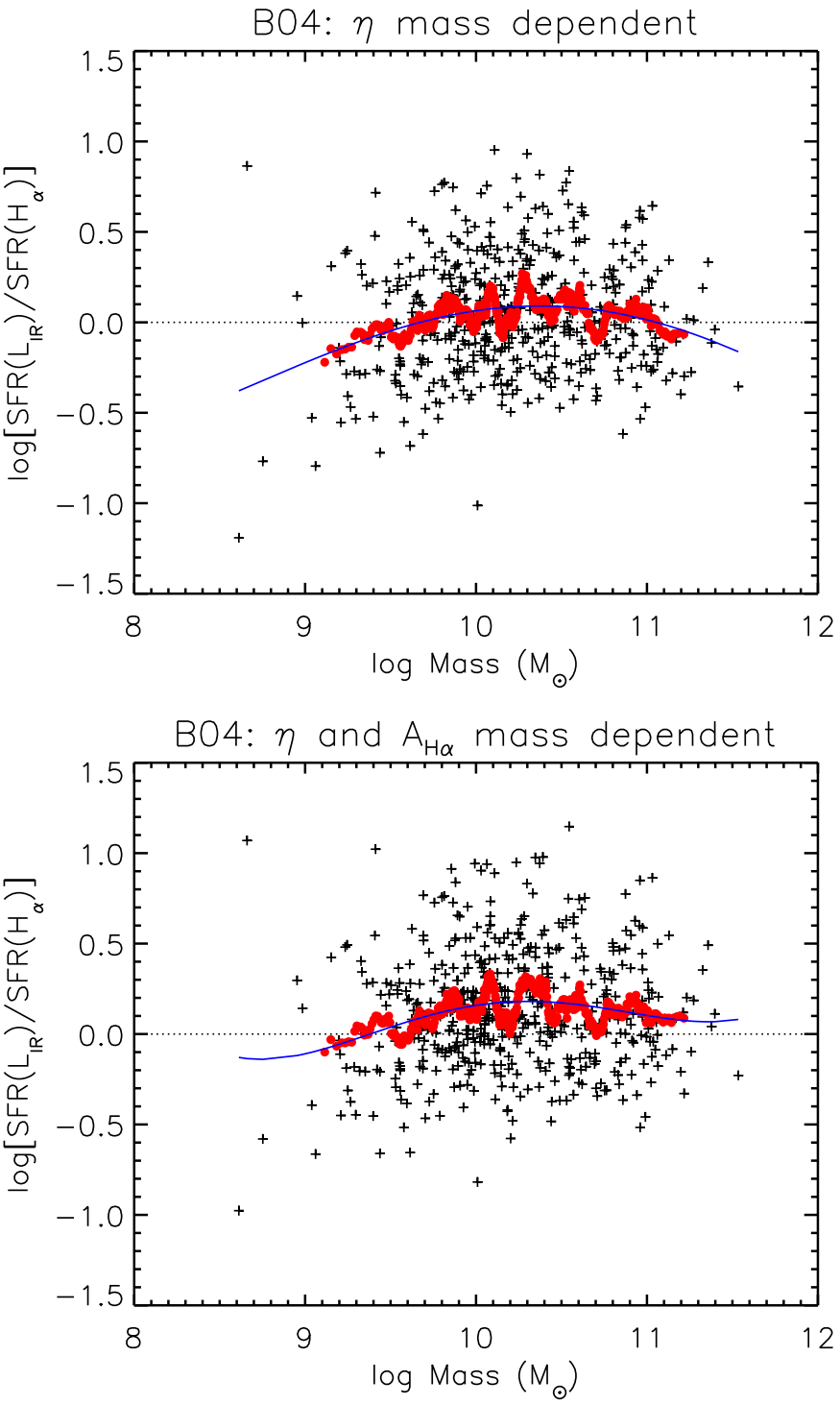

Figure 7.26: Same as in the lower panel of Fig. 7.25 for the SFR(Hα) values derived following B04 recipes (mass dependent $\eta^0_{H\alpha}$ in the upper panel; mass dependent $\eta^0_{H\alpha}$ and $A_{H\alpha}$ in the lower panel).

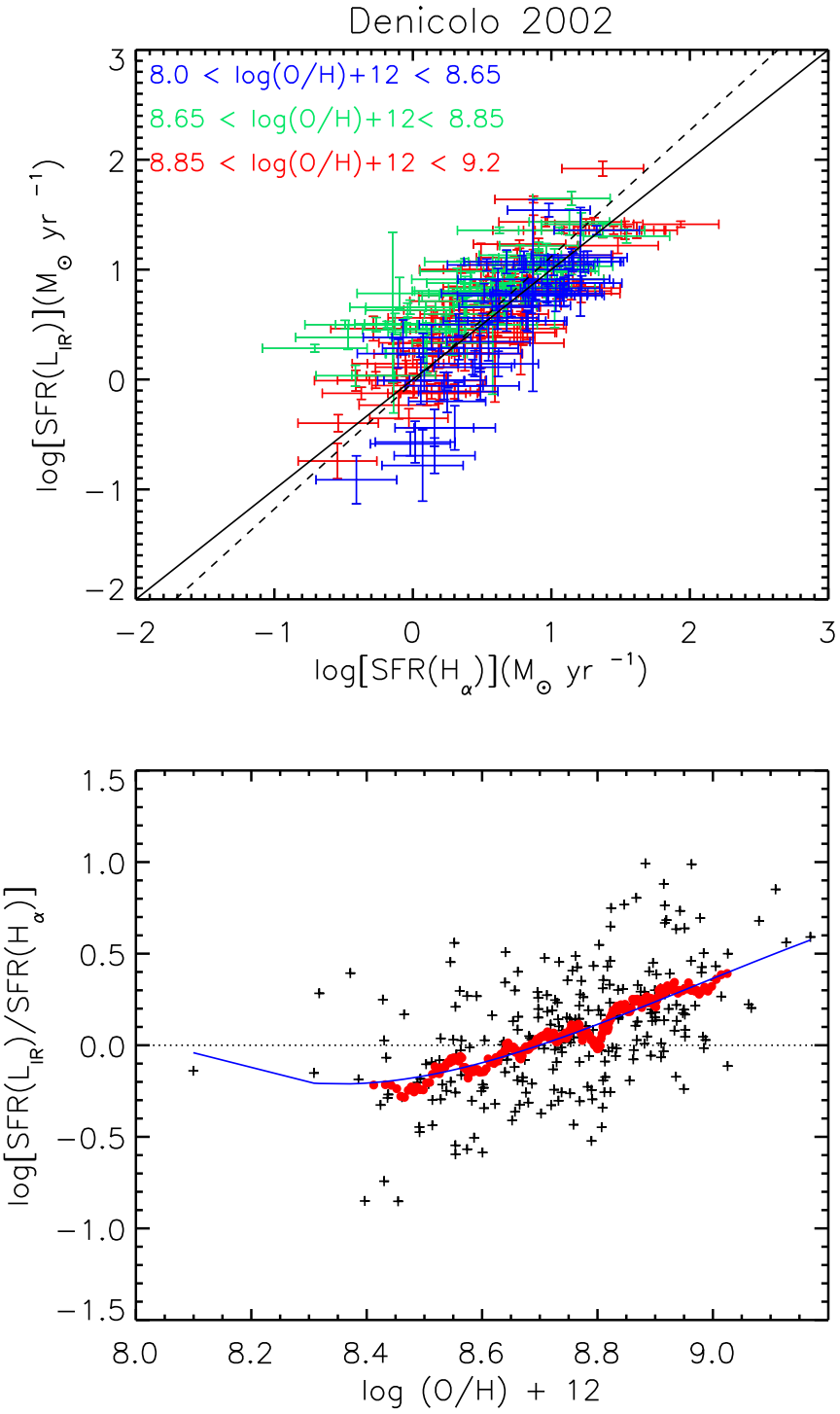

Figure 7.27: Same as in Fig. 7.23 but here colors represent different metallicity bins.

SFR(L_{IR}) is over-estimated with respect to the SFR(Hα). The difference between both SFR indicators varies of $\sim$ 0.6 dex when moving from the lowest to the highest metallicity values. This is consistent with the fact that, in galaxies with higher metallicities, the dust is more eff cient in absorbing and re-emitting the light emitted by young stars at IR wavelengths. Therefore, for the same SFR values, a galaxy with high metallicity emits more in the IR; thus the SFR derived from the L_{IR} is over-estimated with respect to the SFR from the Hα luminosity. We tested this effect making use of the B04 recipes to derive SFR(Hα, B04) and SFR(Hα, B04, ext.) to see if mass dependent eff ciencies or dust attenuations had any inf uence on the SFR estimates comparison, but no improvement was achieved (see Fig. 7.28). We conclude that metallicity is a key parameter when deriving the SFR and suggest to apply the K98 relation carefully when considering very low/ high metallicity galaxies.

7.4.4 Specif c Star Formation Rate

The SSFR is a very interesting parameter as it does not only account for the number of stars being formed, but also takes into account the eff ciency of a galaxy of a given mass to transform a certain amount of gas mass into stars with respect to its total mass context. It gives us information about the star formation activity of a galaxy, allowing us to divide them into star-forming, active or intermediate galaxies. It is reasonable to consider that galaxies with different star-formation modes may show different luminosity-SFR relations. In Fig. 7.29 we show an analog plot to Fig. 7.23 where now the considered parameter is the SSFR ($SSFR = SFR/Mass$). The SFR value that we use in this plot is the median value of SFR(Hα) and SFR(L_{IR}). This value has been chosen to avoid a systematic trend with one of the two SFR indicators, which are present in the *y* axis. As expected, all of our galaxies have high values of SSFR and would be classif ed as star-forming galaxies following the criteria explained in Sect. 5.5.

We observe a slight overestimation of the SFR(L_{IR}) with respect to the SFR(Hα) for galaxies with small values of SSFR of $\sim$ 0.3 dex at SSFR < 10.0(yr^{-1}), while for the systems with higher SSFR the two SFR indicators seem to be in good agreement. One possible explanation for this discrepancy is the fact that the old stellar population may signif cantly contribute to the L_{IR} of a galaxy (see for example da Cunha et al. 2011). For the galaxies with low SSFR, the heating by

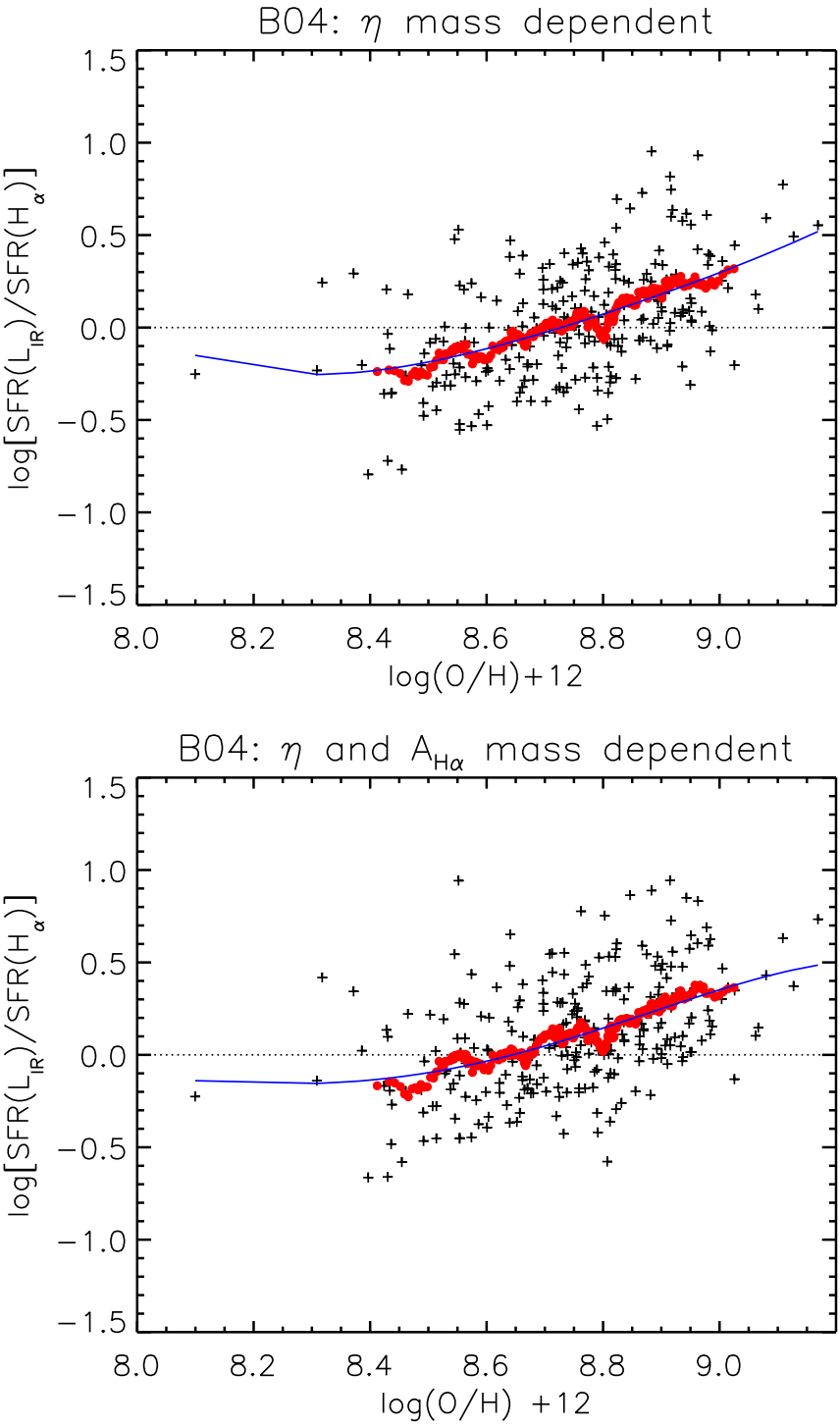

Figure 7.28: Same as in Fig. 7.24 but with respect to the metallicity.

stars older than 10^7 yr in the diffuse inter stellar medium can be comparable to the dust luminosity form the absorption of light from young stars; thus the value of the SFR(L_{IR}) is overestimated as it includes emission form the old stellar population and not only from the recently formed stars.

This effect is also observed even when comparing the SFR(L_{IR}) with the SFR(Hα, B04), as can be seen from the upper panel of Fig. 7.30. For the SFR(Hα, B04, ext.), the effect is slightly reduced but still observed for low SSFR values (lower panel of Fig. 7.30). We conclude that caution must be taken when deriving the SFR from the L_{IR} for galaxies with low values of SSFR, as the emission from the older stellar population may overestimate the derived SFR.

7.4.5 Morphological Type

Another important characteristic that could affect the SFR indicators is the morphological type, as different morphologies imply different star formation histories and geometries and therefore different SEDs and IR emission. To assess the effect of morphology on the SFR derivation we made use of the morphological catalog by Nair et al. (in prep.), who, following a similar scheme as in Nair & Abraham (2010), visually classif ed the galaxies belonging to the COSMOS f eld, dividing them into different types (Ell, S0, Sa-Sd, Irr). In Fig. 7.31 we show the usual SFR(L_{IR}) vs SFR(Hα) plot dividing our sample into different morphological types.

The SFR(L_{IR})-SFR(Hα) seems to be in very good agreement with the bulk of spiral galaxies. For the Sa and Sb samples, the agreement between the two SFR estimates is extremely good ($m = 0.99 \pm 0.08$ and $m = 1.01 \pm 0.06$, respectively) and it is consistent within 3σ also for the Sc sample ($m = 1.16 \pm 0.07$). For the Sd, irregular sample (Sd/Irr), the relation becomes much steeper ($m = 2.45 \pm 0.99$) but is still consistent within 3σ when we take into account that the statistics of this sub-sample are reduced (we have only 17 sources classif ed as Sd or irregular galaxies). The same effect is seen when using the B04 methods to derive the SFR from the Hα luminosity. One possible explanation for the discrepancy of both SFR indicators for the Irr/Sd galaxies is their complex morphology. Irregular galaxies are clumpier and less homogeneous than earlier spiral galaxies, thus making it more diff cult to measure the total Hα f ux of the galaxy by applying aperture corrections. Despite the fact that the number of Sd/Irr objects is quite small, we observe a continuous

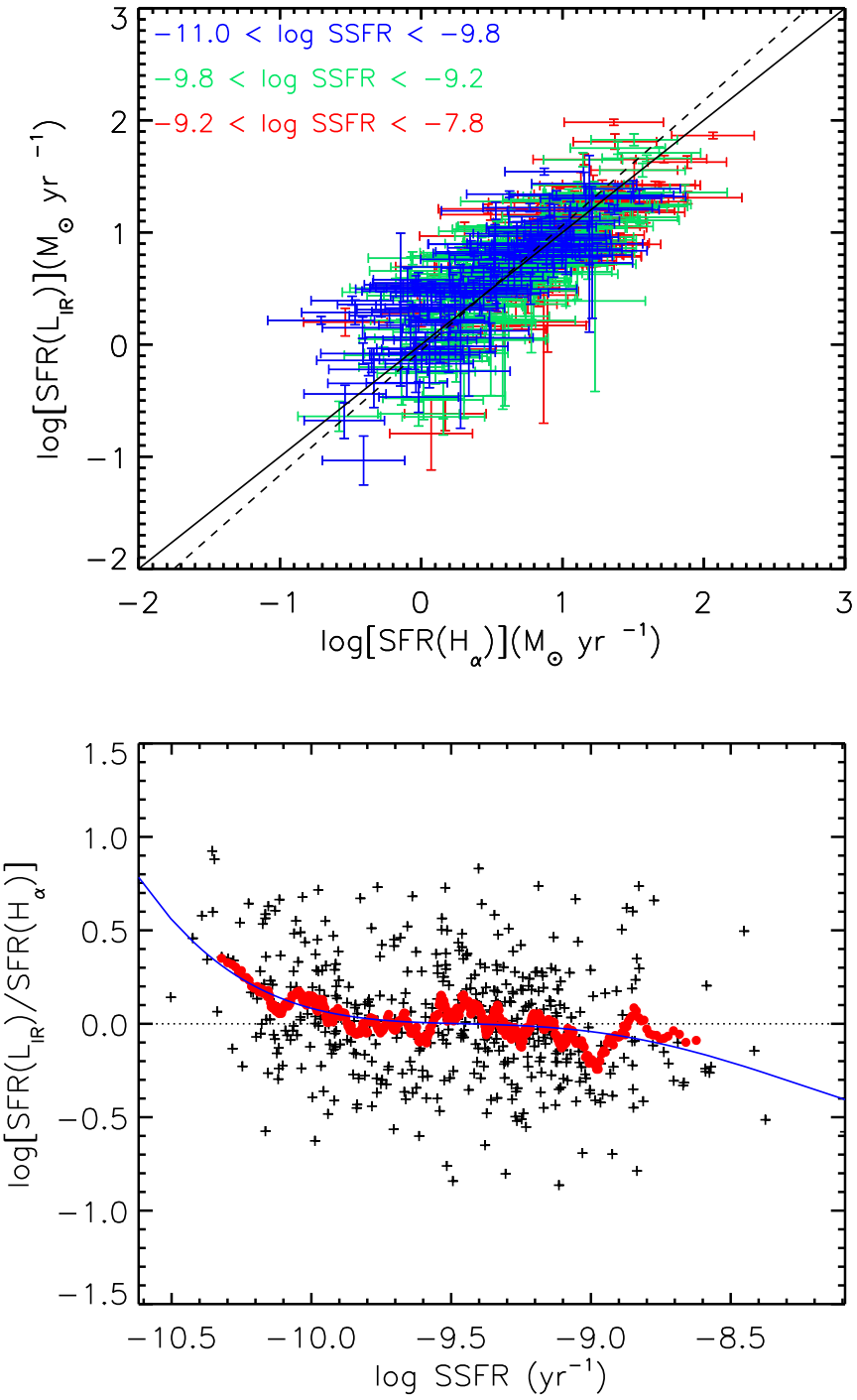

Figure 7.29: Same as in Fig. 7.23 but here colors represent different SSFR bins.

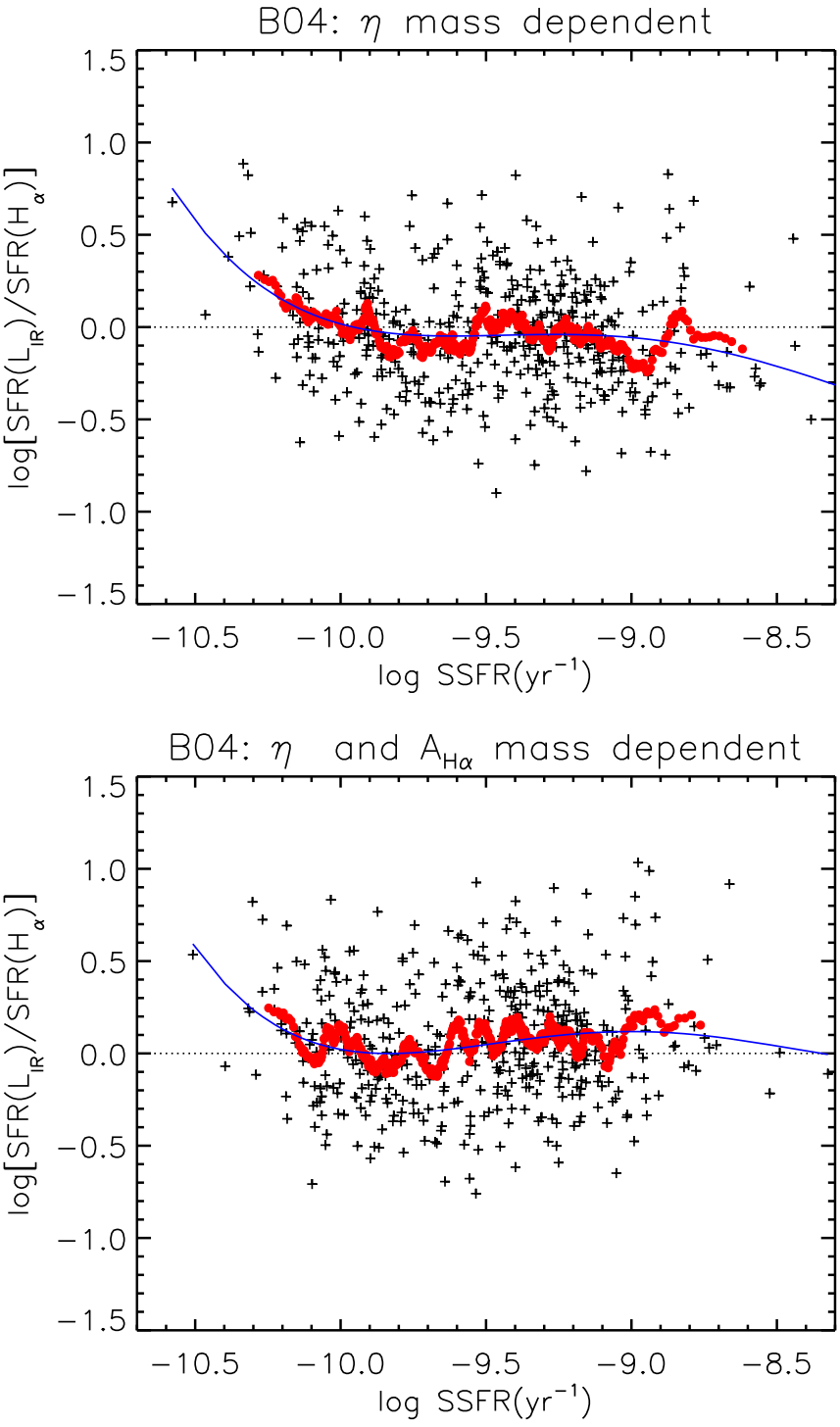

Figure 7.30: Same as in Fig. 7.24 but with respect to SSFR.

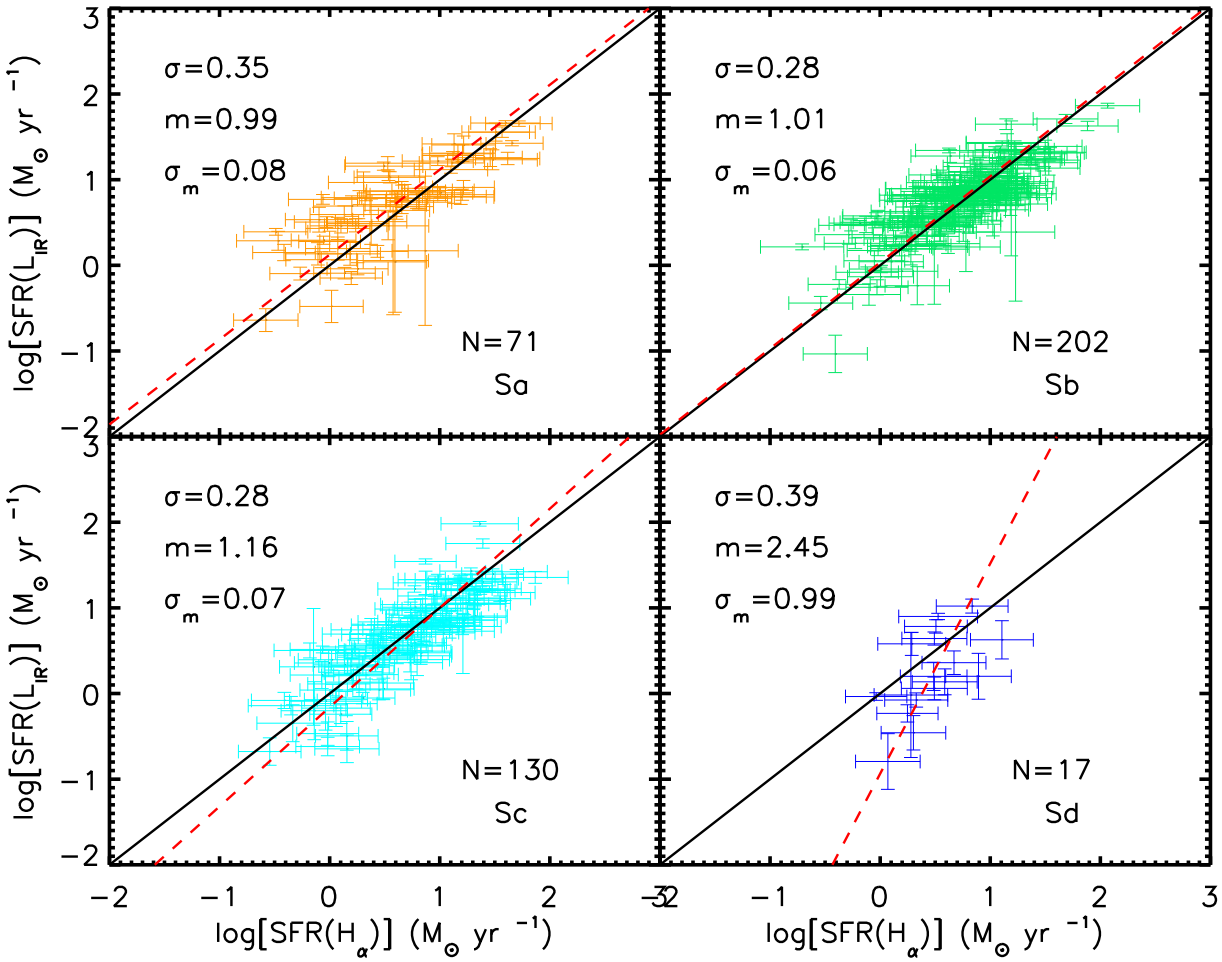

Figure 7.31: SFR(L_{IR}) vs SFR(Hα) for sources classif ed as Sa, Sb, Sc or Sd/Irr. Red dashed and continuous lines are the best f t to our data and the one to one relation, respectively.

trend of a steepening of the slope of the SFR(L_{IR})-SFR(Hα) relation when moving from early to late spiral galaxies. For example, if we consider Sa and Sb galaxies together we obtain a slope of $m = 1.00$, *i.e.* a 3σ difference with respect to the slope for the Sc sample. This difference may be indicative of a weak dependence of the SFR indicators on morphology. However, a more signif cant statistical sample could be extremely useful to asses if the observed steepening of the slope with morphological type is a real effect or if it is just due to the few sources considered for each morphological type, specially for the Sd/Irr sample.

Conclusions

In this thesis we have studied the evolution of the stellar mass function of different galaxy types (classified on the basis of their SSFR) as a function of the redshift (at $1.4 \leq z \leq 3.0$) for an infrared selected sample of galaxies in the COSMOS field. We have also studied the comparison between the SFR values derived from the L_{IR} by means of the Kennicutt (1998b) relation (Eq. 3.4) and the SFR derived from the extinction corrected Hα luminosity for an infrared selected sample of galaxies at $0 < z < 0.46$.

To study the evolution of the stellar mass of different galaxy types, we derived the GSMF and the stellar the mass density in the COSMOS field (~ 1.73 deg^2) from $z = 1.4$ to $z = 3.0$ for the whole sample and for the sample divided into populations according to their SSFR (star-forming, intermediate, quiescent), paying special attention to the quiescent one. The GSMF estimate is based on ~ 18000 galaxies with $mag_{3.6\mu m}$ <22.0 and $z \geq 1.4$. We summarize our results below:

- We found that an IRAC selected sample is fundamental for studying quiescent galaxies at high redshift. Calling 'optical', 'K_s' and 'IRAC' sub-samples to the sources detected in the optical bands, not detected in the optical bands but with detection in the K_s selected catalog or detected only in the IRAC bands, respectively; we found that about 88% and 91% of the 'K_s' and 'IRAC' sub-samples are found at $z \gtrsim 1.4$ respectively, with this fraction dropping to 21% for an i^+-band selected sample. Considering the galaxy classification, 62% of the optically selected sub-sample is fitted by a blue template, while the same fraction is much lower ($\sim 7\%$) for the IRAC sub-sample.

- We studied the main properties of the high redshift quiescent sample ($z \geq 1.4$), finding that they are old and massive galaxies, with $\langle M \rangle \sim 10^{10.65} M_\odot$ and ages ranging from ~ 1 to ~ 4 Gyr. They have small *e-folding* time scales $\tau \sim$

0.1 – 0.3 Gyr and very low dust extinction (E(B-V) $\sim$ 0 – 0.15), meaning passively evolving populations.

- We observed a signif cant evolution of the quiescent galaxy mass function (QSMF) from $2.5 < z < 3.0$ to $1.4 < z < 1.6$, amounting to $\sim$ 1 dex for galaxies with $logM \sim 11.0$. The evolution is $\sim$ 0.3 dex in each redshift bin, meaning that the number of quiescent galaxies continuously increases with cosmic time.

- We found that $z \sim 1.5$ is a clear epoch of transition of the GSMF: while the GSMF at $z \gtrsim 1.5$ is dominated by the star-forming galaxies at all stellar masses, at $z \lesssim 1.5$ the contribution to the total GSMF of the quiescent galaxies is signif cant and the quiescent galaxies become more important than the star-forming population for $M \geqslant 10^{10.75}M_{\odot}$.

- The fraction of star-forming galaxies decreases from 60% to 20% from $2.5 < z < 3.0$ to $1.4 < z < 1.6$ for $M \sim 10^{11.0}M_{\odot}$, while the quiescent population increases from 10% to 50% at the same z and mass intervals.

- We found a signif cant number of quiescent galaxies already in place at $z > 2.5$ ($\rho \sim 6.0$ $M_{\odot}Mpc^{-3}$), meaning that these galaxies assembled most of their stellar mass in previous epochs in an active starburst phase or through important merging processes at higher redshifts.

- All of the theoretical models agree in predicting a gradual increase with cosmic time in the fraction of galaxies with a low SFR. However, only the K07 Millennium-based model is able to properly reproduce the shape of the data. The inclusion of radio mode feedback from the central galaxies of groups and clusters in theoretical models seems to be fundamental to recover the observed properties of the high redshift quiescent population.

In this thesis we also compare the SFR values derived from two indicators: the L_{IR} and the Hα emission line luminosity. We studied a sample of 474 galaxies at z=0.06-0.46 with both spectroscopic and IR data from the 20k zCOSMOS survey and the PEP Herschel survey at 100 and 160 μm. The L_{IR} was derived by integrating from 8 up to 1000 μm the best-f tting SED to the data. We calculated the SFR from the Hα luminosity by taking into account the dust extinction. We divided our sources in three L_{IR} bins and constructed median spectra to derive the

extinction corrections from the Hα/Hβ observed ratio of the three median spectra. We conclude that:

- Comparing the two SFRs estimates, we found a very good agreement between them for the bulk of the studied galaxies, meaning that the simple recipes used to convert luminosity into SFR are consistent with each other.

- We do not observe any signif cant dependence of the calibration as a function of the redshift, at least up to $z \sim 0.46$, which is the limit of our sample.

- The stellar mass seems to partially inf uence the SFR(L_{IR})-SFR(Hα) relation, in the sense that for low mass galaxies ($logM < 9.3 M_{\odot}$) the SFR(L_{IR}) seems to be under-estimated with respect to SFR(Hα). This could be due to the fact that high mass galaxies usually undergo constant SFHs, which is one of the assumptions taken in the K98 relation, while for low mass systems the SFHs seem to be more complicated.

- We found that the metallicity has a signif cant effect in the SFR calibration, with values of log [SFR(L_{IR})/SFR(Hα)] $\sim$ 0.6 dex different from low to high metallicity galaxies. The metallicity effect cannot be avoided even when using B04 recipes. This effect can be explained by the fact that more metallic galaxies more effectively re-emitt the light from the young stars at IR wavelenghts; thus, for the same SFR values a more metallic galaxy has a higher L_{IR} than a less metallic galaxy.

- The SFR(L_{IR}) seems to be overestimated with respect to the SFR(Hα) for galaxies with low SSFR values (< 10 [yr^{-1}]) due to the IR emission from the old stellar population. Stars older than 10^7 yr may signif cantly contribute to the L_{IR} in systems with little star formation activity; therefore, the SFR derived from the L_{IR} is overestimated as it does not only account for the recently formed stellar population.

- When separately studying the SFRs indicators as a function of morphological types, we f nd that they are in excellent agreement for the Sa and Sb galaxies, while the relation is steeper for later types ($m = 1.16 \pm 0.07$ and $m = 2.45 \pm 0.99$ for the Sc and Sd/Irr samples, respectively). Although the values of the slope are consistent with the one to one relation at the 3σ level, we detect a continuous trend of steepening of the slope of the relation when moving

from early to late spiral galaxies. A more statistical signif cant sample may be useful to elucidate if this trend is actually observed or if it is due to the small number of sources considered in the Sd/Irr sample.

Publications

1. **The evolution of quiescent galaxies at high redshifts (z ≥ 1.4)**

H. Domínguez Sánchez, F. Pozzi, C. Gruppioni, A. Cimatti, O. Ilbert, L. Pozzetti, H. McCracken, P. Capak, E. Le Floch, M. Salvato, G. Zamorani, C. M. Carollo, T. Contini, J.-P. Kneib, O. Le Fèvre, S. J. Lilly, V. Mainieri, A. Renzini, M. Scodeggio, S. Bardelli, M. Bolzonella, A. Bongiorno, K. Caputi, G. Coppa, O. Cucciati, S. de la Torre, L. de Ravel, P. Franzetti, B. Garilli, A. Iovino, P. Kampczyk, C. Knobel, K. Kovač, F. Lamareille, J.-F. Le Borgne, V. Le Brun, C. Maier, M. Mignoli, R. Pelló, Y. Peng, E. Perez-Montero, E. Ricciardelli, J. D. Silverman, M. Tanaka, L. A. M. Tasca, L. Tresse, D. Vergani, E. Zucca

2011, Monthly Notices of the Royal Astronomical Society, 417, 900-915

Abstract

The goal of this work is to study the evolution of high redshift ($z \geq 1.4$) quiescent galaxies over an effective area of ~ 1.7 deg^2 in the COSMOS f eld. Galaxies have been divided according to their star-formation activity and the evolution of the different populations, in particular of the quiescent galaxies, has been investigated in detail. We have studied an IRAC ($mag_{3.6\mu m}$ <22.0) selected sample of ∼ 18000 galaxies at z ≥ 1.4 in the COSMOS f eld with multi-wavelength coverage extending from the *U* band to the *Spitzer* 24 μm one. We have derived accurate photometric redshifts ($\sigma_{\Delta z/(1+z_s)}$ = 0.06) through a SED-f tting procedure. Other important physical parameters (masses, ages and star formation rates) of the galaxies have been obtained using Maraston (2005) models. We have divided our sample into actively

star-forming, intermediate and quiescent galaxies depending on their specif c star formation rate. We have computed the galaxy stellar mass function of the total sample and the different populations at $z = 1.4 - 3.0$. We have studied the properties of high redshift quiescent galaxies f nding that they are old (1 – 4 Gyr), massive ($\langle M \rangle \sim 10^{10.65} M_{\odot}$), weakly star forming stellar populations with low dust extinction (E(B-V) ≤ 0.15) and small e-folding time scales ($\tau \sim 0.1 - 0.3$ Gyr). We observe a signif cant evolution of the quiescent stellar mass function from $2.5 < z < 3.0$ to $1.4 < z < 1.6$, increasing by $\sim$ 1 dex in this redshift interval. We f nd that $z \sim 1.5$ is an epoch of transition of the GSMF: while the GSMF at $z \gtrsim 1.5$ is dominated by the star-forming galaxies at all stellar masses, at $z \lesssim 1.5$ the contribution to the total GSMF of the quiescent galaxies is signif cant and becomes higher than that of the star-forming population for $M \geqslant 10^{10.75} M_{\odot}$. The fraction of star-forming galaxies decreases from 60% to 20% from $z \sim 2.5 - 3.0$ to $z \sim 1.4 - 1.6$ for $M \sim 10^{11.0} M_{\odot}$, while the quiescent population increases from 10% to 50% at the same redshift and mass intervals. We compare the fraction of quiescent galaxies derived with that predicted by theoretical models and f nd that the Kitzbichler & White (2007) model, implemented on the Millennium Simulation, is the one that better reproduces the shape of the data. Finally, we calculate the stellar mass density of the star-forming and quiescent populations as a function of redshift and f nd that there is already a signif cant number of quiescent galaxies at $z > 2.5$ ($\rho \sim 6.0$ $M_{\odot} Mpc^{-3}$), meaning that eff cient star formation had to take place before that time.

2. **Comparison of the SFR estimates from Hα luminosity and L_{IR} with new Herschel data**

H. Domínguez Sánchez, M. Mignoli, F. Pozzi, C. Gruppioni, A. Cimatti, J. Cepa, M. Sánchez Portal, G. Zamorani, PEP and zCOSMOS teams

In preparation.

Abstract

We empirically test the relation between the SFR derived from the L_{IR} and SFR derived from the Hα emission line luminosity using simple conversion relations. We use a sample of 474 galaxies at $z = 0.06 - 0.46$ with both spectroscopic information (20k zCOSMOS) and new far-IR Herschel data (100 and 160 μm). We derive SFR from the Hα extinction corrected emission line luminosity, SFR(Hα). The extinction values are calculated in L_{IR} bins from median spectrum. We calculate the L_{IR} by integrating from 8 up to 1000 μm the best-f tting SED to our IR data. We compare the SFR(Hα) with the SFR derived from the L_{IR}, SFR(L_{IR}). We f nd a very good agreement between the two SFRs estimates, with a slope of $m = 1.11 \pm 0.04$ in the SFR(L_{IR}) vs SFR(Hα) diagram and a dispersion of $\sigma = 0.31$. We study the effect of some intrinsic properties of the galaxies in the SFR(L_{IR})-SFR(Hα) relation. We f nd almost no dependence with redshift (up to 0.46) and little inf uence with stellar mass, in the sense that for low mass galaxies ($logM < 9.3M_{\odot}$) the SFR(L_{IR}) seems to be under-estimated with respect to SFR(Hα). The metallicity seems to have a more important effect in the SFR comparison, with values of log[SFR(L_{IR})/SFR(Hα)] $\sim$ 0.6 dex different from low to high metallicity galaxies. The SFR(L_{IR}) seems to be overestimated with respect to the SFR(Hα) for low SSFR systems, probably due to the IR emission from the older stellar population. We also study the SFR(L_{IR})-SFR(Hα) relation by dividing our sample in morphological types. Both SFRs estimates are in very good agreement for the Sa, Sb and Sc morphologically classif ed galaxies, with a slight increase on the slope of the SFR(L_{IR}) vs SFR(Hα) diagram (from $m = 0.99 \pm 0.08$ to $m = 2.45 \pm 0.99$ from the Sa to the Sd/Irr types). Although still consistent at 3σ for all the morphological types, there is a continuous trend of steepening of the SFR(L_{IR})-SFR(Hα) relation when moving from

early to late galaxy types.

Bibliography

Abraham, R. G. et al. 2007, AJ, 669, 184, arXiv:astro-ph/0701779

Allen, C. W. 1976, Astrophysical Quantities, ed. Allen, C. W.

Arnouts, S. et al. 2001, A&A, 379, 740, arXiv:astro-ph/0103071

Arnouts, S., Walcher, C. J., Le Fèvre, O., Zamorani, G., & Ilbert, O. e. a. 2007, A&A, 476, 137, 0705.2438

Baldry, I. K., Balogh, M. L., Bower, R., Glazebrook, K., & Nichol, R. C. 2004, in American Institute of Physics Conference Series, Vol. 743, The New Cosmology: Conference on Strings and Cosmology, ed. R. E. Allen, D. V. Nanopoulos, & C. N. Pope, 106–119, arXiv:astro-ph/0410603

Baldwin, J. A., Phillips, M. M., & Terlevich, R. 1981, PASP, 93, 5

Barbaro, G., & Poggianti, B. M. 1997, A&A, 324, 490, arXiv:astro-ph/9702129

Bell, E. F., McIntosh, D. H., Katz, N., & Weinberg, M. D. 2003, ApJS, 149, 289, arXiv:astro-ph/0302543

Bell, E. F. et al. 2004, ApJ, 608, 752, arXiv:astro-ph/0303394

Bertelli, G., Nasi, E., Girardi, L., & Marigo, P. 2009, A&A, 508, 355, 0911.2419

Bertoldi, F. et al. 2007, ApJS, 172, 132

Bolzonella, M., Miralles, J.-M., & Pelló, R. 2000, A&A, 363, 476, arXiv:astro-ph/0003380

Bolzonella, M., nekKovac, K., Pozzetti, L., Zucca, E., Cucciati, O., & Lilly, e. a. 2009, ArXiv e-prints, 0907.0013

Bongiorno, A., Mignoli, M., Zamorani, G., Lamareille, F., & Lanzuisi, e. a. 2010, Aap, 510, A56+, 0911.3914

Bonnor, W. B. 1956, MNRAS, 116, 351

Borch, A. et al. 2006, AAP, 453, 869, arXiv:astro-ph/0604405

Bower, R. G., Terlevich, A., Kodama, T., & Caldwell, N. 1999, in Astronomical Society of the Pacif c Conference Series, Vol. 163, Star Formation in Early Type Galaxies, ed. P. Carral & J. Cepa, 211, arXiv:astro-ph/9808325

Brinchmann, J., Charlot, S., White, S. D. M., Tremonti, C., Kauffmann, G., Heckman, T., & Brinkmann, J. 2004, MNRAS, 351, 1151, arXiv:astro-ph/0311060

Bruzual, G., & Charlot, S. 2003, MNRAS, 344, 1000, arXiv:astro-ph/0309134

Bruzual A., G., & Charlot, S. 1993, ApJ, 405, 538

Bundy, K., Ellis, R. S., Conselice, C. J., Cooper, M., Weiner, B., Taylor, J., Willmer, C., & DEEP2 Team. 2005, in Bulletin of the American Astronomical Society, Vol. 37, Bulletin of the American Astronomical Society, 1235–+

Buzzoni, A. 1989, ApJS, 71, 817

Calzetti, D., Armus, L., Bohlin, R. C., Kinney, A. L., & Koornneef, e. a. 2000, ApJ, 533, 682, arXiv:astro-ph/9911459

Capak, P., Aussel, H., Ajiki, M., McCracken, H. J., Mobasher, B., & Scoville, e. a. 2007, ApJS, 172, 99, 0704.2430

Cappelluti, N. et al. 2009, A&A, 497, 635, 0901.2347

Cassata, P. et al. 2008, A&A, 483, L39, 0804.1064

——. 2007, ApJS, 172, 270, arXiv:astro-ph/0701483

Chabrier, G. 2003, PASP, 115, 763, arXiv:astro-ph/0304382

Charlot, S., & Bruzual, A. G. 1991, ApJ, 367, 126

Chary, R., & Elbaz, D. 2001, ApJ, 556, 562, arXiv:astro-ph/0103067

Chiosi, C., Bertelli, G., & Bressan, A. 1988, A&A, 196, 84

Cimatti, A. 2006, Nuovo Cimento B Serie, 121, 1383

Cimatti, A. 2009, in American Institute of Physics Conference Series, Vol. 1111, American Institute of Physics Conference Series, ed. G. Giobbi, A. Tornambe, G. Raimondo, M. Limongi, L. A. Antonelli, N. Menci, & E. Brocato, 191–198, 0901.1457

Cimatti, A. et al. 2008, A&A, 482, 21, 0801.1184

——. 2004, Nat, 430, 184, arXiv:astro-ph/0407131

——. 2002, VizieR Online Data Catalog, 339, 20395

Cirasuolo, M., McLure, R. J., & Dunlop, J. S. 2007, Nuovo Cimento B Serie, 122, 1133

Cole, S., Norberg, P., Baugh, C. M., Frenk, C. S., & Bland-Hawthorn, e. 2001, MNRAS, 326, 255, arXiv:astro-ph/0012429

Coleman, G. D., Wu, C.-C., & Weedman, D. W. 1980, ApJS, 43, 393

Cowie, L. L., Songaila, A., Hu, E. M., & Cohen, J. G. 1996, AJ, 112, 839, arXiv:astro-ph/9606079

da Cunha, E., Charlot, S., Dunne, L., Smith, D., & Rowlands, K. 2011, ArXiv e-prints, 1111.3961

Daddi, E., Cimatti, A., Renzini, A., Fontana, A., Mignoli, M., Pozzetti, L., Tozzi, P., & Zamorani, G. 2004, ApJ, 617, 746, arXiv:astro-ph/0409041

Daddi, E. et al. 2007, ApJ, 670, 156, 0705.2831

——. 2005, ApJ, 626, 680, arXiv:astro-ph/0503102

Dale, D. A., Helou, G., Contursi, A., Silbermann, N. A., & Kolhatkar, S. 2001, ApJ, 549, 215

Damen, M. et al. 2010, ArXiv e-prints, 1011.2764

De Lucia, G. et al. 2007, MNRAS, 374, 809, arXiv:astro-ph/0610373

Denicoló, G., Terlevich, R., & Terlevich, E. 2002, MNRAS, 330, 69, arXiv:astro-ph/0110356

Driver, S. P. et al. 2006, MNRAS, 368, 414, arXiv:astro-ph/0602240

Ebert, R. 1957, Z. Astrophys., 42, 263

Elbaz, D. et al. 2007, A&A, 468, 33, arXiv:astro-ph/0703653

Elbaz, D., Hwang, H. S., Magnelli, B., Daddi, E., & Aussel, H. e. a. 2010, AAP, 518, L29, 1005.2859

Ellis, R. S., Colless, M., Broadhurst, T., Heyl, J., & Glazebrook, K. 1996, MNRAS, 280, 235, arXiv:astro-ph/9512057

Elvis, M. et al. 2009, ApJS, 184, 158, 0903.2062

Faber, S. M., & Jackson, R. E. 1976, ApJ, 204, 668

Faber, S. M. et al. 2007, ApJ, 665, 265, arXiv:astro-ph/0506044

Fitzpatrick, E. L. 1985, ApJ, 299, 219

Fontana, A. et al. 2006, A&A, 459, 745, arXiv:astro-ph/0609068

——. 2009, A&A, 501, 15, 0901.2898

Fontanot, F., Monaco, P., Silva, L., & Grazian, A. 2007, MNRAS, 382, 903, 0709.1804

Franceschini, A., Rodighiero, G., Cassata, P., Berta, S., & Vaccari, e. a. 2006, A&A, 453, 397, arXiv:astro-ph/0601003

Franx, M. et al. 2003, ApJL, 587, L79, arXiv:astro-ph/0303163

Franx, M., van Dokkum, P. G., Schreiber, N. M. F., Wuyts, S., Labbé, I., & Toft, S. 2008, ApJ, 688, 770, 0808.2642

Gallazzi, A., Charlot, S., Brinchmann, J., & White, S. D. M. 2006, MNRAS, 370, 1106, arXiv:astro-ph/0605300

Giallongo, E., Salimbeni, S., Menci, N., Zamorani, G., Fontana, A., Dickinson, M., Cristiani, S., & Pozzetti, L. 2005, ApJ, 622, 116, arXiv:astro-ph/0412044

Graves, G. J., Faber, S. M., & Schiavon, R. P. 2009, ApJ, 698, 1590, 0903.3603

Gruppioni, C. et al. 2010, AAP, 518, L27, 1005.1473

——. 2008, ApJ, 684, 136, 0805.0705

Hasinger, G. et al. 2007, ApJS, 172, 29, arXiv:astro-ph/0612311

Heckman, T. M. 1980, A&A, 87, 142

Hogg, D. W. 1999, ArXiv Astrophysics e-prints, arXiv:astro-ph/9905116

Hubble, E. 1929, Proceedings of the National Academy of Science, 15, 168

Hubble, E. P. 1926, ApJ, 64, 321

Ilbert, O., Arnouts, S., McCracken, H. J., Bolzonella, M., & Bertin, e. a. 2006, A&A, 457, 841, arXiv:astro-ph/0603217

Ilbert, O., Capak, P., Salvato, M., Aussel, H., & McCracken, e. a. 2009, ApJ, 690, 1236, 0809.2101

Ilbert, O., Salvato, M., Le Floc'h, E., Aussel, H., Capak, P., & McCracken, e. a. 2010, ApJ, 709, 644, 0903.0102

Jarosik, N. et al. 2011, ApJS, 192, 14, 1001.4744

Kauffmann, G. et al. 2003, MNRAS, 346, 1055, arXiv:astro-ph/0304239

Kennicutt, Jr., R. C. 1998a, ARA&A, 36, 189, arXiv:astro-ph/9807187

——. 1998b, ApJ, 498, 541, arXiv:astro-ph/9712213

Kennicutt, Jr., R. C., Tamblyn, P., & Congdon, C. E. 1994, ApJ, 435, 22

Kitzbichler, M. G., & White, S. D. M. 2007, MNRAS, 376, 2, arXiv:astro-ph/0609636

Klypin, A., Kravtsov, A. V., Bullock, J. S., & Primack, J. R. 2001, ApJ, 554, 903, arXiv:astro-ph/0006343

Kneiske, T. M., Mannheim, K., & Hartmann, D. H. 2002, A&A, 386, 1, arXiv:astro-ph/0202104

Kochanek, C. S. et al. 2001, ApJ, 560, 566, arXiv:astro-ph/0011456

Kodama, T., & Arimoto, N. 1997, A&A, 320, 41, arXiv:astro-ph/9609160

Komatsu, E. et al. 2011, ApJS, 192, 18, 1001.4538

Kormendy, J. 1977, ApJ, 218, 333

Kriek, M. et al. 2010, ApJL, 722, L64, 1008.4357

——. 2008, ApJ, 677, 219, 0801.1110

Kroupa, P. 2002, Science, 295, 82, arXiv:astro-ph/0201098

Kroupa, P., Tout, C. A., & Gilmore, G. 1993, MNRAS, 262, 545

Lagache, G. et al. 2004, ApJS, 154, 112, arXiv:astro-ph/0406016

Lamareille, F., Brinchmann, J., Contini, T., Walcher, C. J., & Charlot, S. e. a. 2009, AAP, 495, 53, 0811.2053

Le Fèvre, O. et al. 2003, ArXiv Astrophysics e-prints, arXiv:astro-ph/0311475

Le Floc'h, E., Aussel, H., Ilbert, O., Riguccini, L., Frayer, D. T., & Salvato, e. a. 2009, ApJ, 703, 222, 0909.4303

Leitherer, C., & Heckman, T. M. 1995a, ApJS, 96, 9

——. 1995b, ApJS, 96, 9

Lilly, S. J., Le Brun, V., Maier, C., Mainieri, V., Mignoli, M., Scodeggio, M., & Zamorani, e. 2009, ApJS, 184, 218

Lilly, S. J., Le Fèvre, O., Renzini, A., Zamorani, G., & Scodeggio, e. 2007, ApJS, 172, 70, arXiv:astro-ph/0612291

Lilly, S. J., Tresse, L., Hammer, F., Crampton, D., & Le Fevre, O. 1995, ApJ, 455, 108, arXiv:astro-ph/9507079

Lutz, D., Poglitsch, A., Altieri, B., Andreani, P., & Aussel, H. e. a. 2011, AAP, 532, A90+, 1106.3285

Madau, P., Pozzetti, L., & Dickinson, M. 1998, ApJ, 498, 106, arXiv:astro-ph/9708220

Maraston, C. 1998, MNRAS, 300, 872, arXiv:astro-ph/9807338

——. 2005, MNRAS, 362, 799, arXiv:astro-ph/0410207

Marchesini, D., van Dokkum, P. G., Förster Schreiber, N. M., Franx, M., Labbé, I., & Wuyts, S. 2009, ApJ, 701, 1765, 0811.1773

Mather, J. C. et al. 1994, ApJ, 420, 439

McCarthy, P. J. et al. 2004, ApJ, 614, L9, arXiv:astro-ph/0408367

McCracken, H. J., Capak, P., Salvato, M., Aussel, H., Thompson, D., & Daddi, e. 2010, ApJ, 708, 202, 0910.2705

Menci, N., Fontana, A., Giallongo, E., Grazian, A., & Salimbeni, S. 2006, ApJ, 647, 753, arXiv:astro-ph/0605123

Menci, N., Fontana, A., Giallongo, E., & Salimbeni, S. 2005, ApJ, 632, 49, arXiv:astro-ph/0506387

Mo, H., van den Bosch, F. C., & White, S. 2010, Galaxy Formation and Evolution, ed. Mo, H., van den Bosch, F. C., & White, S.

Nagamine, K., Ostriker, J. P., Fukugita, M., & Cen, R. 2006, ApJ, 653, 881, arXiv:astro-ph/0603257

Nair, P. B., & Abraham, R. G. 2010, ApJs, 186, 427, 1001.2401

Nicol, M.-H., Meisenheimer, K., Wolf, C., & Tapken, C. 2011, ApJ, 727, 51, 1011.4067

Noeske, K. G. et al. 2007, ApJ, 660, L43, arXiv:astro-ph/0701924

Nordon, R., Lutz, D., Berta, S., Wuyts, S., & Magnelli, B. e. a. 2011, ArXiv e-prints, 1106.1186

Pannella, M., Hopp, U., Saglia, R. P., Bender, R., Drory, N., Salvato, M., Gabasch, A., & Feulner, G. 2006, ApJL, 639, L1, arXiv:astro-ph/0601338

Pérez-González, P. G. et al. 2008, ApJ, 675, 234, 0709.1354

Planck Collaboration et al. 2011, A&A, 536, A1, 1101.2022

Polletta, M., Tajer, M., Maraschi, L., Trinchieri, G., & Lonsdale, e. a. 2007, ApJ, 663, 81

Pozzetti, L., Bolzonella, M., Zucca, E., Zamorani, G., & Lilly, e. a. 2010, A&A, 523, A13+, 0907.5416

Prada, F., Klypin, A. A., Cuesta, A. J., Betancort-Rijo, J. E., & Primack, J. 2011, ArXiv e-prints, 1104.5130

Prevot, M. L., Lequeux, J., Prevot, L., Maurice, E., & Rocca-Volmerange, B. 1984, A&A, 132, 389

Renzini, A. 2006, ARA&A, 44, 141, arXiv:astro-ph/0603479

Renzini, A., & Fusi Pecci, F. 1988, ARA&A, 26, 199

Renzini, A., & Voli, M. 1981, A&A, 94, 175

Rodighiero, G., Cimatti, A., Franceschini, A., Brusa, M., Fritz, J., & Bolzonella, M. 2007, A&A, 470, 21, arXiv:astro-ph/0703276

Rodighiero, G. et al. 2010, A&A, 518, L25, 1005.1089

Romano, D., Chiappini, C., Matteucci, F., & Tosi, M. 2004, ArXiv Astrophysics e-prints, arXiv:astro-ph/0409473

Salpeter, E. E. 1955, ApJ, 121, 161

Sanders, D. B., Salvato, M., Aussel, H., Ilbert, O., & Scoville, e. a. 2007, ApJS, 172, 86, arXiv:astro-ph/0701318

Sargent, M. T., Carollo, C. M., Lilly, S. J., Scarlata, C., & Feldmann, R. e. a. 2007, ApJS, 172, 434, arXiv:astro-ph/0609042

Scalo, J. 1998, in Astronomical Society of the Pacif c Conference Series, Vol. 142, The Stellar Initial Mass Function (38th Herstmonceux Conference), ed. G. Gilmore & D. Howell, 201, arXiv:astro-ph/9712317

Scalo, J. M. 1986, in IAU Symposium, Vol. 116, Luminous Stars and Associations in Galaxies, ed. C. W. H. De Loore, A. J. Willis, & P. Laskarides, 451–466

Schechter, P. 1976, ApJ, 203, 297

Schinnerer, E. et al. 2007, ApJS, 172, 46, arXiv:astro-ph/0612314

Schmidt, M. 1959, ApJ, 129, 243

——. 1968, ApJ, 151, 393

Scoville, N. 2007, in Astronomical Society of the Pacif c Conference Series, Vol. 375, From Z-Machines to ALMA: (Sub)Millimeter Spectroscopy of Galaxies, ed. A. J. Baker, J. Glenn, A. I. Harris, J. G. Mangum, & M. S. Yun , 166

Somerville, R. S., Lee, K., Ferguson, H. C., Gardner, J. P., Moustakas, L. A., & Giavalisco, M. 2004, ApJ, 600, L171, arXiv:astro-ph/0309071

Sutherland, W., & Saunders, W. 1992, MNRAS, 259, 413

Taniguchi, Y. et al. 2007, ApJS, 172, 9, arXiv:astro-ph/0612295

Thomas, D., Maraston, C., Bender, R., & Mendes de Oliveira, C. 2005, ApJ, 621, 673, arXiv:astro-ph/0410209

Tinsley, B. M. 1972, A&A, 20, 383

——. 1980, FCP, 5, 287

Toomre, A. 1977, in Evolution of Galaxies and Stellar Populations, ed. B. M. Tinsley & R. B. G. Larson D. Campbell, 401

Tremonti, C. A. et al. 2004, Apj, 613, 898, arXiv:astro-ph/0405537

van Dokkum, P. G. et al. 2008, ApJ, 677, L5, 0802.4094

Veilleux, S., & Osterbrock, D. E. 1987, ApJS, 63, 295

Weiner, B. J. et al. 2005, ApJ, 620, 595, arXiv:astro-ph/0411128

Weisz, D. R. et al. 2011, ArXiv e-prints, 1109.2905

Yan, L., McCarthy, P. J., Weymann, R. J., Malkan, M. A., Teplitz, H. I., Storrie-Lombardi, L. J., Smith, M., & Dressler, A. 2000, AJ, 120, 575

Zamojski, M. A. et al. 2007, ApJS, 172, 468, arXiv:astro-ph/0701478

Zucca, E., Zamorani, G., Vettolani, G., Cappi, A., Merighi, R., & Mignoli, e. a. 1997, A&A, 326, 477, arXiv:astro-ph/9705096